James Weir
Fluids Laboratory

Investigation of smooth contact angle treatment in porous media

Thesis by

Thomas BUREL

University of Strathclyde,

Mechanical and Aerospace Engineering

James Weir Building, 75 Montrose Street

GLASGOW, Lanarkshire G1 1XJ

United Kingdom

A thesis presented in fulfilment of the requirements

for the degree of Doctor of Philosophy

2018

Declaration of author's rights

This thesis is the result of the author's original research. It has been composed by the author and has not been previously submitted for examination which has led to the award of a degree.

Signed: Thomas Burel

Date: 14 September 2018

Abstract

Some of the key challenges faced in the oil/gas extraction and carbon dioxide injection/storage processes are the presence of complex geometries and the significant effect of the capillary forces which arise at low capillary numbers. Therefore, the contact angle needs to be carefully treated. Mesoscopic techniques such as lattice Boltzmann methods are capable of dealing with lower capillary numbers as compared to the Navier-Stokes solvers, which can also implicitly capture the interface between two fluids.

To investigate immiscible two-phase flows at low Reynolds and capillary numbers (Re<1 and Ca<1), the colour-fluid model is used i.e. the Rothman-Keller model [1]. This model includes two steps: a perturbation operator from Lishchuk *et al* [2] (the continuum surface force [3]) or Gunstensen *et al* [4] approaches and a recolouring operator [5]. However, the lattice Boltzmann implementation employs a Cartesian grid for domain discretisation that is unable to conform with curved surfaces. It misinterprets those curved surfaces as a series of stair-like patterns. On those surfaces, a non-physical contact angle could be defined which may lead to a numerically flooding of the wetting fluid inside the droplet for a non-spreading drop or outside for a spreading droplet. To remove this unphysical behaviour and take into account the flow field effect on the contact angle, interpolation techniques are employed to estimate the real contact angle on the "stairs" boundaries. We also employ extrapolations to obtain more accurate density on concave corners, thus the grid resolution can be reduced.

After the code is numerically validated on static droplets, on droplets deformed under a simple shear, and on simple geometries. Finally, we perform simulations on a Berea sandstone sample [6] to understand dynamics behaviour of immiscible fluids in porous media.

Acknowledgements

I would like to express my gratitude to Prof Yonghao Zhang and Dr Monica Olivera for giving me the opportunity to realise my dream. I am thankful to the Mechanical and Aerospace Engineering department of the University of Strathclyde for their study facilities and their financial support.

I would like to thank my supervisor Prof Yonghao Zhang for financing this project and supporting me with invaluable advice throughout. I am really grateful to him for that help. I would also like to thank him and Prof Kai Luo for giving me the opportunity to present and attend UKCOMES workshops and getting for access to ARCHER.

Not forgetting all the people involved in the James Weir Laboratory and especially my second supervisor Dr Tom Scanlon who shared his knowledge and his Scottish culture, and supported me throughout my PhD. I would especially like to thank Dr Nikolaos Ioannou who welcomed me, taught me such a lot and became a dear friend (outside of the University). Miss Qingqing Gu and Dr Minh Tuan Ho helped me during these three years of research and I would like to thank them for that and for their friendship.

My desire to do a PhD came about after an internship in research at EDF with Dr Mugurel Stanciu and the motivation and inspiration from the following great researchers: Prof Christine Rousselle and Dr Ivan Fedioun at PRISME and ICARE Institutes, respectively. I am very glad they encouraged me to do this research and I would like to express my gratitude to them.

Finally, my friends (Léonor, Mercedes, Faidon, Bagdagul, Ferdin, Irene, Pascal, and more) have always given me happiness with the added help of sweets and coffee during these three years. Last but not least, the people who have never failed to support me are my family and I would like to acknowledge this with gratitude.

Scientific contributions

With peer review

Submitted article

- 2018 Physical Review E An improved boundary condition at a low grid resolution and Reynolds number

International conferences

Poster

- 2017 InterPore Investigation into the effect of confinement and mobility at pore scale for real rock.

Presentation

- 2017 ICMMES Smooth contact angle treatment at “stairs” surfaces.

National conference

Poster

- 2016 29th Scottish fluid mechanics meeting Direct simulations at pore-scale for engineering applications.

Without peer review

National conference

Presentation

- 2016 UKCOMES meeting Implementing contact angle model at "stairs" surfaces.

Contents

List of Figures

List of Tables

Abbreviations

BGK Bhatnagar-Gross-Krook

CFD Computational Fluid Dynamic

CM Central Moment

CPU Central Processing Unit

CSF Continuum Surface Force

DNS Direct Numerical Simulation

DSMC Direct Simulation Monte-Carlo

DVM Discrete Velocity Method

EOR Enhanced Oil Recovery

FD Finite Difference method

FEM Finite Element Method

FVM Finite Volume Method

GL Gauss-Legendre

GLL Gauss-Lobatto-Legendre

Kn Knudsen number

LBM Lattice Boltzmann Method

LGA Lattice Gas Automata

MPI Message Passing Interface

MRT Multiple Relaxation Time

NO_x Nitrogen oxides

NS Navier-Stokes

PDE Partial Differential Equation

REV Representative Elementary Volume

SEM Spectral Element Method

VOF Volume Of Fluid

Chapter 1

Introduction

1.1 General concepts for reservoir studies

For this first section, an introduction of the oil and gas in petroleum reservoirs from the geological point of view to the simulation of the extraction process will be presented.

1.1.1 General description of a petroleum reservoir

A petroleum reservoir is a field in the ground which contains oil and/or gas. A petroleum reservoir will be simplified to a reservoir in the rest of this thesis. The typical size of a reservoir is several km^3. They are located around the world and each field has different quantity of oil and/or gas. A representative figure of the known oil & gas reservoir is shown in Figure 1.1.

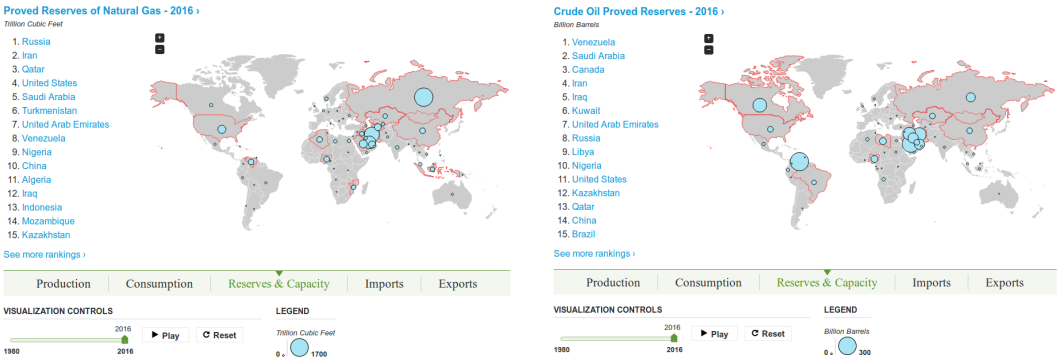

Figure 1.1: Oil & gas reserve in the world in 2016 [7].

The extraction process has three recovery steps: primary, secondary, and Enhanced

Oil Recovery (EOR). The cheapest primary step utilises the natural pressure inside the reservoir and releases the oil and/or gas when the well is drilled. Less than 15% can be recovered with the primary recovering. The secondary recovery needs water flooding i.e. forced water injection and 15% more of oil can be extracted [13]. With these two first conventional techniques, we can extract only 30% in the best scenario but probably less than 15%. Extensive research has been done to increase extraction rate with an additional step called EOR and the commonly used EOR techniques are presented in [14].

1.1.2 Fluids in oil & gas reservoirs

The properties of oil & gas fluids extracted from reservoirs are very different which strongly depend on temperature, the site of extraction and pressure. For instance, Table 1.1 shows the different properties of heavy oils.

	Viscosity (cp[1])	**Density (kg/m^3)**	**API**
Heavy oils	10^1 to 10^2	903-945	18° to 25°
Extra-heavy	10^2 to 10^4	930-1020	7° to 20°
Bitumen	10^4 to 10^6	985-1020	7° to 12°
Oil shale	more than 10^6		

Table 1.1: Heavy oil properties at 60°F (≈ 16°C) [13].

The temperature in the ground can be very different depending on the location principally due to the depth of the reservoir but it can also be affected by geothermal activities. Indeed, it was reported the temperature can be between $57°C$ to $340°C$ Celsius with a range of depth from $300[m]$ to $9000[m]$ [15]. The ground temperature of crude oils can also be elevated due to microbial activities [16].
Knowing the ground temperature is highly important for the viscous properties of the oil. Some examples of hydrocarbons are shown in Figure 1.2. As it can be seen, the viscosity of liquids decreases due to the attractive interaction of atoms is weaker and the viscosity of gas increases due to the collision frequency increases.

[1] 1 centipoise = 10^{-3} Pa s

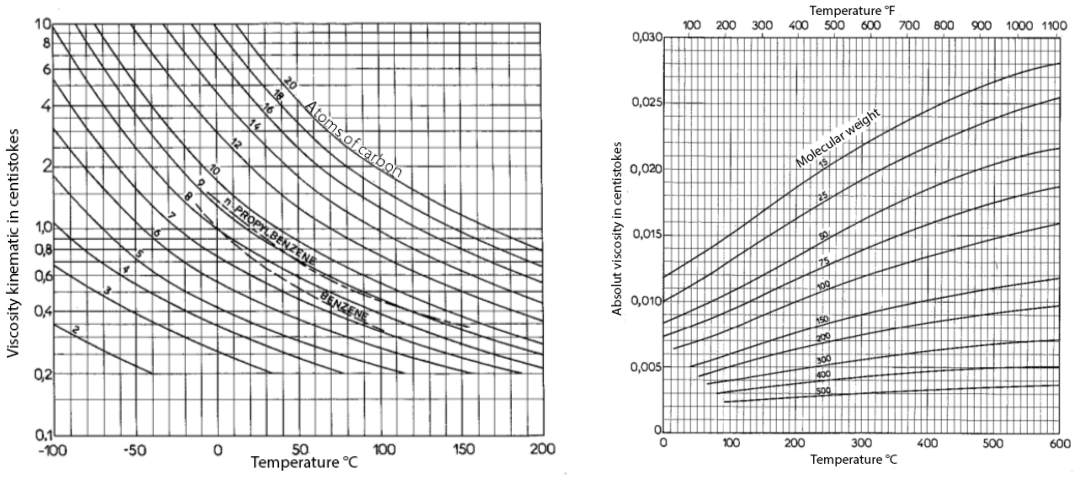

Figure 1.2: Examples of the temperature evolution of the kinematic viscosity for liquid and gas hydrocarbons under 1 atm [8] (Translated into English).

Therefore, in case of thermal EOR, the evolution of the fluid properties (viscosity, density, heat capacity and so on) with the temperature must be taken into account.

1.1.3 Reservoir simulations

To simulate the two-phase flows in reservoirs, the first step is to characterise a sample (pore-scale) then upscale the results to a Representative Elementary Volume (REV) sample (homogenisation) then simulate the reservoir to evaluate the oil production as shown in Figure 1.3. These three steps will be introduced.

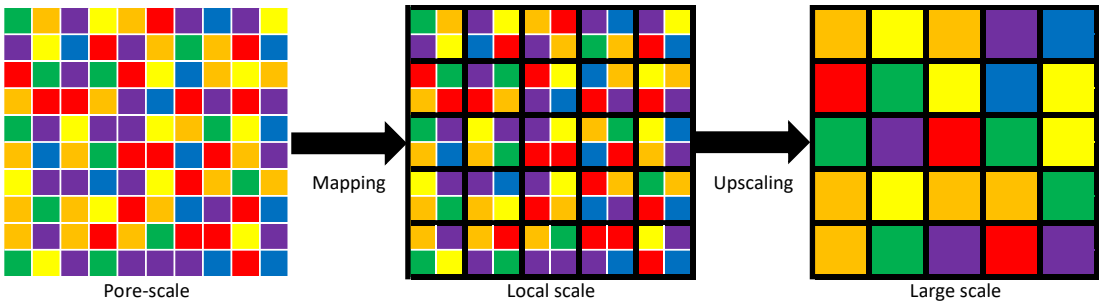

Figure 1.3: Representation of the different scales in a reservoir.

1.1.4 Pore-scale methods

Simulations at the pore-scale are common for single-phase flows since decades. With the development of multiphase models and computer resources, pore-scale two-phase

flow simulations become popular. For single-phase flows, the results, obtained from the pore-scale simulations, are quite well understood for conventional oil & gas at the primary extraction step.

The behaviour of unconventional oil & gas e.g. oil sands, extra heavy oil, shale gas/oil, etc. or even the secondary extraction step is not well understood. Indeed, the unconventional oil & gas is generally located in very narrow pores and rarefied gas conditions can appear during the extraction. The major problematic is: how the rarefied gas conditions affect the flow and when the rarefied gas conditions appear. The multiphase phenomena, appearing in porous media at pore-scale, are not well understood and how they affect the upper (local and large) scales[2] are even less known. In this thesis, we are trying to bring more knowledge at the local scale with a more realistic contact angle treatment.

1.1.4.1 Upscaling methods

As the reservoir size is too big to be represented at the local scale and most of the geometry is unknown, a coarse mesh is needed and then the simulation of the reservoir takes place at the large scale. Thus, up-scaling methods are used to homogenise the pore-scale to the local scale (Figure 1.3).

The cells of the coarse mesh should be a REV. Marle [9] proposed to find the REV of the sample by measuring the porosity as a function of radius as Quintard & Whitaker [17] had shown the importance of the radius in averaging. When the radius is too small (less than r_1 in Figure 1.4), the calculated/measured porosity has a lot of dispersion between two radius sizes. When the radius is too large (more than r_2 in Figure 1.4), the porosity is not representative of the sample. A representation of this proposition is shown in Figure 1.4. In practice, the size is often much larger for limiting the simulation time. This consideration is for single-phase flow but there is not such as well-established technique for two-phase flows. Thus, in multiphase flows, the REV becomes the same by lack of knowledge.

For a real reservoir, many pore-scale samples are not known in the local scale. Thus,

[2]Local scale is also known as Darcy scale. If the sample is REV, the local scale is skipped. The large scale is also known as reservoir scale.

there is a lack of flow properties to determine the local scale. A stochastic approach is used to determine them based on the known samples [18]. Thus, errors in the pore-scale simulations will directly impact the whole reservoir. However, the physics at the

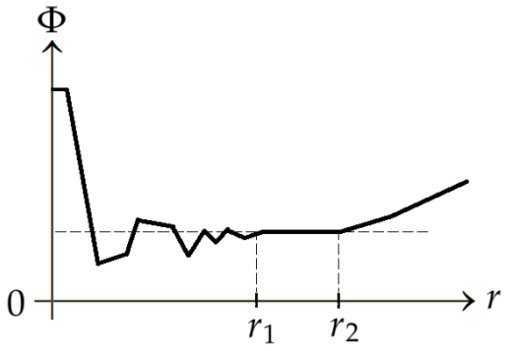

Figure 1.4: Porosity in function of radius [9].

local and large scales are different. At the local scale, the Navier-Stokes or Boltzmann equations are valid, but it is common to use the Darcy's law at both scales. To upscale from the pore-scale, an optimisation technique is commonly used. The idea is to define an objective function and minimize it. This function has to take into account the results/experiments at the pore-scale and find the correct parameters at the large scale to reproduce the effect of the local scale. Thus, a new set of relative permeability (Equation 2.18) is defined which are called pseudo-functions which can be static [18] or dynamic [18, 19].

1.1.4.2 Reservoir methods

To determine and optimise the oil production of the reservoir, it is common to simulate the flow with the Darcy's law and a mass conservation equation, as in Open Porous Media platform. Several models can be added such as polymer models for taking in account of dead-pores, absorption and so on [20].

1.2 Why using Lattice Boltzmann Method?

The classical scheme for Computational Fluid Dynamic (CFD) is the Finite Volume Method (FVM) which is a cell-based method. However, other schemes with a cell-based

method exist such as Finite Element Method (FEM) which is more appropriate for morphed meshes, Spectral Element Method (SEM) which is more used for turbulence analysis (high order schemes) or Finite Difference Method (FDM) which gets the most accurate results for a mathematical point of view but needs a Cartesian mesh (high calculation cost) for high order schemes. Therefore, the spectral methods are considered as the reference of numerical schemes for classical CFD (continuum mechanics).

LBM is a mesoscopic particle-based method. Thus, it is a discrete method and not a cell-based method as often used in continuum methods. In addition to macroscopic flow properties, LBM can also provide some properties of the fluid at the microscopic scale, so it works for nearly rarefied gas flow to continuum flow. This strength is very useful for porous media and multiphase flow.

Indeed, the flow inside a porous medium could be classified as a rarefied gas flow due to the size of pores which could be less than the micrometre. At this size of pores, the molecular mean free path starts to be not negligible compared to the size of pores and the fluid should be treated as a rarefied gas. For rarefied gas, the scheme changes in order to capture the small variation of the fluid properties. A porous media contains many walls and LBM treats wall boundary conditions in a straightforward and simple manner.

LBM is suitable for multiphase flow as it is an interface capturing method. Thus, we do not need to track the interface [21] which is one of the biggest challenges for classical CFD for multiphase flow.

1.3 Multiphase flow

Research challenges on the numerical methods (e.g. diffuse interface, instability) and the multi-physical phenomena (e.g. surface wetting, droplet coalescence, interface instability) in porous media, are the focus of the present work.

In fact, multiphase flow is difficult to simulate as it often involves multi-scale flow phenomena. For instance, the interaction between phases takes place at the microscopic

scale but their motion is at the macroscopic scale. To treat this kind of flow, we need to classify them first. A short description of multiphase flow categories is shown in the Table 1.2.

Continuous Fluid	Dispersed Fluid	Examples
Gas	Solid	Aerosol Smoke Suspensions Fluidised bed
	Liquid	Condensation Sprays Frogs Clouds
Liquid	Solid	Suspensions Slugs
	Liquid (non miscible)	Emulsions
	Gas	Foam
Liquid–Liquid		Oil extraction

Table 1.2: Multiphase flow categories.

The behaviour of the flow, called flow regime, changes depending on flow conditions and fluid proprieties, which is shown in Figure 1.5. An example of fingering due to the low surface tension is also shown in Figure 1.5.

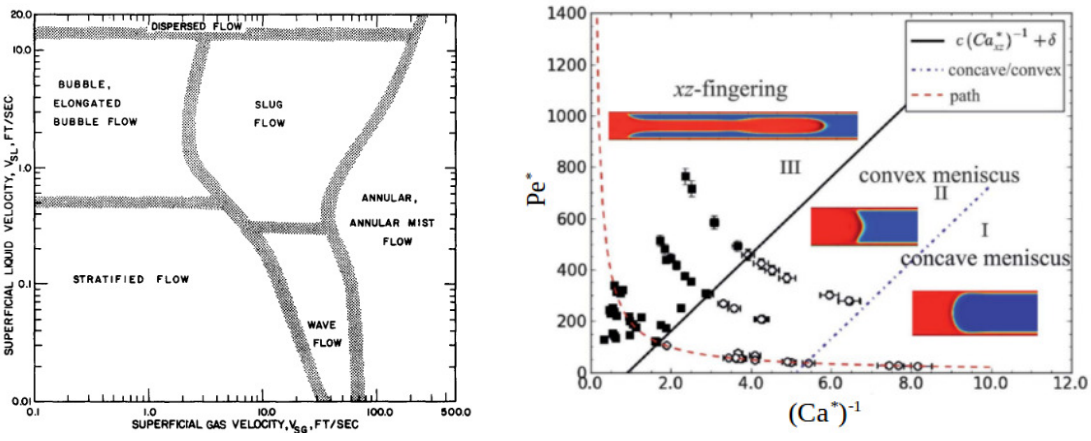

Figure 1.5: On the left, flow regime map for 2.5 cm diameter horizontal pipe air-water flow at atmospheric conditions, Mandhane et al. [10] and on the right, the shape of the interface in the xz–plane for a viscosity contrast $r = 0.4$ as a function of the scaled capillary and Péclet numbers, Setu et al. [11].

For classical CFD to simulate two-phase flows, a front-tracking (Lagrangian) or front-capturing (Eulerian)method must be applied. The classical techniques are: the marker-based method for front-tracking and the Level-Set and Volume-Of-Fluid (VOF) methods and more recently the Immersed Boundary Method (IBM) for front-capturing. In LBM, the method is an interface capturing method. Therefore, the method does not need a front-tracking or front-capturing method.

1.4 Research objectives

This research is included in an oil & gas research project, collaborating with Heriot-Watt University, and led by Professor Yonghao Zhang and Dr Tom Scanlon from James Weir Fluid Laboratory at the University of Strathclyde in mechanical aerospace engineering department.

My contribution to this project is mainly to develop a mesoscopic platform to simulate flows in porous media. My platform is already used by another PhD student, Miss Qingqing Gu and some undergraduate students.

The second objective is to use binary images to generate the mesh. Indeed, the pre-treatment stage in CFD applications is long and not obvious for complex geometries. Using the binary images, this stage is reduced to almost no time whatever the complexity of the geometry.

The third challenge is to handle single and two-phase flows. Plenty of applications use porous media for single or two-phase flows. In the future, more and more applications will appear with new techniques to produce products more and more compact. Indeed, porous exchangers started to replace traditional exchangers such as tube and shell exchangers. For instance, we can find them in the car industry or heating systems for buildings.

The fourth objective is to have a massive parallel platform to get quick results for engineering domains. Solving a real engineering case requires a big domain (several

million or billions of nodes) and a relatively long physical time (several million or billions of iterations). To be able to get the result in a reasonable time-scale, we need to use a massively parallel approach. We decided to use a full MPI approach to run on HPC with a large number of processors (several hundred).

The last objective is to get efficient and accurate results. This is the reason we choose to use LBM. It is an efficient method for two-phase flows and for a massively parallel approach. The accuracy will greatly depend on the grid size. Compared to Navier-Stokes solver, LBM needs a much finer mesh. Therefore, we could get some discrepancy, especially in two-phase flows. However, LBM can handle smaller capillary numbers compared to the Navier-Stokes solvers. For example, the solution with LBM will be less affected by spurious currents. In other words, LBM produces less spurious currents.

1.5 Thesis outline

This thesis is divided into four chapters.

In chapter 2, the fluid and porous media properties used will be described. This is important to analyse correctly the results without violating the assumptions made in the definition of the fluid and porous media properties.

In chapter 3, a short review of numerical methods is provided for classical methods and more details are given for the lattice Boltzmann Methods and the different techniques used in this thesis.

In chapter 4, the numerical methods will be discussed and analysed, especially on the parallel efficiency, the improvement of the boundary treatment and the errors in two-phase flows.

In chapter 5, the contact angle treatment will be presented, validated and applied on a 2D Berea sandstones [6].

Chapter 2

Fluid and porous media properties

This chapter covers all the characteristics needed to define the numerical parameters. The first section covers briefly the characteristics of fluids used or presented in porous media. The second section describes the physical characteristics of porous media.

2.1 Fluid characteristics

In this section, the three major fluid properties which are density, viscosity and surface tension, and the two-major dimensionless number which are the Reynolds and the Capillary number, which will be described in detail.

LBM is based on a gas kinetic approach. However, the simulations in this thesis are for liquids. Thus, we will keep a low Mach number [1]to be near the incompressible limit. To explain the effect on the fluid properties, the gas and liquid properties will be described. The properties of the gas will be based on the hard sphere model with the

[1] $M = u/c$, where M, u, and c are the Mach number, the velocity of the fluid, and the speed of sound, respectively.

ideal gas law and for liquid, it will be empirical laws due to lack of theory.

2.1.1 Density

This fluid property, density, represents the mass of molecules per unit volume. In case of a gas (using the ideal gas law), the density can be determined as [22]:

$$\rho = \frac{p}{r\,T} = \frac{p\,m}{k_B\,T}, \tag{2.1}$$

where ρ, p, T,r,m, and k_B are the density, the static pressure, the temperature, the specific gas constant, the molecule mass, and the Boltzmann constant, respectively.
In a liquid, the fluid can be considered as incompressible[2], thus the density is constant with a variation of pressure, but the thermal expansion needs to be used to take into account the change of density due to the temperature[3].
In the thesis, we consider isothermal flows at low Mach number. As the density of oil is close to the water (Table 1.1), we consider the oil and water to have the same density here.[4]. Thus, we do not consider the change of density and a reference density set to 1 [lu].

2.1.2 Viscosity

The viscosity can be estimated for a simple (monatomic) gas by using the relation of Maxwell [22]:

$$\mu = \frac{1}{3}\,\rho\,u_{mpv}\lambda, \tag{2.2}$$

[2]In case of pressure more than 500 bars, the fluid becomes compressible. In very deep reservoirs or high-pressure systems as the common rails in diesel engines, the compressibility needs to be taken into account especially for acoustic.

[3]If we consider a reservoir at 5000$[m]$ of deep and the data from IAPWS-97, the density of water at 57° and 340°$[c]$ and 500$[bars]$ are 1005.36 and 711.785$[kg/m^3]$, respectively. The variation of density due to pressure at 57°$[c]$ for 1 and 500$[bars]$ are 984.726 and 1005.36$[kg/m^3]$, respectively. Thus, it is clear the temperature affects more than the pressure on the density.

[4]The density can be different due to Equation 2.1 but the interfacial forces do not take it into consideration.

where μ,ρ,u_{mpv}, and λ are the dynamic viscosity, the most probable velocity and the mean free path, respectively. The mean free path can be estimated as

$$\lambda = \frac{k_B\, T}{\sqrt{2}\,\pi\, d^2\, p} = \frac{k_B}{\sqrt{2}\,\pi\, d^2\, \rho\, r}, \tag{2.3}$$

and the most probable velocity as

$$u_{mpv} = \sqrt{\frac{2\, k_B\, T}{m}}, \tag{2.4}$$

where d is the average molecule diameter. More complex formulations were developed to have a better representation of the molecules. For instance, the empirical formulation of Chung in 1984 [23] which provides quite accurate results utilising the kinetic theory. Considering a constant density with the temperature, the variation of viscosity is proportional to $\sqrt{T}$ as shown in Figure 1.2.

In a liquid, the viscosity is commonly based on empirical correlations in a form as:

$$\mu = \exp(A + \frac{B}{T} + C\, T + D\, T^2). \tag{2.5}$$

Physically, the viscosity of liquids decreases when the temperature increases which is the opposite of gas. To get around this contradiction, the viscosity must be an input. Thus, using a kinetic gas scheme such as LBM to simulate liquids leads to modify the most probable velocity, the mean free path, and the mean collision rate (u_{mpv}/λ).

For two-phase flows, the viscosity ratio is defined as, for droplets,

$$\lambda = \frac{\mu^m}{\mu^d}, \tag{2.6}$$

for channels or serpentine,

$$\lambda = \frac{\mu^{out}}{\mu^{in}}, \tag{2.7}$$

and for porous media,

$$\lambda = \frac{\mu^{inv}}{\mu^{dis}}, \tag{2.8}$$

where μ^m, μ^d, μ^{out}, μ^{in}, μ^{inv}, and μ^{dis} are the dynamic viscosity of the matrix, the droplet, outgoing, incoming, invading, and displaced fluids, respectively.

2.1.3 Surface tension

The surface tension represents the anisotropy of intermolecular forces at the interface between two immiscible fluids and is equal to $\sigma = s_n\, e$ where σ, s_n, and e are the surface tension, the normal stress, and the interface thickness (several Ångström), respectively. This property is dependent on the temperature. At high temperature, the surface tension reduces drastically in most cases[5] [25, 26]. However, in this thesis, we consider only isothermal flow with homogeneous phases, so the surface tension will be constant in our simulations.

2.1.4 Dimensionless number

For flow simulations, dimensionless numbers help to characterise the flow. In this thesis, only two well-known dimensionless numbers, the Reynolds and Capillary numbers, are considered in the analysis.

2.1.4.1 Reynolds number

This number is mostly used in turbulence analysis. For instance, the production rate of turbulence in different turbulence models is determined through a local Reynolds number. However, this number is also important for low-speed multiphase flows. Indeed, the Reynolds number compares the inertia forces with the viscous forces as:

$$Re = \frac{\widetilde{U}\,\widetilde{L}}{\widetilde{\nu}}, \tag{2.9}$$

where Re, $\widetilde{U}$,$\widetilde{L}$, and $\widetilde{\nu}$ are the Reynolds number and the characteristic: velocity, length, and kinematic viscosity, respectively.

Therefore, if the Reynolds number is larger than 1, the inertial forces are dominant compared with their viscous forces. With an interface involving in the flow, the stress seen between the two sides of the interface will differ. Indeed, with $Re > 1$, the

[5] For molten metals, the tend can be the opposite [24].

interface will deform due to the inertia, so the analysis will be different from $Re < 1$ i.e. a creeping flow.

In this thesis, the characteristic properties for channels or serpentine are the maximum velocity, the height and the dynamic viscosity of the red fluid. For a porous medium, the characteristic length should be based on the pore sizes which are not known for this study. Thus, only the local Reynolds number has been checked to be less than 1 in several channels of the media.

2.1.4.2 Capillary number

In multiphase flow, the interfacial forces play a significant role especially when those forces are larger than the viscous forces. By taking the energy per surface unity, we get the Capillary number:

$$Ca = \frac{\widetilde{\mu}\,\widetilde{U}}{\widetilde{\sigma}}, \tag{2.10}$$

where $\widetilde{\mu}$,$\widetilde{U}$, $\widetilde{\sigma}$ and are the characteristic: dynamic viscosity, velocity, and surface tension, respectively.

2.2 Porous media

This section describes porous media and defines the porosity, the tortuosity, and the permeability.

2.2.1 What is a porous medium?

A porous medium is a material containing pores (voids). A pore is a small space inside a solid or semi-solid matrix but free of matrix. For instance, a sponge is a porous medium. However, not all porous media are concerned with fluid flows. In fact, a lot of porous media are not permeable to fluids. Therefore, we will restrict the topic to permeable porous media and solid matrix.

Porous media can be found in industrial environments or in nature. In nature, porous media are almost everywhere. For instance, sands and most rocks are porous [27, 28].

In chemical engineering, porous media are often employed for filtering applications as in NO_x converters [29,30] or for reactors as in fluidized bed reactors [31].

The three major parameters to define a porous medium for fluid flow applications are the porosity, the tortuosity and the permeability.

2.2.2 Porosity

The porosity is defined as

$$\phi = \frac{V_p}{V_t}, \tag{2.11}$$

where V_p is the volume occupied by the pores and V_t is the volume of all material. This number shows the proportion of void in the media. However, some pores are not connected to the network and don't contribute to the flow. Those pores should be excluded, and we define the effective porosity as

$$\phi_e = \frac{V_{ep}}{V_t}, \tag{2.12}$$

where ϕ, V_{ep},and V_t are the porosity, the volume occupied by the only pores connected to the network, and the volume of all material, respectively. This number represents the amount of fluid which could be absorbed by the porous media. A small number shows the material is dense and a small volume of fluid could go through it. However, it is less straightforward to obtain this value. So, we will consider only the porosity and not the effective porosity for the rest of the thesis.

2.2.3 Tortuosity

The porosity alone is not enough to indicate the capability of the flow to go through the porous media. Indeed, the network could be well connected and straight, or the opposite. The tortuosity represents this structure property. It is experimentally measurable and two main techniques are often used such as geometrical and electrical conductivity. However, there are several other techniques utilising differently the physical properties[6].

[6]For a straight network of tubes, tortuosity and porosity are equal.

2.2.3.1 Geometrical technique

From a geometrical point of view, tortuosity is the ratio between the mean length from the inlet to the outlet and the length of the sample. So, the method needs to find the "theoretical flow path" lengths between the inlet and outlet then average them. A "theoretical flow path" length is the shortest distance to reach the outlet at a one inlet location. Thus, several lengths exist along the inlet boundary and determining them is not straightforward for a complex geometry. This way of determining the tortuosity can be used to compare samples and understand their structures [32, 33] but it is not clearly relevant for hydrodynamic study.

2.2.3.2 Hydraulic/Electric techniques

The tortuosity can also be measured by using the electrical conductivity between the inlet and the outlet of the porous media and comparing to the real electrical conductivity of the fluid. It is defined as

$$T = \phi_e \frac{\sigma_f}{\sigma_p}, \tag{2.13}$$

where T is the tortuosity, σ_f is the electrical conductivity of the fluid and σ_p is the electrical conductivity of the porous media. It can be also estimated with a heat flux with the same principle.

The hydraulic tortuosity is more difficult to calculate. The idea is to calculate the square of the ratio between the actual path length and the apparent path length. This is not a simple task, which differs from the electrical or thermal calculations [34].

Due to the heterogeneity of the material, the flow takes a preferential path [32]. To fill all the pores, the time is much higher than the time needed to evacuate of the media [35].

2.2.4 Permeability

Another important parameter is the permeability that represents the difficulty for the fluid to go through the porous media by an applied pressure. It was defined by Darcy [36], when he sought a law to design the fountains and the running water in the

city of Dijon where the water came directly from a source with pipes, as

$$K = \frac{Q}{S}\mu\frac{L}{\Delta P}, \tag{2.14}$$

where K, Q, S, L, and ΔP are the permeability, the volume flow, the section, the length of the medium, and the pressure drop, respectively. This law is for a sample with only one phase and usually called the absolute permeability. Thus, this law needs to be generalised and extended to multiphase.

2.2.4.1 Generalised form

To take into account of anisotropy of the sample and be able to discretise, the permeability needs to be generalised as:

$$K_{ij} = -\frac{u_i\,\mu}{\partial P/\partial x_j}, \tag{2.15}$$

where K_{ij}, u_i, and P are the single-phase permeability, superficial velocity, and the static pressure, respectively. This form of the permeability is a tensor of order 2 which considers, everywhere, that the flow creeps [7] with only one phase. However, it is common to consider only low Reynolds number i.e. laminar flow.

2.2.4.2 Multiphase form

In order to add one or more phases to Equation 2.15, it needs to assumed that each phase behaves as a single-phase so the equation becomes:

$$K_{ij}^k = -\frac{u_i^k\,\mu^k}{\partial P^k/\partial x_j}, \tag{2.16}$$

where the superscript ^{k} is the phase index. However, the analysis of each phase is not easy and a relative permeability K_r^k is introduced as:

$$K_{r\,ij}^k\,K_{ij} = -\frac{u_i^k\,\mu^k}{\partial P^k/\partial x_j}. \tag{2.17}$$

[7] Reynolds needs to be less than 1. So, the inlet/outlet can be reversed in single-phase flow.

So, the relative permeability is:

$$K_{r\,ij}^{k} = -\frac{u_i^k\,\mu^k}{(\partial P^k/\partial x_j)\,K_{ij}}. \tag{2.18}$$

2.2.4.3 Extension of the definitions

The pressure gradient defined in the Equation 2.15 can be obtained by at least two ways:

- Experimentally as in Equation 2.14
  $\frac{\partial P^k}{\partial x_j} = \frac{\Delta P}{L}$
- Finite volume so the average of the pressure gradient in the domain
  $\frac{\partial P^k}{\partial x_j} = \frac{\sum_{j=1}^{n}\left(V_j\,(\partial P^k/\partial x_j)\big|_j\right)}{\sum_{j=1}^{n} V_j}$
  for n fluid nodes [8] and each fluid node has a volume V_j [9].

The superficial velocity is the corresponding velocity for the same mass flow passing through the volume of all material [10] i.e. the void-only porous media. Therefore,

$$u_i^k = \phi\; u_i^k\Big|_{pore}, \tag{2.19}$$

where

$$u_i^k\Big|_{pore} = \frac{\sum_{j=1}^{n}\left(V_j\; u_i^k\Big|_j\right)}{\sum_{j=1}^{n} V_j}, \tag{2.20}$$

for n fluid nodes [8] and each fluid node has a volume V_j [9].
However, the superficial velocity can be seen with the flow going inside or outside (inlet/outlet) as in experiment:

$$u_i^k = u_i^k\Big|_{inlet/outlet}, \tag{2.21}$$

but in multiphase flow, this definition can be problematic. For instance, a phase in the domain can move only inside, be injected but not going out, or just go out.

[8] This assumes each node represents a volume and the velocity at the node is constant inside this volume. Moreover, the flow needs to be incompressible.
[9] $\sum_{j=1}^{n} V_j$ is the volume occupies by the pores V_p.
[10] V_t from the definition of the porosity.

Clearly, different definitions of Equation 2.18 can be created. If the idea is to compare with experiments, the best method is to use the pressure gradient based on the difference of pressure between inlet and outlet and use the superficial velocity by the flow going inside or outside. However, if the aim is to use in upscale methods, the integration method will be preferred.

2.2.5 Mobility

This property represents the ability of the fluid to move inside the porous media and it is defined as:

$$M \equiv \frac{K_{r\,ij}^{k}\, K_{ij}}{\mu^{k}}. \tag{2.22}$$

We can define the mobility ratio as:

$$M_{ratio} \equiv \frac{M^{dis}}{M^{inv}} = \frac{K_{r\,ij}^{dis}}{K_{r\,ij}^{inv}} \frac{\mu^{inv}}{\mu^{dis}}. \tag{2.23}$$

When the relative permeabilities are equal, the mobility ratio becomes the viscosity ratio. Thus, it is an important parameter to evaluate the ability of the invading fluid to flood the porous media. The oil & gas companies use this ratio to estimate the extraction of oil & gas. The largest mobility ratio gives the best flooding i.e. the best oil & gas production.

2.2.6 Saturation

The saturation is the volume fraction of one fluid which occupies the void of the porous media. For the invading fluid, the saturation is:

$$S_{invading} = \frac{\sum_{j=1}^{n} \left(V_j\, \alpha_j\right)}{\sum_{j=1}^{n} V_j}, \tag{2.24}$$

for n fluid nodes [8] and each fluid node has a volume V_j [9]. α_j is the local mass fraction of the invading fluid.

Chapter 3

Numerical methods

This chapter covers the numerical methods from classical CFD to LBM for single-phase and two immiscible fluids flow.
Different numerical methods can be chosen depending on the required accuracy and the flow physics involved. A short review will be presented to introduce the different methods. The second part describes the traditional methods for continuum flows and the last part discusses the method used in this thesis.

3.1 Introduction

Experiments are not always easy to perform, and they can be time-consuming, costly, and not feasible (no gravity, no interactions with walls, no measurement techniques, etc.). Therefore, simulations can replace or complement experiments. It was more than 60 years ago that numerical methods were developed [37]. However, in the beginning, the computer could not handle complex domains and complex equations. For instance, simulations considering a potential flow were very common 20-30 years ago, which is still of use for design optimisations. Indeed, the method is so quick to solve that can be used to test a lot of configurations. However, the results are mainly qualitative and not predictive.

With the development of High-Performance Computing (HPC), the Direct Numerical Simulation (DNS) with the Navier-Stokes (NS) solvers became popular. We are now able to simulate a wing at the Reynolds number larger than 10^6. However, simulation of two-phase flows using DNS is still rare at moderate Reynolds number. Developing numerical methods to handle this kind of flow efficiently, with a Massively Parallel approach is consequently important.

The numerical methods should predict the physics involved in a specific domain and they can use a model or the methods themselves to represent it. For instance, a chemical reaction can be solved at the molecular level, the continuum level or others. However, the calculation costs can be too high at the molecular level due to the number of molecules involved in the system or the physical time is too large, typically more than 1 ms. In case the number of molecules is reasonable as at very low pressure or at very narrow channels and a physical time is small, it is possible to simulate at the molecular level. Otherwise, a continuum approach with a model can be used.
However, using pure molecular or continuum approaches can show up limitations. So mesoscopic or hybrid approaches become important. A general description of mesoscopic methods for gas is given in the Appendix A.

3.1.1 From free molecular to continuum flow regimes

When the gas molecules rarely collide, the flow is in the free molecular regime. When the molecules of fluid collide very frequently, it is in the continuum regime. If the molecules are in constant collisions, the matter is in the solid state. To determine the flow regime, it is common to use the dimensionless Knudsen number (Kn). The most common definition for Kn ($Kn = \lambda/L$) is to compare the mean free path with a reference length of the domain as the height of a channel. However, this general definition cannot take into account all the cases where the rarefaction appears for instance, around a shock wave or a very small particle. Rarefaction due to shock waves are more critical in liquids but it is rare due to the high speed of sound in liquid [38]. In this case, the reference length should be local and can be approximated by the gradient of pressure or velocity. For a very small particle, the drag is reduced due to

the rarefaction [39]. Cunningham proposed a model to take it into account and derive from the Stokes' law.

3.1.2 Macroscopic methods

Numerical methods for continuum flow regime have existed for several centuries [40–42] such as the well-known Euler equations where the Eulerian description comes from. Indeed, Euler used the spatial derivatives to represent the motion. At this time, the Lagrangian description was the custom i.e. to represent a motion, the fluid particles were followed in time and space. In order to solve it numerically, computer resources were needed to be developed. Therefore, the development of codes to simulate a flow with Navier-Stokes equations started around 1970. Recently, it is common to use CFD methods to simulate continuum flows. The two main approaches are the Smooth Particle Hydrodynamics and the Navier-Stokes.

3.1.2.1 Smooth Particle Hydrodynamics

The method was developed by Lucy [43] and Gingold and Monaghan [44] in 1977. It is a Lagrangian method where the particles represent a volume of fluid (density) and their velocities represent the fluid velocity. Other physical properties can be linked with the particle such as the temperature.
The first step of the method is to initialise the domain with particles which have a mass. Then the method is simple: moving the particles according to their macroscopic properties, apply the boundary conditions and update the macroscopic properties by solving the Euler, the Navier-Stokes, other laws, or other equations.
To enforce the law or the equation, a special operator is used to calculate the macroscopic properties based on a kernel. More details and applications can be found in the references [45–47].

The advantage of this method is meshless and conservation of the mass due to its Lagrangian formulation. However, a lot of drawbacks can show up including high computation cost, low accuracy, instability, and slow convergence [47].

3.1.2.2 Navier-Stokes approach

The Navier-Stokes equations were created, separately, by the engineer Henri Navier in 1823 and by the physicist and mathematician Sir George Stokes in 1845. The equations represent the evolution of a fluid with a viscosity in a domain from classical conservation laws (mass, momentum and energy) in a Eulerian description. It can be considered as an extension of the work of Euler.

3.2 Navier-Stokes equations

Considering a Newtonian fluid with density $\rho(p,T)$ and dynamic viscosity $\mu(T)$ where p and T are the pressure and the temperature respectively, the Navier-Stokes equations can be written in the conservative form with Einstein notation as:

$$\frac{\partial \rho}{\partial t} + (\rho u_i)_{,i} = 0, \tag{3.1}$$

$$\frac{\partial \rho u_i}{\partial t} + \left(\rho u_i u_j\right)_{,j} = -p_{,i} + \tau_{ij,j}, \tag{3.2}$$

$$\frac{\partial \rho e}{\partial t} + \left(\rho e u_j\right)_{,j} = -p u_{j,j} - \dot{q}_{j\,,j} + u_{i,j}\tau_{ij}, \tag{3.3}$$

where:

$$\tau_{ij} = \mu S_{ij} = \mu\left(u_{i,j} + u_{j,i} - \frac{2}{3}u_{k,k}\delta_{ij}\right) \tag{3.4}$$

is the stress tensor and where

$$\dot{q_j} = -\frac{\mu Cp}{Pr}T_{,j} \tag{3.5}$$

is the heat flux due to conduction in the direction x_j. e, Cp and Pr are the internal energy, the heat capacity at a constant pressure and the Prandtl number, respectively.

3.2.0.3 Incompressible Navier-Stokes equations

Assuming the fluid is incompressible and isothermal, we can simplify the equations as:

$$u_{i,i} = 0, \tag{3.6}$$

$$\rho\Big(\frac{\partial u_i}{\partial t} + \big(u_i u_j\big)_{,j}\Big) = -p_{,i} + \mu u_{,ii}, \tag{3.7}$$

or

$$\frac{\partial u_i}{\partial t} + \big(u_i u_j\big)_{,j} = -\frac{1}{\rho} p_{,i} + \nu u_{,ii}, \tag{3.8}$$

and with the density equal to unity,

$$\frac{\partial u_i}{\partial t} + \big(u_i u_j\big)_{,j} = -p_{,i} + \nu u_{,ii}. \tag{3.9}$$

3.2.1 Numerical methods

Several approaches can be used to solve Navier-Stokes equations. Here, the discussion will be only on the discrete representation of the spatial derivative operators using the Spectral Element Method (SEM) and the Finite Volume method (FVM) which, later, will be used to validate the continuum flow simulations.

3.2.1.1 Spectral Element method

SEM is considered as a high-order method. Indeed, the method is based on FEM (Galerkin) approach. Therefore, the integration and the spatial derivative operators are based on an element.

SEM is a particular case of FEM due to the type of polynomials used. In SEM, it is common to consider the basis and test functions from Gauss-Lobatto-Legendre (GLL) and Gauss-Legendre (GL) polynomials [48, 49] for the velocity and pressure fields, respectively. The strong advantage of using that kind of polynomials is their orthogonal properties. Thus, the error (residual) is directly obtained and the Navier-Stokes equations (Equation 3.1 and Equation 3.8) are recovered.

GLL or GL can exploit the advantages of the h and p refinements (mesh size and polynomial order, respectively) to obtain exponential convergence rates [50]. Therefore, to increase the accuracy, the order of the polynomials (commonly chosen between 5 to 15.) should be higher or the size of elements should be smaller. It is clear by using this approach, the solution is integrating over all the elements and the integration is calculated as a sum.
This method gives a very high resolution and provides very good performance for a parallel approach. However, the method is less stable than FVM and requires more calculations. An improvement is to use a Discontinue Galerkin approach to increase the number of element and/or order locally [51]. However, this technique introduces discrepancy between elements due to the interpolation technique between elements and the convergence rates is reduced due to the integration per element instead of over all the elements.

3.2.1.2 Finite Volume method

This method is the most used in the CFD community due to the geometric flexibility. The method represents the properties of the fluid/flow in the cell-centre and each cell represents a volume of fluid. Therefore, the integration is by a cell. By using the Gauss' theorem, the volume integration can be transformed to a surface integral.

For each term in a Partial Differential Equation (PDE), an evaluation of the flux at the boundaries of each cell has to be done. This creates the drawback of the method which is difficult to increase the order of accuracy, especially on an unstructured grid. The method tends to use a Cartesian grid for high-order approximations.

3.2.2 Interface-tracking with front-capturing or front-tracking methods

In this section, we consider an interface between two fluids which needs to be represented. Mainly, those kinds of flows are liquid-liquid or gas-liquid. The front-capturing (Eulerian approach) or front-tracking (Lagrangian approach) is used to describe free-

surface flow, stratified flow, droplets or bubbles dynamics[1]. The front-capturing approach includes Volume Of Fluid and Level Set methods and the front-tracking includes Marker-based method.

3.2.2.1 Volume Of Fluid

VOF is a Eulerian technique which considers the volume fraction $\psi(x,t)$ of each phase in each cell to be transported. The transport equation is

$$\frac{\partial \psi}{\partial t} + u\psi_{,j} = 0 \tag{3.10}$$

in case of no injection, well or phase change.
The macroscopic velocity u is calculated by the Navier-Stokes equations with a source term for the interfacial forces. In case of incompressible fluids, the continuity equation remains the same equation as Equation 3.1. The momentum Equation 3.8 is modified.

$$\rho\Big(\frac{\partial u_i}{\partial t} + \left(u_i u_j\right)_{,j}\Big) = -p_{,i} + \left(\mu\left(u_{i,j} + u_{j,i}\right)\right)_{,i} + f_\gamma, \tag{3.11}$$

where f_γ is the Continuum Surface Force (CSF) [3]

$$f_\gamma = \sigma\kappa n\delta_s. \tag{3.12}$$

A reconstruction of the interface is needed for VOF. Several approximations can be used. However, the reconstruction is based on the normal of the interface, which is rarely calculated correctly, leading to spurious current and a wrong calculation of the CSF.
It is possible to remove the reconstruction [52] by using a special approximation of the viscosity and numerical schemes. The main advantage of this technique is to ensure the mass conservation.

[1]The number of bubbles or droplets need to be limited due to computational cost.

3.2.2.2 Level Set

This method uses the transport Equation 3.10 and defines the level set function $\psi(x,t)$ as a smooth function which is continuously differentiable and with the condition at the interface

$$\psi(x,t) = Cst. \tag{3.13}$$

In the original work of Osher and Sethian [53], the constant was chosen to be zero. It is usual to set the level set function as the distance (signed) to the interface. A Heaviside distribution or a smooth Heaviside distribution is used to calculate the density and viscosity at the interface. The smooth Heaviside distribution is used to take into account the thickness of the interface. The momentum equation is the same as in VOF methods (Equation 3.11). The CSF is based on the level set function $\psi(x,t)$ and therefore, the delta distribution needs to take into account the Heaviside or smooth Heaviside distribution. Clearly, the Level set method does not ensure the mass conservation but can represent the sharpness of the interface. It is also possible to combine VOF and Level Set Methods to get the advantages of both methods i.e. the mass conservation and the sharpness of the interface).

3.2.2.3 Marker-based method

This Lagrangian technique places markers (massless particles) on the interface and which move them with the flow [54]. The interface is represented by a function between two markers in two dimensional, generally a linear function and by several markers in three dimensional, generally triangles [55]. Figure 3.1 represents a two-dimensional example of the technique. The drawback of the method is that the mass conservation is not guaranteed, and the calculation cost is high to track the markers.

3.3 Lattice Boltzmann method

This section describes the method used in this thesis. First, a synthetic explanation where the method comes from will be described, then LBM itself from the Boltzmann equation, LBM to Navier-Stokes, then the boundary conditions in LBM and the last

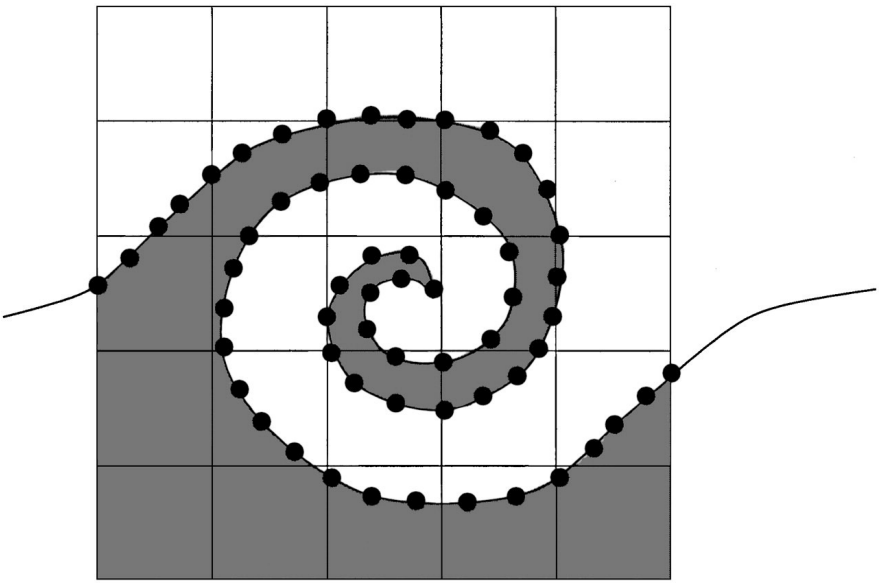

Figure 3.1: Representation of the Front-Tracking technique [12]

part, the multiphase flow models in LBM framework.

3.3.1 Historical development

The LBM was originated from Lattice Gas Automata (LGA) which is a discrete (Boolean variable) particle kinetic method. The aim of this method is to simulate the gas (particle) kinetic by a simple way to investigate some of its proprieties such as mass and momentum. The model is based on a lattice with a maximum of particles at each lattice site and a Fermi-Dirac distribution. Each particle has one of the unit velocity vectors and each particle must have a different velocity. Otherwise, those particles are excluded. The evolution in time is realised by a streaming and a collision of the particles.

The first (LGA) scheme was from Hardy, Pomeau, and Pazzis (HPP model) in 1973 [56] with an infinite square lattice, four-unit velocity vectors and a maximum of four particles at each site. Frisch, Hasslacher, and Pommeau (FHP model) in 1986 [57] used an equilateral triangular lattice, six-unit velocity vectors, and one particle at each site. This symmetrical representation helps to recover NS. An extension in 3D (Face Centered HyperCube model) was proposed by d'Humière [58]. However, those models are noisy by using Booleans variables and have a lack of Galilean invariant due to the

Fermi-Dirac distribution.

The Lattice Boltzmann Method replaces the discrete particle (Boolean variables) by single-particle distribution functions (real variables), the Fermi-Dirac distribution by the Maxwell-Boltzmann distribution, and collide the particles by a Boltzmann approach [59, 60]. However, the collision operator stays non-linear. The modern LBM has shown up by using the Bhatnagar-Gross-Krook operator (BGK) [61–65].

3.3.2 Principles of Lattice Boltzmann method

This subsection describes the LBM included the link between Boltzmann equation and LBM, the major collision operators and equilibrium distribution, and the way to recover NS from LBM.

3.3.2.1 From the Boltzmann equation to lattice Boltzmann method

The Boltzmann equation is the base of the kinetic theory for gases. In $\mathcal{H}$ space (also known as phase space), the Boltzmann equation is written as

$$\hat{\mathbf{L}}[f] = \mathbf{C}[f], \tag{3.14}$$

where $\hat{\mathbf{L}}$ is the Liouville operator, $\mathbf{C}$ is the collision operator and f is a single-particle distribution function. In non-relativistic form, the Liouville operator is written as

$$\hat{\mathbf{L}}_{\mathrm{NR}} = \frac{\partial}{\partial t} + u \cdot \nabla + \frac{\mathbf{F}}{m} \cdot \frac{\partial}{\partial \mathbf{u}}. \tag{3.15}$$

Therefore, the classical form for the non-relativistic form of the Boltzmann equations is

$$\frac{\partial f}{\partial t} + u \cdot \nabla f + \frac{\mathbf{F}}{m} \cdot \frac{\partial f}{\partial \mathbf{u}} = \mathbf{C}[f], \tag{3.16}$$

where u is the free particle velocity, $\mathbf{F}$ is an external force and m is the mass of a

particle.

To move from real gas (Boltzmann equation) to a simplified model (lattice Boltzmann equation), a lattice network is defined, not necessary Cartesian, and particle velocities are restricted to a set of discrete velocities. The general non-relativist[2] form of the lattice Boltzmann equation is

$$\frac{\partial f_i}{\partial t} + e_i \cdot \nabla f_i + \frac{\mathbf{F_i}}{m} \cdot \frac{\partial f_i}{\partial \mathbf{e_i}} = \mathbf{C}[f_i], \tag{3.17}$$

where e_i is the particle velocities in the direction i of the set of discrete velocities, F_i is an external force in the direction i.

If we assume the particles have no external force[3] and cannot be off-lattice, we can rewrite the equation as

$$f_i(\vec{x} + \vec{e}_i \Delta x, t + \Delta t) = f_i(\vec{x}, t) + \Omega_i(f_i(\vec{x}, t)), \tag{3.18}$$

where Ω_i is the LBM collision operator.

3.3.2.2 Collision operators

The collision operator could be treated in several ways. The common collision operators for LBM are: Bhatnagar-Gross-Krook (BGK), Multiple Relaxation Time (MRT), Central Moment (CM), and Entropic. However, the most common way is the BGK collision operator [66].

BGK collision operator

The idea is to replace the non-linear collision operator by a linear collision[4] operator based on a relaxation factor to simplify the collision term. Applying this to LBM, we

[2] Non-relativist will be used until the end of the review and will not be mentioned anymore.

[3] Which is wrong due to the gravity but in most cases, the gravity is insignificant in single-phase flows but not in two-phase flows when the densities are not equal. Obviously, in two-phase flows, the external force has to be added.

[4] It is linear when the relaxation time does not change i.e. when the viscosity is constant, otherwise it is quasi-linear.

get the LBGK model [61–63] and is written as

$$f_i(\vec{x} + \vec{e}_i \Delta x, t + \Delta t) = f_i(\vec{x}, t) + \frac{f_i(\vec{x}, t) - f_i^{eq}(\vec{x}, t)}{\tau}, \tag{3.19}$$

where τ is the relaxation factor and defined as

$$\tau = \frac{6 \cdot \nu + 1}{2}, \tag{3.20}$$

where ν is the kinematic viscosity and f_i^{eq} is the equilibrium distribution. The general form [64] of the equilibrium distribution function with the second order ($O(u^2)$)is

$$f_i^{eq} = \rho \omega_i \left[a + b\vec{e}_i \cdot \vec{u} + c\left(\vec{e}_i \cdot \vec{u}\right)^2 + d\vec{u}^2 \right]. \tag{3.21}$$

Qian *et al* 1992 [63] gave an analytical solution[5] for the coefficients in Equation 3.21. For the D2Q9 scheme, the coefficients are:

$$f_i^{eq} = \rho \omega_i \left[1 + 3\vec{e}_i \cdot \vec{u} + \frac{9}{2}\left(\vec{e}_i \cdot \vec{u}\right)^2 - \frac{3}{2}\vec{u}^2 \right]. \tag{3.22}$$

More details about the equilibrium distribution will be discussed later in subsubsection 3.3.2.3.

MRT collision operator

The MRT technique [67,68] was created to improve the stability of the BGK approach. Globally, MRT can be seen as a BGK approach per discrete velocity. Indeed, the method reduces to a linear relaxation for each discrete velocity.

In aeroacoustics, the MRT helps to keep the simulation stable with a low shear viscosity. However, the drawback is the augmentation of the bulk viscosity which is in order of the shear viscosity in gas and one or two orders higher in liquids [69]. Therefore, the acoustic waves can be dissipated more than really absorbed.

[5] For a compressible gas at low speed and single-phase flows

The calculation costs are higher than the BGK due to the fact that a matrix product is needed.

Entropic collision operator

BGK and MRT have a wrong assumption: the moments relax at a fixed rate i.e. the collision and the moments have the same basis and $\mathcal{H}$ space. However, the moments move with the flow. At low-speed flow, this error is not important and can be balanced by a finer mesh. For high Reynolds numbers, the calculation cost can be very high with a very fine mesh and could give wrong results. In order to remove this non-desirable behaviour, the relaxation coefficients of each moment are computed in each time step and each grid point in order to minimize the discrete entropy function [70, 71].

The calculation cost is higher for low Reynolds number, but the main issue of this operator is to define the boundary conditions.

Central Moment collision operator

The main idea of this operator is to improve the MRT method towards Entropic collision operator without minimizing the discrete entropy function. To achieve this goal, the MRT moments are shifted to the moving frame and using up to the fourth-order moment to close the system [72]. Mathematically, it is a change of basis and a truncation at the fifth-order moment.

Thus, the Galilean invariance strongly presented in the BGK or the MRT is almost removed [73]. As for the Entropic collision operator, the boundary conditions are not easy to define. Recently, some progress was made to include an external force [74] such as the gravity term.

3.3.2.3 Equilibrium distributions

The equilibrium distribution is assumed to be based on the Maxwell-Boltzmann equilibrium distribution[6]:

$$f_i^{eq} \equiv \frac{\rho}{\left(2\pi/3\right)^{D/2}} \exp\left[-\frac{3}{2}\left(e_i - u\right)^2\right], \tag{3.23}$$

[6] Other choices can be used, for instance to take into account the van der Waals forces.

where D is the spatial dimension and u is the normalised macroscopic velocity by $\sqrt{3RT}$ with T the temperature. Originally, the equation is expressed in terms of energy and not in a density of energy.

Using the above equation is numerically very costly. The most common approach to reduce the cost is to develop the equation in the Taylor series to the second order in u. Thus, we obtain the Equation 3.21 which is:

$$f_i^{eq} = \rho\omega_i\left[a + b\vec{e}_i\cdot\vec{u} + c\left(\vec{e}_i\cdot\vec{u}\right)^2 - d\vec{u}^2\right]. \tag{3.24}$$

Clearly, the equation is compressible, and the speed of sound is $1/\sqrt{3}$. By considering the density as $\rho = \rho_0 + \delta\rho$ and neglecting all density fluctuations with the velocity u, the Equation 3.22 can be rewritten [75] as

$$f_i^{eq} = \omega_i\left[\rho a + \rho_0\left(b\vec{e}_i\cdot\vec{u} + c\left(\vec{e}_i\cdot\vec{u}\right)^2 - d\vec{u}^2\right)\right], \tag{3.25}$$

where ρ_0 is the reference and $\delta\rho$ is the density fluctuation. Thus, we obtain the incompressible form of the equilibrium distribution function.

Considering D2Q9 scheme (two-dimensional square lattice with 9 discrete velocities) [63], the Equation 3.21 becomes the Equation 3.22 which is:

$$f_i^{eq} = \rho\omega_i\left[1 + 3\vec{e}_i\cdot\vec{u} + \frac{9}{2}\left(\vec{e}_i\cdot\vec{u}\right)^2 - \frac{3}{2}\vec{u}^2\right], \tag{3.26}$$

and the Equation 3.25 becomes [75]:

$$f_i^{eq} = \omega_i\left[\rho + \rho_0\left(3\vec{e}_i\cdot\vec{u} + \frac{9}{2}\left(\vec{e}_i\cdot\vec{u}\right)^2 - \frac{3}{2}\vec{u}^2\right)\right], \tag{3.27}$$

where $e_0 = c(0,0)$,$e_1 = c(1,0)$,$e_2 = c(0,1)$,$e_3 = c(-1,0)$,$e_4 = c(0,-1)$,$e_5 = c(1,1)$,$e_6 = c(-1,1)$,$e_7 = c(-1,-1)$,$e_8 = c(1,-1)$ and $w_0 = 4/9$,$w_1 = w_2 = w_3 = w_4 = 1/9$,$w_5 = w_6 = w_7 = w_8 = 1/36$

3.3.2.4 Recovery of the Navier-Stokes equations

Nowadays, the hydrodynamic limits of the Boltzmann equation are an open problem. However, in some special conditions, the limits were proven as for the Incompressible Navier-Stokes by Bardos and Ukai [76].

The first works for recovering the Navier-Stokes equations were done by Hilbert [77] and Enskog [78]. Mathematically, their works are only a formal proof [79]. The Hilbert method consists to seek a formal solution of the Boltzmann equation for a variable Kn from this form

$$f(t,x,u;\epsilon) = \sum_{n=0}^{\infty} \epsilon^n f(t,x,u), \epsilon = Kn. \tag{3.28}$$

By identification, Hilbert obtained a system of equations for $f_0, f_0+\epsilon f_1, f_0+\epsilon f_1+\epsilon^2 f_2$ etc. The idea of Enskog is to identify f_n as a function of the hydrodynamic fields (mass, momentum and energy). Both methods can recover (formally) Euler or Navier-Stokes. More details of those approaches and their errors can be found [79–81]. More details about the hydrodynamic limits of the Boltzmann equation can be found at [82].

However, Chapman-Enskog expansion is really used in LBM. Therefore, the principle of the method for LBM with BGK is to use a Taylor expansion in ϵ up to the second order of the Lattice Boltzmann equation (Equation 3.19). We get

$$\frac{\partial f_i^{eq}}{\partial t_1} + e_i \cdot \nabla_1 f_i^{eq} = -\frac{f_i^{(1)}}{\tau}, \tag{3.29}$$

$$\frac{\partial f_i^{eq}}{\partial t_2} + \left(1 - \frac{2}{\tau}\right)\left[\frac{\partial f_i^{(1)}}{\partial t_1} + e_i \cdot \nabla_1 f_i^{(1)}\right] = -\frac{f_i^{(2)}}{\tau}. \tag{3.30}$$

By using the properties of the moments, some linear algebra and the definition of the equilibrium distribution (for instance, the Equation 3.22), the Equations 3.29 and 3.30 can be identified to the Navier-Stokes equations (Equations 3.1 and 3.2).

3.3.3 Boundary conditions

3.3.3.1 Periodic boundary conditions

The periodic boundary condition is defined as a boundary connected to another boundary which leads to a periodic domain. Thus, in LBM, the particles going outside of the domain enter at the connected boundary.

The classical way to implement this boundary is to copy the particles going outside and add them at the connected boundary. However, this adds a synchronised communication between processors. To improve this lack of efficiency, the periodic boundary condition is implemented in an implicit manner i.e. the communication nodes are modified in the mesh generation to impose the boundary condition. This leads to remove additional treatments usually used in a classical way and thus, periodic nodes behave as interior nodes (inside the domain).

To implement this implicit manner, the node ghost layer of the connected boundary is used and synchronised with the first layer of nodes toward the domain at the periodic boundary condition. Thus, each domain sees the other domain as no boundary. An example of the two ways is shown in Figure 3.2. A source term can be added to represent a pressure drop but the pressure needs to be fixed. This is done by imposing the pressure at the inlet as the half pressure-drop by correcting f_0 of the distribution.

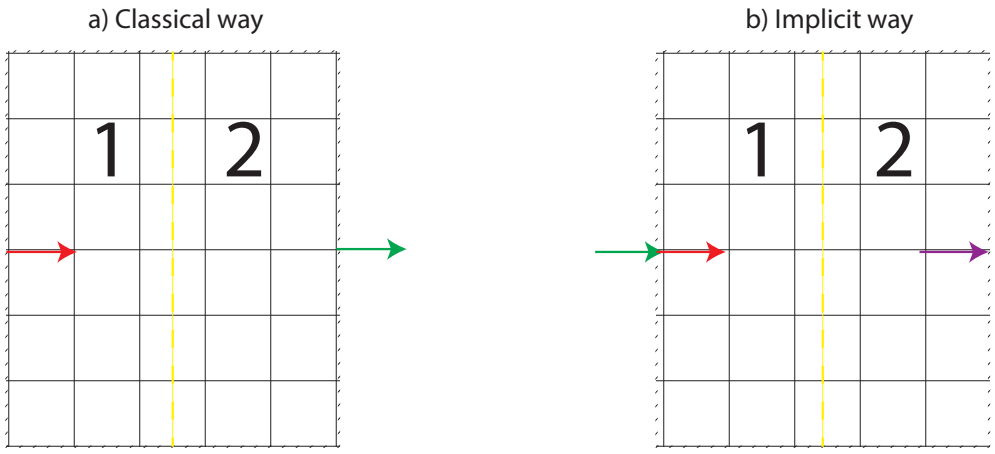

Figure 3.2: Sketch of the left periodic boundary condition for two MPI processes and where the green arrow becomes the red arrow. The red arrow is synchronised with the green arrow for the classical way during applying the boundary condition whereas the green arrow is synchronised with the purple arrow during the time step.

3.3.3.2 Symmetry boundary conditions

This boundary condition is very straightforward. It is just a symmetry of the distribution so naturally there is no flow through the boundary. This condition can be also considered as a specular reflection on a wall.

3.3.3.3 Velocity or pressure boundary conditions

The pressure or velocity boundary conditions are a modification of the momentum. The most common boundary condition for pressure (through the density with an equation of state) or velocity is given by Zou and He [83]. The idea, to determine the unknown discrete velocity, is to consider the non-equilibrium part as a bounce-back on the boundary. However, the method cannot apply at corners due to more unknown variables than equations. In that case, an easy way proposed by Ho [84] is to impose the velocity and the pressure to remove an unknown. For a moving wall, Ladd proposed to use the bounce-back rules and add a source term [85].
More boundary conditions exist for imposing a velocity or a pressure and some other schemes can be found in [86].

3.3.3.4 Wall boundary condition

LBM is very suitable to treat the no-slip velocity conditions at walls due to the simplified kinetic model. For instance, the simplest way to treat the wall is the so-called bounce-back scheme [59, 87]. The idea is that all the particles which hit a wall will bounce-back in the opposite direction. The wall nodes can be also considered as wet nodes, and thus, the collision operator is applied (section 4.2).
In case of rarefied gas, a diffuse boundary condition [88] is used. However, with the low order scheme, the flow field is not captured accurately for a high or moderate Knudsen number i.e. more than 0.1. Using an approach LBM higher order or DVM is more appropriate [89]. Another way to treat the walls is to consider the boundary as a velocity boundary condition. The boundary condition of the Zou and He [83] is used with the velocity set to be zero.

3.3.3.5 Corner treatment

The corners are treated in a relatively similar manner to wall boundary conditions, however, at concave corners, the two discrete particle velocities pointing into the solid in opposite directions represented by the dash lines in Figure 3.3 are unknown. These two discrete particle velocities do not participate in the streaming process but affect the collision process in the D2Q9 schemes i.e. the system of equations at the concave corners are ill-posed. Thus, some choice has to be made to close the system. The simplest approach is to set these to zero, but this leads to a loss of momentum. Another approach is to extrapolate the distribution function at concave corners from the neighbouring nodes [90]. In the present work, the set of equation is closed, specifically for low Reynolds flows, by a macroscopic approach. The assumption of low Reynolds number implies that the diffusive time scale is much greater than the convective ones i.e. the inertia forces are negligible compared to the viscous forces. This enables us to consider

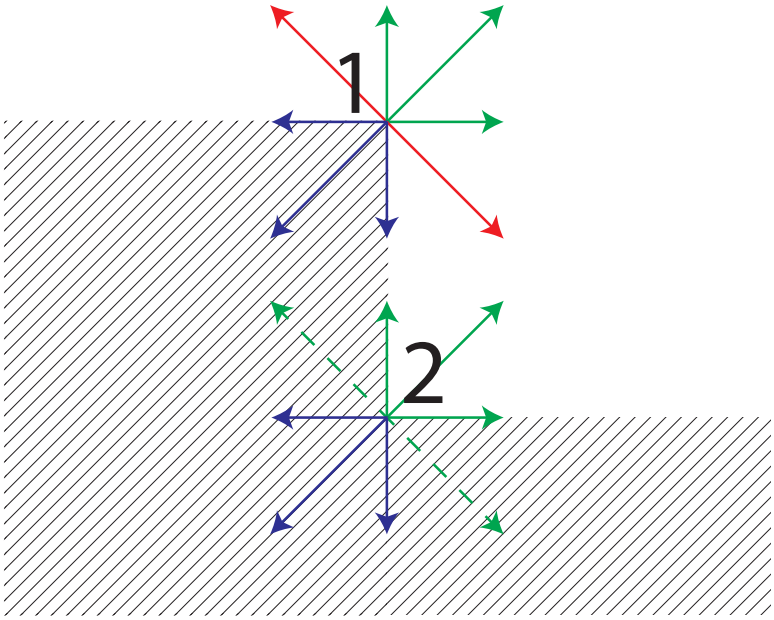

Figure 3.3: Simplify representation of the D2Q9 distribution at convex (1) and concave (2) corners. Blue and green lines are the incoming and outgoing discrete particles, respectively. The red lines represent the incoming and the outgoing discrete particles. The green dash lines are the unknown discrete particles.

the gradient of density is small. Thus, the density at the concave corner is extrapolated by the inverse distance weighting (subsubsection 3.3.5.2) of the three direct neighbours

and the two unknown discrete particles are defined by using the zeroth-moment and assuming the two unknown discrete particles equal, as

$$2f_{un} = \tilde{\rho} - (2\rho_{in} + f_0), \tag{3.31}$$

where, f_{un}, $\tilde{\rho}$, ρ_{in}, f_0 are the unknown discrete particle, the extrapolate density, the sum of incoming discrete particles, and the static discrete particle, respectively. In this way, the density at the concave corner is approximated to a realistic value which produces quicker and better simulations(section 4.1 and section 4.2). Due to the extrapolation uses the density values of the nearest neighbours i.e. the first layer of the surrounding nodes, the parallel efficiency is not strongly impacted. The two incoming and outgoing discrete particles represented by the red lines in Figure 3.3 are assumed equal to enforce the no-slip boundary condition, thus, the incoming discrete particles are summed and are equal to the sum of the outgoing discrete particles to conserve the mass and momentum.

3.3.4 Multiphase flow treatments

Several models were created for multiphase flows in the LBM framework. All of those models use at least two distributions and can be written as

$$f_i^k(\vec{x} + \vec{e}_i\Delta x, t + \Delta t) = f_i^k(\vec{x}, t) + \Omega_i^{k3}\Big(\Omega_i^{k1}\Big(f_i^k(\vec{x}, t)\Big) + \Omega_i^{k2}\Big(f_i^k(\vec{x}, t)\Big)\Big), \tag{3.32}$$

where Ω_i^{k1} is the single-phase collision operator for the phase k described in the subsubsection 3.3.2.2, Ω_i^{k2} is the perturbation operator for the phase k which represents the interfacial forces between the two fluids, and Ω_i^{k3} is the separation operator for the phase k between the distributions. The last operator is only needed for few multiphase models.

A general description of the most used models will be presented and especially for the colour fluid model.

3.3.4.1 Colour fluid model

This model can be considered as a VOF model in the LBM Framework. Indeed, the main idea introduced by Rothman and Keller [1] for LGA is to simulate two immiscible liquids separately in the same domain and segregate them by a reconstruction operator. Gunstensen *et al* [4] extended it to LBM.

The method can be extended to more than two fluids [91] but we will limit here to two immiscible liquids. We also restrict our discussion to two fluids with the same density although it can be used for fluids with different densities [92]. We call the first fluid "Red" and the second fluid "Blue" and denote r and b, respectively. To simplify the notation, we denote k for either r or b.

The fundamental steps of the model

Similar to VOF, the colour gradient is used to estimate the normal of the interface and to evaluate the interface forces. However, the transport Equation 3.10 is implicit due to LBM is an interface-capturing. Indeed, all properties needed to be evaluated at each node are known thus, it is not necessary to calculate fluxes as in the Navier-Stokes solvers. This reduces the spurious currents, no false diffusion and flux errors, and enables lower Capillary numbers.

The Equation 3.32 can be seen for this model as:

- Single-phase collision

$$f_i^k(\vec{x},t)^* = f_i^k(\vec{x},t) + \Omega_i^{k1}\Big(f_i^k(\vec{x},t)\Big). \tag{3.33}$$

- Perturbation collision

$$f_i^k(\vec{x},t)^{**} = f_i^k(\vec{x},t)^* + \Omega_i^{k2}\Big(f_i^k(\vec{x},t)\Big). \tag{3.34}$$

- Recolouring

$$f_i^k(\vec{x},t)^{***} = f_i^k(\vec{x},t)^{**} + \Omega_i^{k3}\Big(f_i^k(\vec{x},t)\Big). \tag{3.35}$$

❀ Streaming

$$f_i^k(\vec{x} + \vec{e}_i \Delta x, t + \Delta t) = f_i^k(\vec{x}, t)^{***}. \tag{3.36}$$

Due to the two immiscible liquids being simulated separately, their densities[7] are evaluated with the zeroth moment as

$$\rho_k = \sum_i f_i^k \,. \tag{3.37}$$

.

The single-phase collision is resolved with the BGK approximation (section 3.3.2.2). The perturbation is introduced by Grunau *et al* [93], Reis *et al* [92] and Lishchuk *et al [2]*. The recolouring minimizes the Helmholtz free energy. However, this technique is numerically time-consuming and creates spurious current due to the lattice pinning. Latva-Kokko *et al* [5] proposed an approximation based on the work of Ortona *et al* [94] and of Tölke *et al* [95] to remove the lattice pinning, smooth the interface and low calculation cost:

$$\begin{aligned} \left(\Omega_i^R\right)^3 &= \frac{\rho^R}{\rho} f_i + \beta \frac{\rho^R \rho^B}{\rho} w_i \cos(\varphi_i) |\vec{e}_i|, \\ \left(\Omega_i^B\right)^3 &= \frac{\rho^B}{\rho} f_i - \beta \frac{\rho^R \rho^B}{\rho} w_i \cos(\varphi_i) |\vec{e}_i|, \end{aligned} \tag{3.38}$$

where $f_i = f_i^R + f_i^B$ and $\cos(\varphi_i)$ is the angle between the discrete velocity and the normal of the interface. It can be noticed the collision operator can be applied on f_i instead of f_i^R and f_i^B. We used the strategy of applying on f_i in this thesis.
In the streaming step, particles hop from node to node. The total population is $f_i = \sum_k f_i^k$ so the total density ρ is $\rho_r + \rho_b$. The evaluation of the velocity depends on the model for the interface forces (the perturbator operator $\Omega_i^{k\,2}$).

Grunau approach

Grunau *et al* [93] extended the work of Gunstensen *et al* [4] to different density and viscosity ratio and improved the perturbator operator. The colour gradient is the same

[7] ρ_k can be seen as a partial density.

as that defined by Gunstensen, i.e.

$$G = \sum_i \left[\left(\rho_r(\vec{x} + \vec{e}_i \Delta x, t) - \rho_b(\vec{x} + \vec{e}_i \Delta x, t) \right) e_i \right]. \tag{3.39}$$

The perturbation operator is based on the idea of Gunstensen to apply a force according to the angle between the normal of the interface and the lattice direction. The model works but it does not recover incompressible Navier-Stokes equations for the conservation of mass and momentum according to the Chapman-Enskog expansion technique. The operator derived from the moments for D2Q6 (hexagonal lattice) is defined as:

$$\Omega_i^{k\,2} = \frac{A^k}{2} |G| \left[\frac{(G \cdot e_i)^2}{|G|^2} - \frac{1}{2} \right]. \tag{3.40}$$

Reis *et al* [92] extended to D2Q9 as

$$\Omega_i^{k\,2} = \frac{A^k}{2} |G| \left[\frac{(G \cdot e_i)^2}{|G|^2} - \frac{3}{4} \right]. \tag{3.41}$$

A^k is a parameter controlling the surface tension and define [92] as:

$$\sigma^k = \frac{4}{9} A^k \tau c^2, \tag{3.42}$$

where σ^k is the contribution to the surface tension from the phase k and c is the lattice speed ($\Delta x / \Delta t$). From this perturbator approach, the calculus of the momentum moment is:

$$\rho_k u = \sum_i \left(f_i^k e_i \right). \tag{3.43}$$

Reis approach

Reis *et al* [92] proposed to modify slightly the approach of Grunau *et al* [93] to recover the Navier-Stokes equations by using the Chapman-Enskog expansion. Indeed, the authors have shown that the stress tensor from the Grunau *et al* approach does not have the correct form of the Navier-Stokes equations. They proposed to rewrite the

Equation 3.41 as:

$$\Omega_i^{k\,2} = \frac{A^k}{2}|G|\left[\omega_i \frac{(G\cdot e_i)^2}{|G|^2} - B_i\right], \tag{3.44}$$

where $B_0 = -\frac{4}{27}$, $B_i = \frac{2}{27}$ for $i = 1, 2, 3, 4$ and $B_i = \frac{5}{108}$ for $i = 5, 6, 7, 8$.

Lishchuk approach

Lishchuk *et al* [2] use the hydrodynamic approach to model the interface forces instead of using the simplify kinetic approach as from Grunau *et al* or Reis *et al*. The main advantage is to be able to use directly the equations for hydrodynamic approach, and thus, the Continuum Surface Force from Brackbill [3]. However, Lishchuk does not use the correct form to model the body force in the LBM Framework according to the Chapman-Enskog expansion.

The model was extended to use the body force modelled by Guo [96] and the Brackbill force [3].

$$\left(\Omega_i^k\right)^2\left(f_i^k(\vec{x},t)\right) = \Delta t\ \omega_i\left(1-\frac{1}{2\tau}\right)\left[\frac{(u\cdot e_i)}{c_s^4}e_i + \frac{(e_i-u)}{c_s^2}\right]\cdot F_s, \tag{3.45}$$

where F_s is the Continuum Surface Force [3]

$$F_s = -\sigma\kappa\frac{G}{[c]}, \tag{3.46}$$

where κ is the curvature, G is the colour gradient and $[c]$ is the jump in colour. The classical approach is to base the colour function on the normal density ρ^N ($\rho^N = \frac{\rho_r-\rho_b}{\rho_r+\rho_b}$) i.e. defined between -1 and 1. Thus, the variation of the normal density (jump in colour) is 2 and we obtain this equation:

$$F_s = -\frac{1}{2}\sigma\kappa\nabla\rho^N. \tag{3.47}$$

The curvature is approximated by the norm of the second derivative of the colour function but we use the derivative of the colour gradient to define it i.e. mathematically, the result is the same but numerically it can introduce a slight error. In subsubsection 3.3.5.1, the gradient calculation approximations are described. With this

perturbation operator, it is necessary to take the contribution in the first moment i.e.

$$\rho_k u = \sum_i \left(f_i^k e_i \right) + \frac{\Delta t}{2} F_s. \tag{3.48}$$

3.3.4.2 Shan & Chen model

This model can be considered as an extension of the Colour fluid model. Indeed, it starts with the same idea: each distribution represents one fluid. However, the idea to model the segregation of the two phases is strongly different. In the Shan & Chen model, the segregation is based on a repulsive force [97] which modifies the equilibrium velocity. In that case, it does not need to reconstruct the interface.

This model reduces the spurious current compared to the colour fluid model. However, it is difficult to determine the repulsive force of many fluids through macroscopic properties such as the surface tension. Moreover, the interface thickness and surface tension are linked which can lead to errors. In academic research, this model is the most used [98]. It is also used for boiling applications and reactive flows [99–101].

3.3.4.3 Free energy approach

This model is based on the Helmholtz free energy functional [102]. The Helmholtz free energy is based on the internal energy whereas the Gibbs free energy is based on the enthalpy. Clearly, the Gibbs approach is a better way of dealing with phase-change[8]. In this thesis, we consider only isothermal and low-speed flow thus, the brief description of the model is restricted to the Helmholtz free energy model with the Ginzburg–Landau free energy density functional [103]:

$$\Psi = \int \left(\psi \left(T, \rho \right) + \frac{\kappa}{2} \left(\nabla \rho \right)^2 \right) dV, \tag{3.49}$$

where Ψ, $\psi \left(T, \rho \right)$, and $\frac{\kappa}{2} \left(\nabla \rho \right)^2$ are the functional, the "bulk" free energy density from Landau mean field theory, and the gradient term, respectively. For this approximation to be valid small values of ρ are needed. From this functional, it is possible to obtain the chemical potential by taking the variational derivative and determine the ther-

[8] It can occur at non-equilibrium thermodynamics

modynamic pressure tensor with the Gibbs-Duhem relation. Using this macroscopic-microscopic approach, we can incorporate into the LBM Framework through the three first moments. This model creates a relative thick interface but it, almost, does not produce spurious currents. The surface tension can be controlled directly [104]. More details about the method can be found in the references [105–108].

3.3.5 Numerical techniques

After the description of the different multiphase models, the different numerical techniques used in this thesis will be described in detail.
Let to consider a variable φ and the gradient of this variable $\nabla\varphi$ on a Cartesian mesh for the rest of this subsection. The subscripts i and j refer to the directions x and y respectively in this subsection.

3.3.5.1 Gradients

Accurate approximation of gradients plays an important role in the colour-fluid model [109]. For a Cartesian grid saving in an unstructured manner i.e. the nodes are not ordered and the connectivity is saved, we limit the gradient choices to: finite difference (first order (decentred/biased) and second order (centred)) and fourth order compact scheme.

Finite difference

At the boundary conditions (wall, inlet, outlet, etc.), the first order decentred gradient in the normal direction of the boundary and the second order centred gradient in the other direction is used based on Taylor's theorem. For a node with a boundary in the +y-direction, the gradient is set as:

$$\nabla\varphi \approx \begin{cases} \frac{\varphi_{i+1,j}-\varphi_{i-1,j}}{2\Delta x}, \\ \frac{\varphi_{i,j+1}-\varphi_{i,j}}{\Delta x}. \end{cases} \tag{3.50}$$

For a convex corner or in the domain, the second order centred is given as:

$$\nabla\varphi \approx \begin{cases} \frac{\varphi_{i+1,j}-\varphi_{i-1,j}}{2\Delta x}, \\ \frac{\varphi_{i,j+1}-\varphi_{i,j-1}}{2\Delta x}. \end{cases} \tag{3.51}$$

For a concave corner oriented in the +x-direction and the +y-direction, the first order decentred in both directions is used as:

$$\nabla\varphi \approx \begin{cases} \frac{\varphi_{i+1,j}-\varphi_{i,j}}{\Delta x}, \\ \frac{\varphi_{i,j+1}-\varphi_{i,j}}{\Delta x}. \end{cases} \tag{3.52}$$

This method is anisotropic which removes the isotropic properties of physical phenomena such as the colour gradient [109].

The fourth order compact scheme

This scheme is classically used for calculating the colour gradient. It is fourth and second order in space for Cartesian and polar coordinates, respectively. In polar coordinates, the gradient is also called isotropic gradient due to its isotropic conservation properties. Using the weight function of LBM and for the D2Q9 scheme, the gradient is calculated as:

$$\nabla\varphi \approx 3\sum_{l} \omega_l e_l \varphi\left(x + \Delta x\, e_l\right). \tag{3.53}$$

Other higher-order schemes[9] can be used, and you can find more details in [109,112,113]. Obviously, this scheme cannot be used directly at the boundaries. To tackle this problem, two ways are proposed using the decentred finite difference or using an extrapolation scheme. The decentred technique has no problem to be applied at the boundary. However, the two different schemes between inside the domain and on the boundary, change the representation of the colour gradient so the interface by the lack of isotropy conservation with the decentred finite difference. In order to avoid two different schemes, an extrapolation technique is used to define the variable φ at the nodes

[9]High-order schemes are built by using a linear operator between Taylor series and are explicits. Compact schemes are the implicit version and, thus, a system of equations is needed to be solved [110, 111].

outside of the boundary [10]. Those nodes are ghost or solid nodes and thus, the fourth-order scheme can be applied on the boundary. However, it cannot be considered as fourth-order accuracy in this case due to the technique used for extrapolating affects the order of accuracy for the gradient.

Therefore, the interest is not the accuracy but keeping the same scheme helps to smooth the difference of accuracy at the boundary thus, the interface becomes smoother.

3.3.5.2 Extrapolations

In classical LBM schemes, extrapolations are not needed. However, to improve the results, to reduce non-physical behaviour or simply not impose a boundary condition, two kinds of extrapolation are used: one based on finite difference gradients described in the previous subsection, and the other one based on the inverse distance weighting interpolation.

Each extrapolation is defined to extrapolate at the boundary (wall, concave corner, convex corner, pressure, velocity, etc.) or at the first layer of solid under the wall (wall, concave corner or convex corner). To simplify, the first layer of solid under the wall is called "in solid" for this subsection.

Finite difference

As for the gradients, the finite difference is based on Taylor's theorem to approximate a gradient. For extrapolation, the gradient is set to be zero to consider no flux. The extrapolation at the boundaries uses only the first order discretisation and in the solid, the second order discretisation. The first order can be considered as not accurate however, the value cannot be non-physical, and it is used only to impose no flux at a boundary for instance the pressure. The second order is rarely used in this research due to its anisotropic properties. For a wall or a boundary node type oriented in the +y-direction, the extrapolation at the boundary is:

$$\varphi_{i,j} \approx \varphi_{i,j+1}, \tag{3.54}$$

[10] It can be outside of the domain too.

and in the solid:

$$\varphi_{i,j-1} \approx 2\varphi_{i,j} - \varphi_{i,j+1}. \tag{3.55}$$

For a convex or concave corner oriented in +x-direction and +y-direction, the extrapolation at the boundary is:

$$\varphi_{i,j} \approx \varphi_{i+1,j+1}, \tag{3.56}$$

and in the solid:

$$\varphi_{i-1,j-1} \approx 2\varphi_{i,j} - \varphi_{i+1,j+1}. \tag{3.57}$$

Inverse distance weighting

This method is based on the weight by the inverse of the distance. Considering n nodes, the extrapolation is:

$$\varphi_{ij} \approx \frac{\sum_k^n \omega_k \varphi_k}{\sum_k^n \omega_k}, \tag{3.58}$$

where

$$\omega_k = \frac{1}{\sqrt{\left(x\left(\varphi_k\right) - x\left(\varphi_{ij}\right)\right)^2 + \left(y\left(\varphi_k\right) - y\left(\varphi_{ij}\right)\right)^2}}. \tag{3.59}$$

For a wall node type oriented in the +y-direction, the extrapolation on the boundary is:

$$\varphi_{i,j} \approx \frac{1}{1 + \frac{2}{\sqrt{2}}} \left(\varphi_{i,j+1} + \frac{1}{\sqrt{2}} \left(\varphi_{i-1,j+1} + \varphi_{i+1,j+1} \right) \right), \tag{3.60}$$

and in the solid:

$$\varphi_{i,j-1} \approx \frac{1}{1 + \frac{2}{\sqrt{2}}} \left(\varphi_{i,j} + \frac{1}{\sqrt{2}} \left(\varphi_{i-1,j} + \varphi_{i+1,j} \right) \right). \tag{3.61}$$

For a convex corner oriented in the +x-direction and the +y-direction, the extrapolation on the boundary is:

$$\varphi_{i,j} \approx \frac{1}{4 + \frac{3}{\sqrt{2}}} \left(\varphi_{i-1,j} + \varphi_{i+1,j} + \varphi_{i,j-1} + \varphi_{i,j+1} + \frac{1}{\sqrt{2}} \left(\varphi_{i-1,j-1} + \varphi_{i-1,j+1} + \varphi_{i+1,j+1} \right) \right), \tag{3.62}$$

and in the solid:

$$\varphi_{i-1,j-1} \approx \frac{1}{2+\frac{1}{\sqrt{2}}}\left(\frac{1}{\sqrt{2}}\varphi_{i,j} + \left(\varphi_{i-1,j} + \varphi_{i,j-1}\right)\right). \tag{3.63}$$

For a concave corner oriented in the +x-direction and the +y-direction, the extrapolation on the boundary is:

$$\varphi_{i,j} \approx \frac{1}{2+\frac{1}{\sqrt{2}}}\left(\frac{1}{\sqrt{2}}\varphi_{i+1,j+1} + \left(\varphi_{i+1,j} + \varphi_{i,j+1}\right)\right), \tag{3.64}$$

and in the solid:

$$\begin{aligned}
\varphi_{i-1,j} &\approx \frac{1}{1+\frac{1}{\sqrt{2}}}\left(\frac{1}{\sqrt{2}}\varphi_{i,j+1} + \varphi_{i,j}\right), \\
\varphi_{i,j-1} &\approx \frac{1}{1+\frac{1}{\sqrt{2}}}\left(\frac{1}{\sqrt{2}}\varphi_{i+1,j} + \varphi_{i,j}\right), \\
\varphi_{i-1,j-1} &\approx \frac{1}{1+\sqrt{\frac{2}{5}}}\left(\varphi_{i,j} + \sqrt{\frac{2}{5}}\left(\varphi_{i+1,j} + \varphi_{i,j+1}\right)\right).
\end{aligned} \tag{3.65}$$

3.3.5.3 Interpolations

The interpolation is used to estimate the contact angle. Therefore, it is defined only on surfaces i.e. walls and concave and convex corners. The interpolation uses the solid and fluid nodes surrounding the node which needs to be interpolated. Only two kinds of interpolations were implemented: the linear interpolation and the linear least-square interpolation.

Linear interpolation

This interpolation is the average between the node connected to the normal direction and the node connected to the opposite direction.

Linear Least-Square interpolation

This interpolation is statistical. Let's define two variables x and y, and we are seeking a line of regression with the form $y = a\,x + b$.

By using the least-square method and for n nodes, the coefficient a is:

$$a = \frac{n\sum xy - \sum x \sum y}{n\sum x^2 - \left(\sum x\right)^2}, \tag{3.66}$$

and b is:

$$b = \frac{\sum y \sum x^2 - \sum x \sum xy}{n\sum x^2 - \left(\sum x\right)^2}. \tag{3.67}$$

Using on a surface, x can be defined as a signed distance (positive for the fluid nodes and negative for the solid nodes). Therefore, the method is restricted to seek b due to the distance is null at the boundary. All the loops are vectorised, and the nodes are marked in the pre-processing part. Thus, the calculation time is similar to the linear interpolation.

3.3.6 Limits of the LBGK and colour-fluid models

The BGK is a linear or quasi-linear operator and assumes the relaxation rate is the same for all the moments. Consequently, the minimum value of the relaxation time to keep the solution stable is limited. The maximum value of the relaxation time is not limited by the method. However, a high relaxation time (above 1.5) means a rarefied flow due to the low collision rate. Therefore, the relaxation time should be between 0.6 and 1.5. In case of a low relaxation time needed, the Central Moment (CM) operator should be more appropriate and also the grid resolution can be reduced.

The LBM as it is commonly used is an explicit time scheme. In two phase and low-speed flow, the number of time step can be huge for a flow in a big domain as in porous media. An implicit method should be used for an industrial case. To design it, it is necessary to use transport equations with an iterative solver. Probably, using the CM operator, it could be easier to establish a fully implicit scheme [74] due to its intrinsic formulation and stability.

The colour-fluid model has several limitations. The model, until now, needs to have a recolouring operator which is computationally expensive, creates spurious currents, and Galilean invariance. The second problem is that the surface tension can be anisotropic due to the colour gradient. At low capillary number or high surface tension, the model

generates a lot of spurious currents, but it is better than the traditional VOF models in term of Capillary number i.e. colour-fluid model can simulate until around 10^{-5} [114] whereas VOF limits around 10^{-3}.

3.4 Validation of the colour fluid model: droplet deformation

A quick 2D validation was done on droplet deformation under a simple shear at low Reynolds number. The flow conditions for both fluids are: $\mathrm{Re} \ll 1$ and $\mathrm{Kn} < 0.001$. This imposes a creeping flow for both fluids in the hydrodynamic flow regime. The calculation stops when the error of the velocity in the Y-direction over the domain is less than 10^{-7}.

As an initiated validation, the results will be compared to an analytical solution from Shapira and Haber (SH) based on the Stokes flow around the droplet with a reflection method [115], the OpenFOAM VOF results from P. Capobianchi, other VOF results [116], and the results obtained for the free energy [106] and phase-field approaches [116] LBM. Comparing with experimental works has no sense due to 2D simulations.

The confinement (Diameter divided by the "channel" height) is set to 0.5 and the viscosity ratio to 1. The empirical parameter of the SH model is set to 5.6996. The radius of the droplet is set to 20$[lu]$ as used in the previous validations [117], the length of the domain is 16 times of the radius (320$[lu]$) and the viscosity is 0.08$[lu]$. The shear flow is imposed with Zou and He boundary condition [83] and a periodic boundary is set in the length of the domain. We used the CSF approach for the validation as in [117] and the results are plotted in Figure 3.4 and they are in good agreement. We have also evaluated the approach of Reis *et al* [92] and we did not find significant differences.

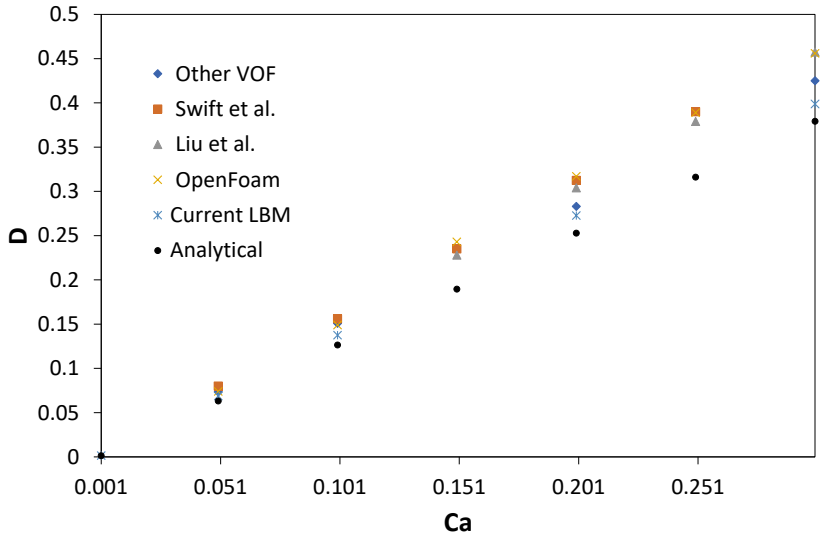

Figure 3.4: Droplet deformation with a confinement of 0.5 and a viscosity ratio of 1.

3.5 Chapter summary

We have seen it is not an easy task to select the right method for simulating flows, especially in case of two phases flows. NS approach can be seen as the classical one and the equations can be solved by different numerical methods and different models.
The SEM is suitable to get accurate results or uses the strength of supercomputer resources, but it can be easily unstable and the calculation costs can be high. The FVM is commonly used for NS equations and performs very well in case of complex systems but the accuracy or the parallel efficiency can be low.
For multiphase flow, the VOF model is a strict conservation of mass but it is costly due to the interface reconstruction and generating of spurious currents. The Level-Set model removes the reconstruction step and reduces spurious currents, but it is not mass conservative. The Marker-based model represents the interface accurately, but it is not mass conservative and can be very costly.

The LBM has been described with the collision operators and equilibrium distributions commonly used by the community. More details were given for the BGK approximation used in this work which is the cheapest, simplest, and the most used collision operator. However, a more recent collision operator, Central Moment (CM),

sounds promising in term of accuracy, stability, and relatively cheap.
To recover NS equations from Boltzmann equation, two approaches are commonly used: Hilbert and Enskog but they are only a formal proof and not a rigorous demonstration. This subject is still an open problem in the mathematics community.
Several classical boundary conditions have been discussed, especially the non-traditional way to implement the periodic boundary condition. As the platform has been developed for the massively parallel approach, the periodic boundary has been treated through the domain decomposition which leads to being more efficient.
The choice of the multiphase models and the numerical approximations affects the accuracy and limits the physics. Thus, the colour fluid model with the fourth order compact scheme is the most relevant choice to simulate multiphase flows in porous media. However, the recolouring operator generates spurious current at a low capillary number.
The classical scheme used for LBGK employed here is an explicit march in time. Therefore, the time step is limited, and the calculation can be very costly.

Finally, a validation case is shown on the droplet deformation. We got a good agreement with the analytical. This case is a complicated case, compared usual validation test case such as Laplace's law, due to it is dynamic and the deformation comes from the shear stress.

Chapter 4

Analysis of numerical methods

The new platform created from scratch has to be validated, the performance evaluated, the new techniques analysed, and the effects of the different models described in subsubsection 3.3.4.1 compared. For the single-phase analysis, two test cases were chosen: the lid-driven cavity and Poiseuille flows. The lid-driven cavity is chosen due to it has corners, stationary walls, and a velocity (or moving wall) boundary conditions and the flow is not driven by a pressure difference. The Poiseuille flow is applied in a straight channel and inclined channels. For the two-phase flows, the Laplace's law was chosen to evaluate the models in colour fluid model (subsubsection 3.3.4.1).

4.1 The lid-driven cavity flow

4.1.1 Description

As the thesis is focused on 2D two-phase flows for porous media, this implies that the simulation for the single-phase flows will be validated for a 2D case. However, the flow cannot be easily compared with experimental results due to the 3D vortexes found in experiments. Thus, this case is a pure numerical validation.

In order to validate the results, they are compared with the literature [118,119] and two NS approaches. The numerical methods used, and described in section 3.2, to compare are: Finite Volume Method (FVM) with Code Saturne [120] and Spectral Element Method (SEM) with Nek5000 [121]. The two methods should give the same result but Code Saturne is a low-order spatial discretization solver and Nek5000 is a high-order weighted residual solver. Spectral methods are considered as the reference for numerical methods. However, Code Saturne is used in industrial contexts and Nek5000 is mostly used in academic research due to the computational cost and the not friendly user interface.

The boundary conditions, taken in the LBM simulations, are bounce-back for the walls (left, right, and bottom side), Zou and He [83] for the Dirichlet velocity condition (top side), Ho for the Velocity-Wall corners at the top side [84] , and bounce-back with extrapolation for the two wall corners at the bottom side.

4.1.2 Effect of the Reynolds number

From Re=100 to Re=1000, only 3 vortices exist: one in the middle of the cavity and two at the corners in the bottom of the cavity. From Re=1000 to Re=5000, another vortex is generated at the top left corner. After Re=5000, the flow becomes unsteady and vortexes travel along the walls. However, the transition between steady and unsteady does not agree between numerical methods.In order to compare easily with the literature, the study is limited from Re=100 to Re=3200 (steady).
The grid resolutions for the simulations are summarized in Table 4.1. The P_n/P_{n-2} formulation, the Helmholtz solver convergence criterion of 10^{-12}, and the divergence criterion of 10^{-11} were used for the SEM simulations.

Re	LBM	FV	SEM
100	100x100	50x50	10x10 and P=7
400	200x200	50x50	10x10 and P=7
1000	400x400	100x100	10x10 and P=7
3200	1000x1000	200x200	10x10 and P=12

Table 4.1: Grid resolutions and the polynomial order (SEM) for the lid-driven cavity simulations.

4.1.2.1 Flow field

For a qualitative analysis, the flow field will be analysed by comparing the streamline of FVM and LBM results.

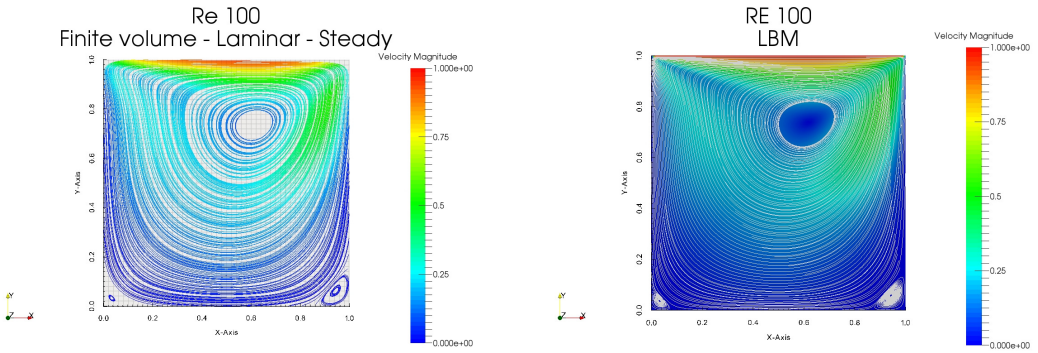

Figure 4.1: The lid-driven cavity's streamlines at Re=100 for FVM and LBM at the left and right, respectively.

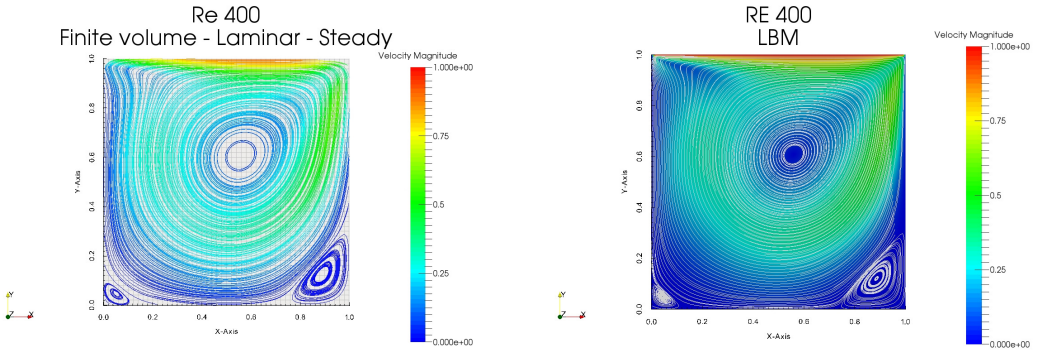

Figure 4.2: The lid-driven cavity's streamlines at Re=400 for FVM and LBM at the left and right, respectively.

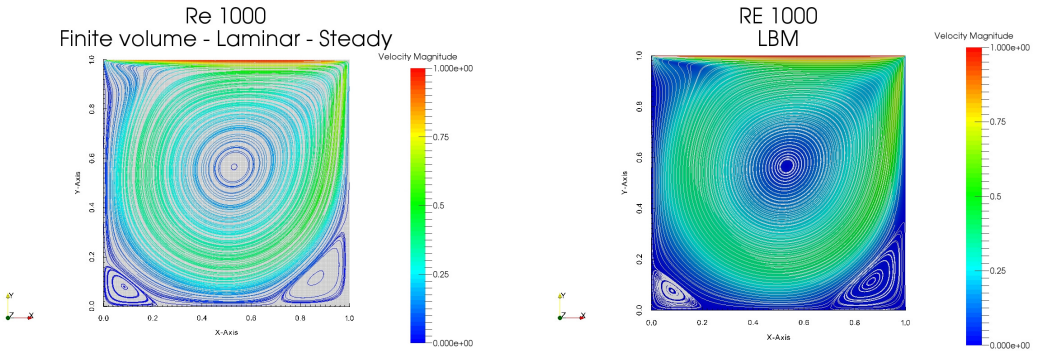

Figure 4.3: The lid-driven cavity's streamlines at Re=1000 for FVM and LBM at the left and right, respectively.

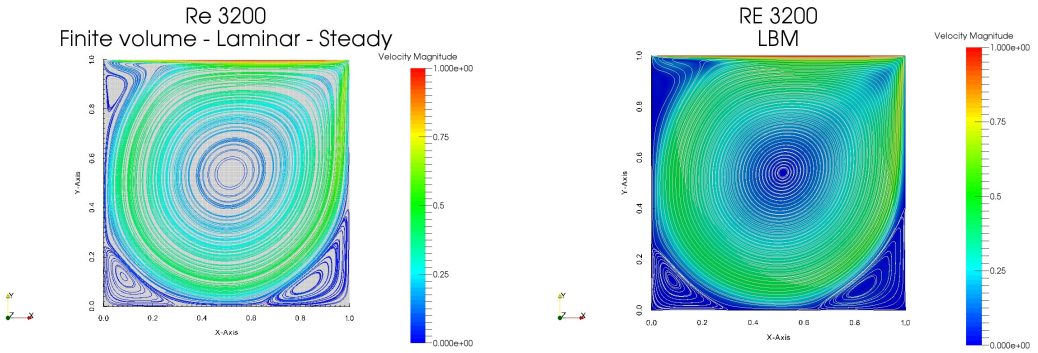

Figure 4.4: The lid-driven cavity's streamlines at Re=3200 for FVM and LBM at the left and right, respectively.

A small difference exists between the two methods, but we consider the results equivalent.

4.1.2.2 Profiles

Analysis of velocity profiles on the X and Y central lines are more precise and permit a quantitative analysis.

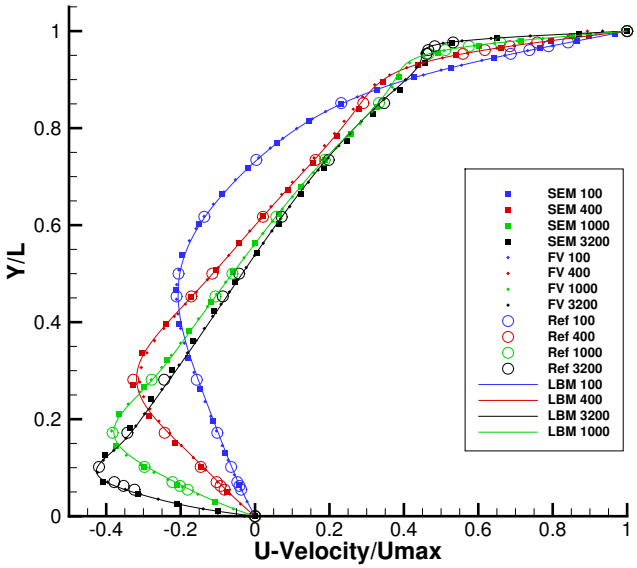

Figure 4.5: Comparison of the u-velocity along the central vertical line.

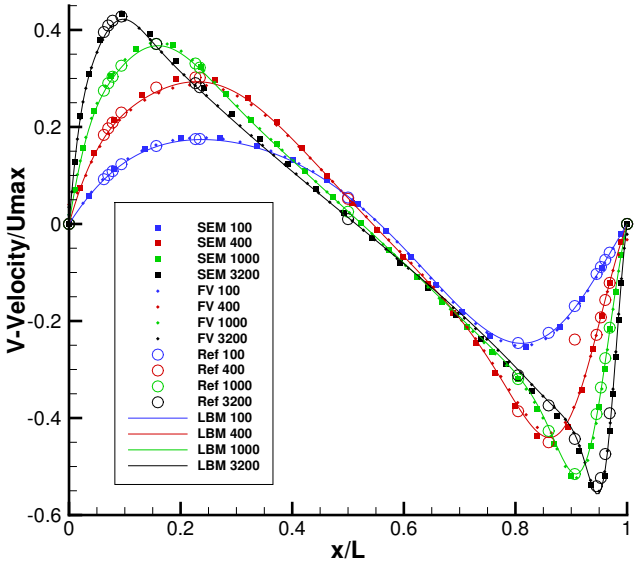

Figure 4.6: Comparison of the v-velocity along the central horizontal line.

All methods have a good agreement between them, thus the single-phase flow solver is validated. However, there is still some small differences due to the difference of the methods. The SEM enforces the continuity of the solution until the second derivative whereas FVM is only the first derivative. Thus, the grid resolution for FVM needs a fine mesh and is still less accurate for the high velocity gradients. The LBM has no continuity for the velocity derivatives, thus, for continuum flows at moderate Reynolds

number, the grid resolution needs to be higher than FVM. Consequently, the errors increase at high velocity gradients. However, all methods tend to the same solution when the cell/element/lattice size tends to 0.

4.1.3 Speed-up

An efficient code is essential to be able to produce quick results for large and complex domain appeared in porous media. To allow running large jobs, we need to ensure the efficiency of the code and the lid-driven cavity at Re=10,000 has been chosen for the domain size needed (1924x1924) and for the complex flow involving (unsteady). In order to compare the implementation of the method, we do not generate output during the simulation due to the writing is fully parallel and the time for writing is very high for few processors. The scaling obtained is:

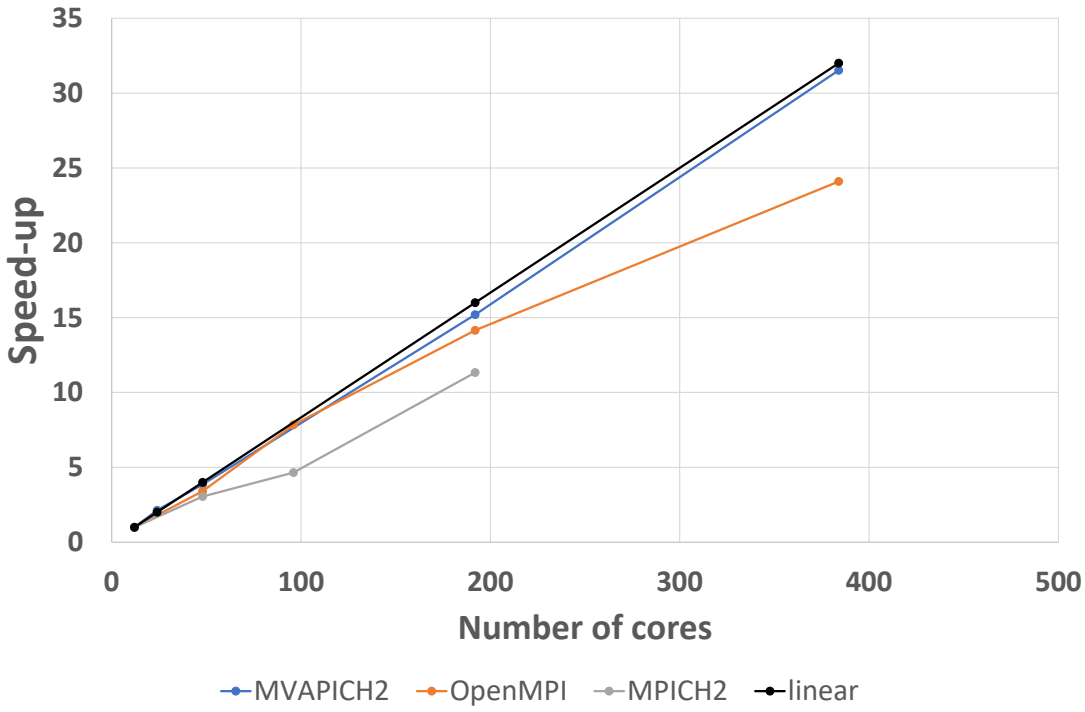

Figure 4.7: Speed-up at RE 10,000 with a mesh 1924x1924 up to 400 cores.

Figure 4.7 shows a very good scalability, especially with the MVAPICH2-2.1 library (optimised library for InfiniBand networks) is used. However, beyond 400 cores, the scaling is not enough, and it is shown in Figure 4.8 and in Table 4.2. Surprisingly, the

MVAPICH2-2.1 library is based on the MPICH2-3.1.4 library and the MPICH2-3.1.4 library gives a low performance. This is probably due to the packing and unpacking data for the network. Indeed, MPICH2 library has to convert the packing data to the InfiniBand network configuration whereas the MVAPICH2 does not need due to it is tuned for it. The OpenMPI-1.6 performed better but the tuning of the library is unknown (Default MPI library installed on the HPC).

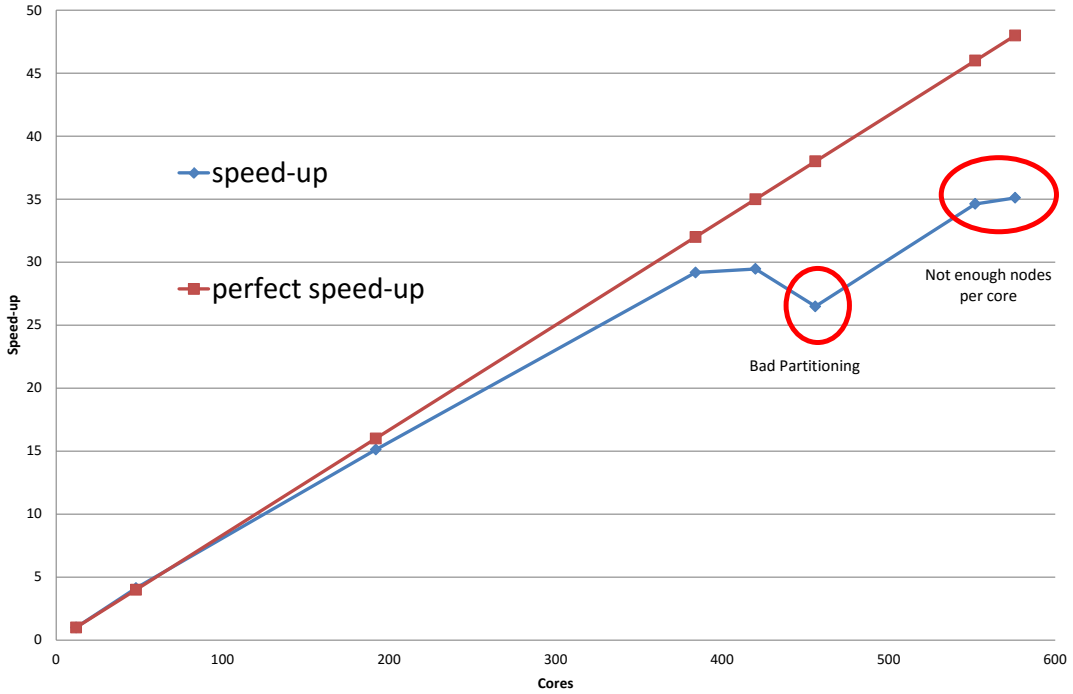

Figure 4.8: Speed-up at RE 10,000 with a mesh 1924x1924 up to 600 cores.

As seen in Figure 4.8, the partitioning is not optimum for the code. Indeed, the unstructured data storage, used for removing the solid in porous media, generates packing and unpacking data before and after exchanging data, respectively. This creates an unbalance of communication between the MPI processes. Moreover, the MPI blocking communication limits the efficiency. This strategy was adopted to guarantee the data was sent before using it. The implementation used dynamic classes in C++ and can lead to losing the state of communicators. No more development works were done to secure the unblocking communication due to the best way is to use the Remote Memory Access i.e. push and pull data without checking the state. The implementation is tricky, and the research topic is not getting the best performance but understanding

the flow in porous media.

The limitation of nodes per core (around 10,000 nodes per core) is quite high for an LBM code i.e. the open-source Palabos is around 2,500 nodes per core. However, Palabos is a Cartesian implementation per block (no solid removed in a block). In the current LBM implementation, the indexes solid nodes are removed from the computational domain. By the lack of time, the solid nodes are still present. This improves the efficiency for porous media but reduces for rectangular computational domain as this lid-driven cavity case.

Simulation time in s				
Cores	Mean	Speed-up	Efficiency	**Number of node per processor**
12	157873,32	1,0	100,0	308481
48	38253,06	4,1	103,2	77120
192	10440,53	15,1	94,5	19280
384	5411,21	29,2	91,2	9640
420	5358,52	29,5	84,2	8814
456	5960,36	26,5	69,7	8118
552	4559,08	34,6	75,3	6706
576	4497,3	35,1	73,1	6427

Table 4.2: Performance of the platform for the lid-driven cavity at Re=10,000.

As seen in the Table 4.2, the efficiency is very good at 576 cores compared to NS solvers where generally the efficiency is less than 50% for 10,000 cells per processors [122, 123].

4.2 An improved boundary condition at a low grid resolution and Reynolds number

Optimisation of existing system and designing new generation of products with compactness in mind, it is a challenge. Achieving this kind of compactness is mostly carried out by utilising porous media such as membranes, foams, etc. Therefore, the needs of simulation for complex geometries have increased drastically. At the same time, the accuracy of simulation has increased, thus, the simulations became more predictive. Different methods have been developed for Computational Fluid Dynamics such as

Lattice Boltzmann Method (LBM) which is a mesoscopic particle-based method derived from Boltzmann equation and Lattice Gas Automata (LGA) [56]. The collision between particles can be approximated by different operators such as Bhatnagar-Gross-Krook (BGK) [66], the Multiple Relaxation Time (MRT) [67, 68], the Central Moment (CM) [72, 74], the entropic [70, 71], etc.

A large branch of wall boundary conditions has been developed. The full-way bounce-back rule is the simplest rule, in which, each particle that hits the wall bounces in the opposite direction instantaneously without being affected by a collision process. This rule ensures the conservation of mass and the no-slip condition at the boundary. Removing the collision operator at the wall nodes reduces drastically the accuracy which results in great demand of finer mesh. An extension has been done by considering the wall is located between two lattice nodes. Using the approximation of Chapman-Enskog expansion, the full-way and half-way are first and second order, respectively [124].
The half-way bounce back rule can lead to a slip velocity at the wall. To tackle this problem, several wall boundary conditions were proposed such as Inamuro *et al* in 1995 [125] which constructs a reflective and diffuse boundary by using the local equilibrium function, Chen *et al* in 2007 [126] proposed to interpolate the equilibrium distribution, Latt in 2007 [86, 127] built a scheme based on the regularised LBM, Ginzburg [124], Ladd [85], and Bouzidi [128] proposed to interpolate schemes.

Choosing LBM to treat porous media leads the walls to be not aligned with the lattice. This generates "stairs" with a Cartesian grid and results in the generation of corners. Using a classical scheme for the Lattice Boltzmann Method, the density at a concave corner node is not correctly calculated due to the distribution being not completely defined i.e. the discrete velocities perpendicular to the normal of the corner are free. In other words, some mass is missed in the density calculation. Thus, it leads to having sensible different densities with the neighbour nodes at the same time step. We proposed to extrapolate the density in a suitable manner as explained in subsubsection 3.3.3.5, to improve the accuracy and conserve the momentum for flows at low Reynolds number.

4.2.1 Simulation conditions

We define the boundary conditions treated with the standard full-way bounce-back as "No Collision". The new approach with the collision operator and the extrapolation of the density from the neighbour nodes by the inverse distance weighting approach is called the "New Technique", whereas, without extrapolation the "No Extrapolation". Therefore, for walls aligned with the lattice, the "New Technique" and "No Extrapolation" are the same and are called "With Collision". We also compared to the standard half-way bounce-back and named "Half-Way". To analyse the new treatment, we use a Poiseuille-like flow in straight and inclined channels. The inclined cases are compared to Spectral Element Method (SEM) with Nek5000 [121]. Four elements with the polynomial order of 7 in the cross-section of the channels, the P_n/P_{n-2} formulation, the Helmholtz solver convergence criterion of 10^{-12}, and the divergence criterion of 10^{-11} were used for the SEM simulations. The mesh for the SEM simulations cannot be the same as LBM. In order to have the simulations as close as possible, we keep the same volume of fluid and the straight walls are aligned, thus the walls for the stairs are located in the middle as shown in Figure 4.9. The viscosity in LBM simulations is set to 0.1 [lu]. The pressure-drop is calculated by the difference of pressure between the centre of the channels at the inlet and the outlet-imposed pressure. We run the simulations for inclined channels with two grid resolutions and compared to the straight channels. In case of high grid resolution, the height of the channel is $192[lu]$ and in case of low resolution, the height of the channel is $19[lu]$.

The Reynolds number is defined as

$$Re = \frac{U^{max} H}{\nu}, \tag{4.1}$$

where, U^{max} is the maximum velocity in the channel, H the height of the channel and ν the kinematic viscosity.

In Figure 4.10, the velocity field is represented for two conditions of convergence: one based on the density and one on the X component of the velocity. Both criteria lead

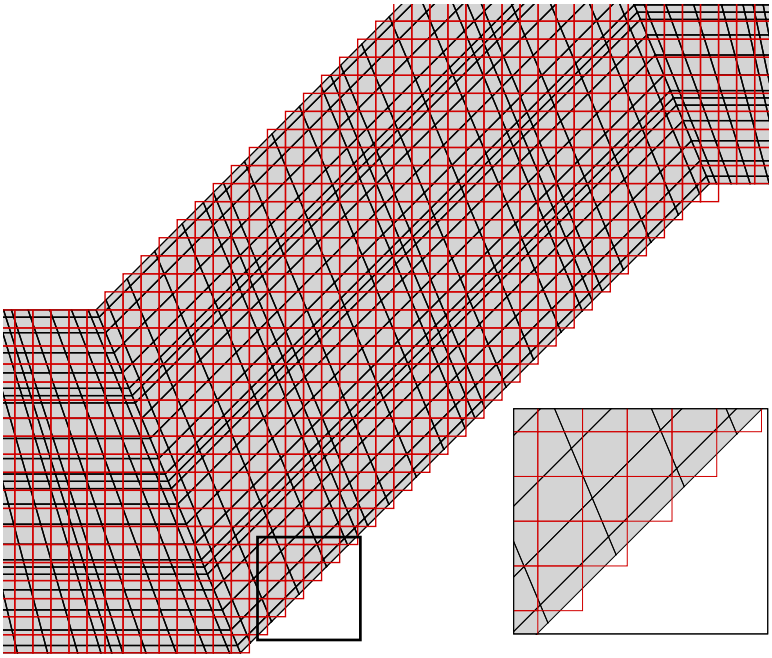

Figure 4.9: Comparison of the LBM (Cartesian) and SEM meshes in red and black, respectively.

to essentially the same results. In the following, the calculations will be terminated when the evolution of density is lower than 10^{-13} or 10^{-15} over the domain for low and high grid resolution, respectively. Indeed, the convergence criterion needs to be smaller for high grid resolution due to the velocity magnitude becomes extremely small, thus, the pressure-drop too which is the important result of this study. Those criteria were chosen after a sensitivity study.

4.2.2 Straight channels

4.2.2.1 Validation

The straight channels validate our code for a well-known flow with an analytical solution which is

$$\Delta P = \frac{8Re\nu^2}{H^3}L, \tag{4.2}$$

where, H and L are the height and length of the channel, respectively. This length is equal to two times the height of the channel.

A parabolic velocity profile is imposed at the inlet on the left side of the channel and

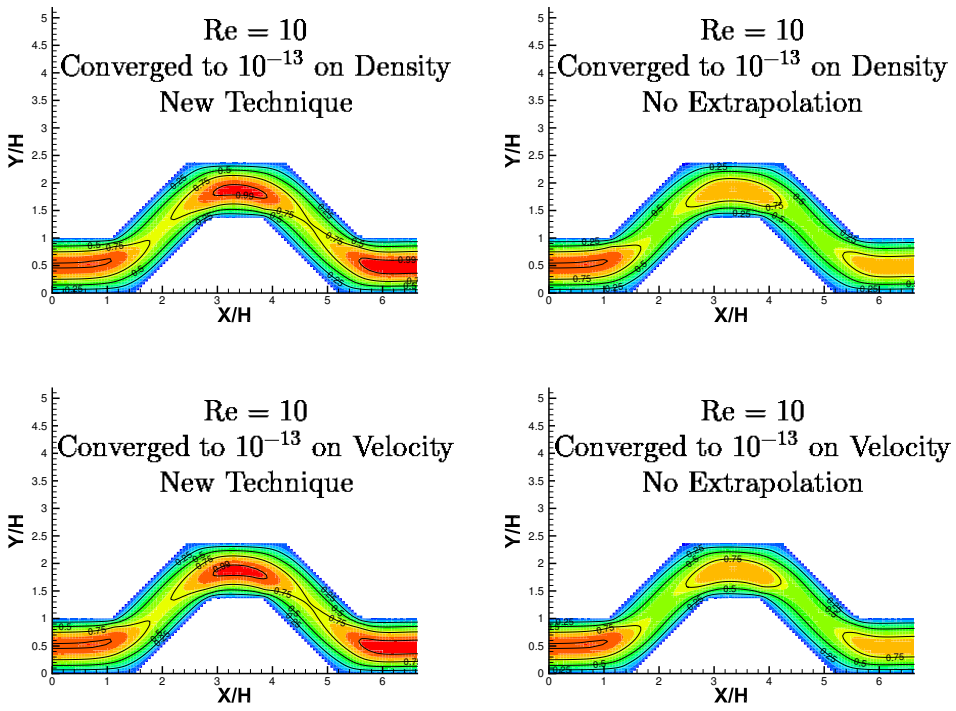

Figure 4.10: Comparison of the x-velocity field for Re=10 and low grid resolution

a constant pressure set to 1/3 [lu] on the right side of the channel with Zou and He boundary condition [83].

Pressure-drop analysis Table 4.3 shows the collision on the wall is needed to get a more accurate pressure-drop. The error is calculated with the analytical solution as a reference and normalised with the analytical solution. In Table 4.3, it can be noticed

Straight channels

	Re	With Collision	No Collision	Half-Way
Low Resolution	10	1.47%	18.75%	2.19%
	1	0.28%	14.43%	0.33%
	0.1	0.39%	14.06%	0.20%
	0.01	0.41%	14.02%	0.19%
High Resolution	10	0.014%	1.507%	0.021%
	1	0.003%	1.285%	0.003%
	0.1	0.004%	1.249%	0.002%
	0.01	0.007%	1.247%	0.004%

Table 4.3: Pressure-drop errors for a Poiseuille flow in the straight channels

the grid size is not enough for the low-resolution geometry to have an error less than

1% for Re=10. Compared to the classical "No Collision" technique, the results of using the collision operator on the walls (the "With Collision") are in good agreement with the analytical solution and similar to the "Half-Way" results.

Velocity profile analysis We have extracted the velocity profiles at the outlet which are shown in Figure 4.11. The Reynolds number has not strongly modified the velocity profiles for the creeping flow regime. It can also be noticed that the incorrect wall shear rate for the "No Collision" and thus, an overshoot of momentum is observed.

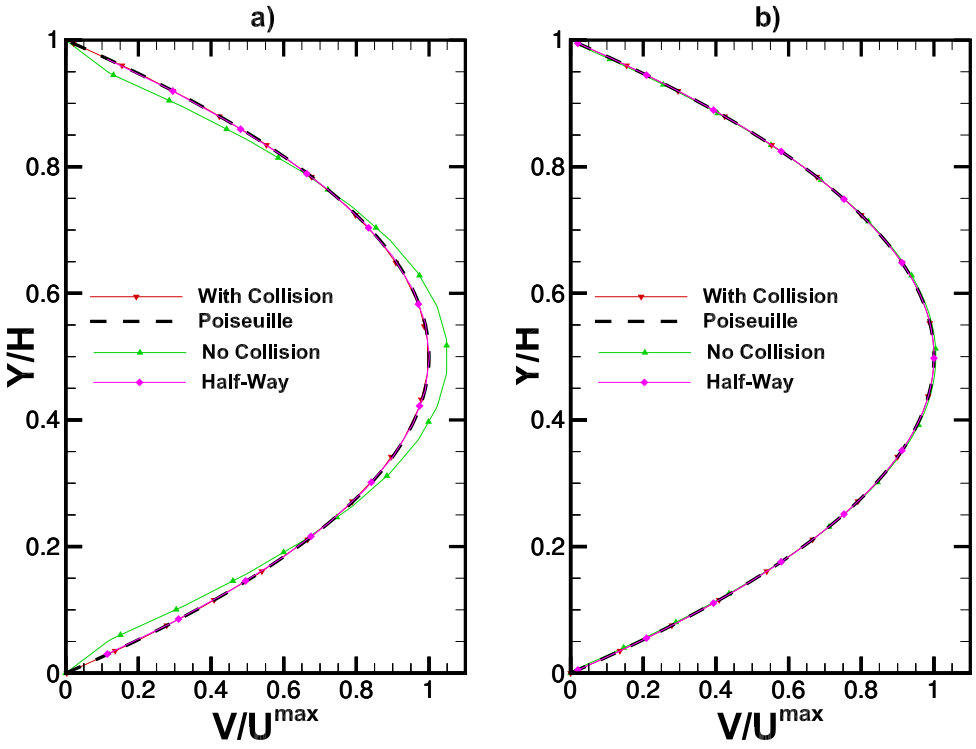

Figure 4.11: Velocity profiles at the outlet: a) low grid resolution and Re = 0.01 and b) high grid resolution and Re = 1.

4.2.2.2 Convergence study

The simulations were carried out for the channel height from 4 to 256[lu], for "No Collision", "With Collision", and "Half-Way" wall boundary conditions, and for Reynolds numbers of 0.01, 0.1, 1, and 10. However, the results for Re= 0.1 or 1 are similar to 0.01, thus, the results for Re=0.1 and 1 are not shown.

Study of the errors versus channel height

Pressure-drop errors Figure 4.12 shows "No Collision" converges to the same error for Re=0.01 or 10 whereas "With Collision" or "Half-Way" gives more accurate results for lower Reynolds number. Moreover, "Half-Way" gives more accurate results than "With Collision" when the Reynolds number is lower.

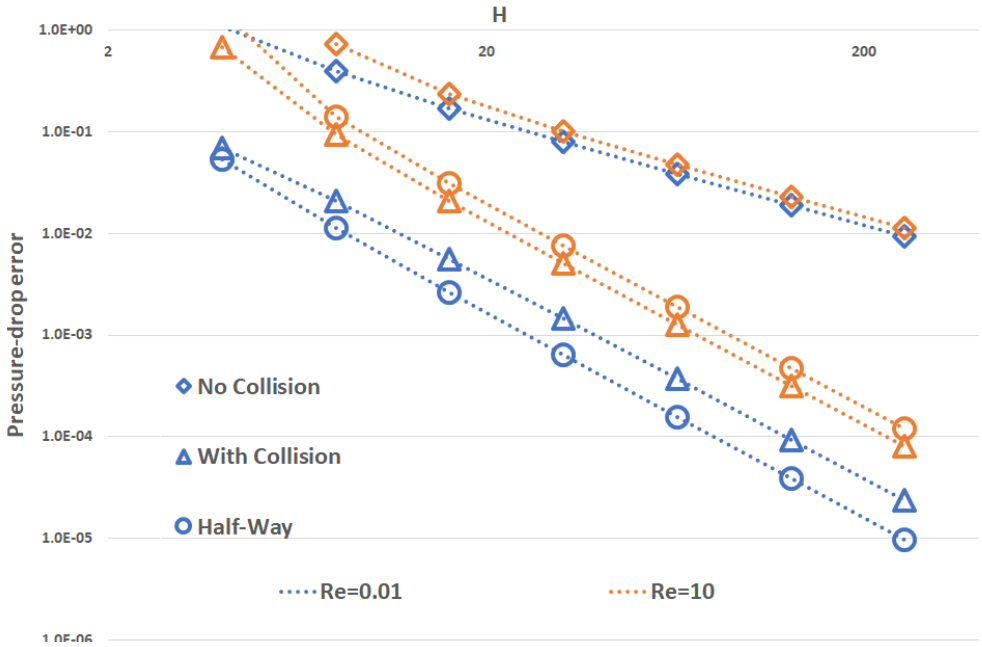

Figure 4.12: The pressure-drop error versus channel height.

Velocity errors We have performed the calculus of the relative error $\|E\|_1$ of the velocity as

$$\|E\|_1 = \frac{\sum^N |U_c - U_a|}{\sum^N |U_a|}, \tag{4.3}$$

where, N is the number of points in the domain, U_c and U_a are the velocity along the channel calculated from the LBM results and the analytical solution, respectively.
The Poiseuille-like flow can be imposed in a number of ways. In the current study, it is imposed by a constant force in the domain [75] (CF) i.e. $F_i = 3\omega_i e_i \cdot (\partial P/\partial x)$, the Guo source term [96] (GF) i.e. $F_i = \Delta t\, \omega_i \left(1 - 1/(2\tau)\right) \left[((u \cdot e_i)/c_s^4)e_i + (e_i - u)/c_s^2\right] \cdot (\partial P/\partial x)$, Pressure at inlet and outlet by Zou and He [83] (PP), and as above Velocity at inlet and Pressure at outlet by Zou and He [83] (VP).

Figure 4.13 shows "No Collision" has a lower order of convergence. PP, GF, or CF give the same results for "No Collision" whereas, VP gives the best accuracy. The "Half-Way" technique with VP produces the most accurate one for creeping flows (Figure 4.13) but for a weak laminar flow (Figure 4.14), it is "With Collision" with GF. Thus, the relative errors of velocity confirm the trend of the pressure-drop error that "Half-Way" is better for $Re \leqslant 1$ otherwise "With Collision" produce more accurate results. Figure 4.13 shows GF is preferable to CF for "Half-Way" but the opposite for "With Collision". This rises from the fact GF is a body force (volumetric) whereas CF is a discrete external force. Globally, PP gives errors between GF and CF. When the

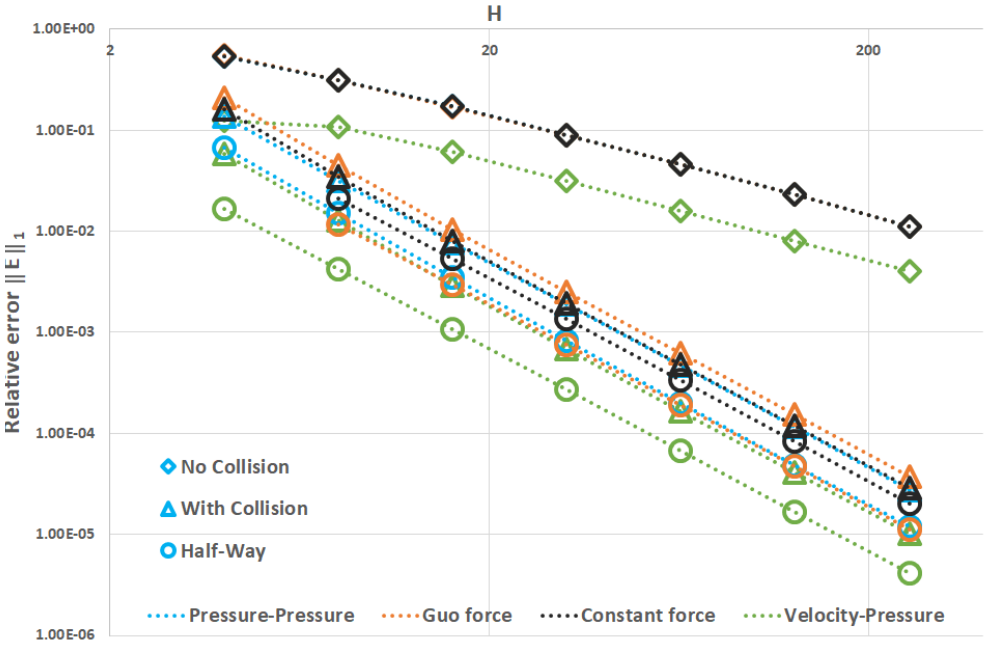

Figure 4.13: The relative error of velocity at Re=0.01 versus channel height.

inertia force becomes non-negligible, the errors rise and especially for a channel height of 4 lattices (Figure 4.14) due to non-linearity of the flow appears. GF and PP give the most and worst accurate, respectively.

The rate of convergence study Figures 4.12, 4.13, and 4.14 show a linear rate of convergence (q) in log scale. Thus, we have extracted the rate of convergence between the grid resolution of 8 and 256 lattices of channel height as

$$q = \log_{32}\left(\|E\|_1 (H = 8) / \|E\|_1 (H = 256)\right) . \tag{4.4}$$

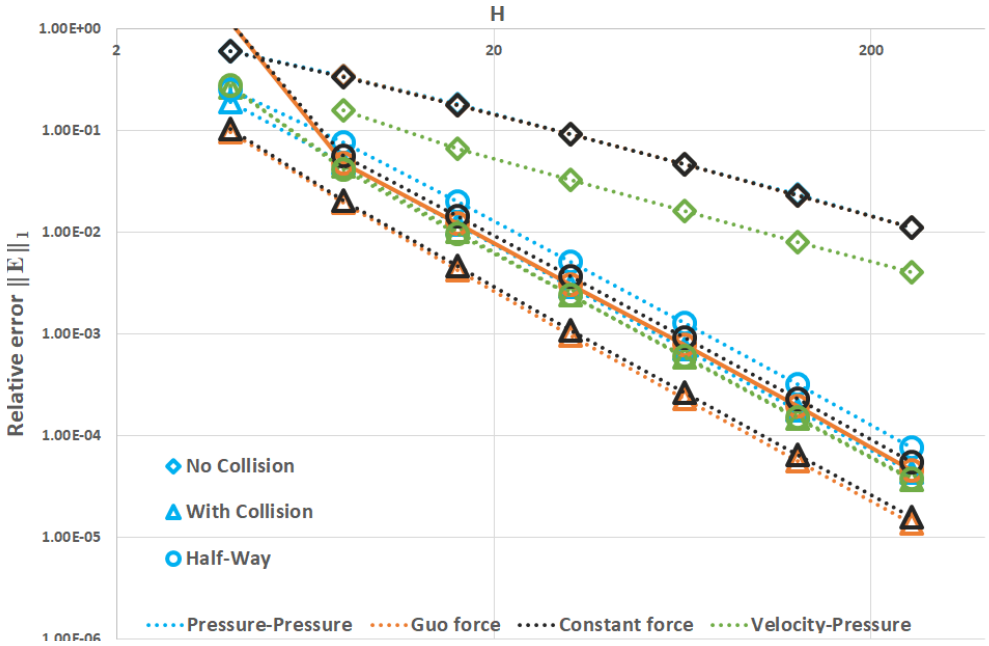

Figure 4.14: The relative error of velocity at Re=10 versus channel height.

The results are summarized in Table 4.4. It is observed that the "No Collision" converges as a first-order scheme whereas, "With Collision" or "Half-Way" converges as a second order scheme. As expected, the collision is needed to obtain higher order rate of convergence and achieves a second-order accuracy.

Rate of convergence

Re		Pressure-Pressure	Guo force	Constant force	Velocity-Pressure
0.01	No Collision	0.96	0.96	0.96	0.95
	With Collision	2.03	2.05	2.05	2.06
	Half-Way	2.06	2.00	2.01	2.00
10	No Collision	0.99	0.99	0.98	1.06
	With Collision	2.03	2.09	2.07	2.05
	Half-Way	1.99	2.00	2.00	2.02

Table 4.4: The rate of convergence for straight channels.

4.2.3 Inclined channels

This case was designed in order to have a channel with two sections inclined by 45°and 5 equal "X" lengths of the centre line of the channel. Design Modeler from ANSYS [129] was used to design it and an image was exported then Matlab from MathWorks [130] was used to scale the image and export to a binary format.

The original image before converting to a binary file at the right scale can be seen in Figure 4.15. However, this geometry cannot keep the same mesh and the same height of channel for full-way and half-way bounce-back treatments. We chose to keep the same mesh to compare our results, thus, the heights of channel are 193 and 20 lattices for the "Half-Way".

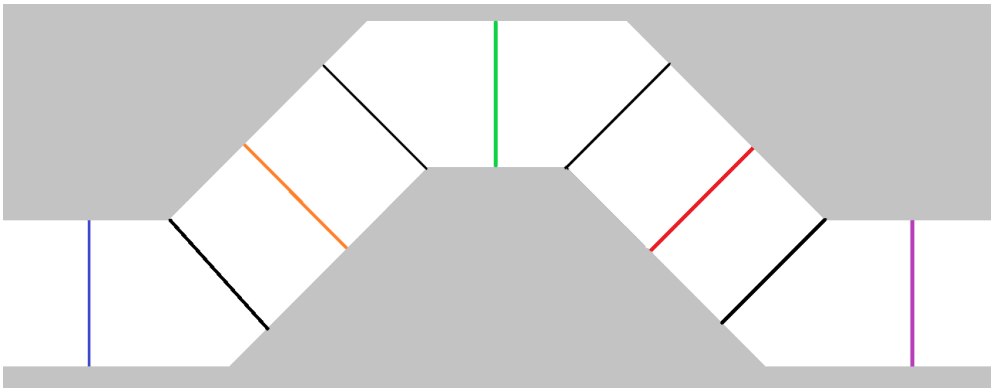

Figure 4.15: The geometry of inclined channels where the dark blue, orange, green, red, and purple lines represent the stations 1,2,3,4, and 5, respectively. The black lines represent the limit of the inclined channels.

4.2.3.1 Effect on velocity and momentum

The accuracy of the velocity profile is critical in case of additional transport properties such as chemical species or light solid particles. In two phase flow, the mass fraction of one fluid needs to be transported. Thus, the inaccuracy of the velocity profile will affect the position of the interface when the capillary number becomes high. Moreover, dealing with a complex geometry and a big domain do not give the opportunity to use a fine grid in each channel. A previous study mentioned at least $4[lu]$ in each channel is needed to support Poiseuille-like behaviour [131]. However, we have noticed for this case it needs at least $10[lu]$ to have an acceptable pressure-drop error (more or less 10%) i.e. similar to the straight channel.

Analysis at the outlet of the inclined channel In this first analysis, we seek to obtain the parabolic velocity profile at the outlet for Reynolds number less than 1.
In Figure 4.16b, for high grid resolution, the outlet velocity profiles show the "New Techniques", "No Collision", and "Half-Way" are able to get the velocity profile in ex-

cellent agreement with SEM whereas, the "No Extrapolation" cannot provide accurate profiles. In case of low grid resolution, the "No Collision" becomes inaccurate as seen in Figure 4.16a.

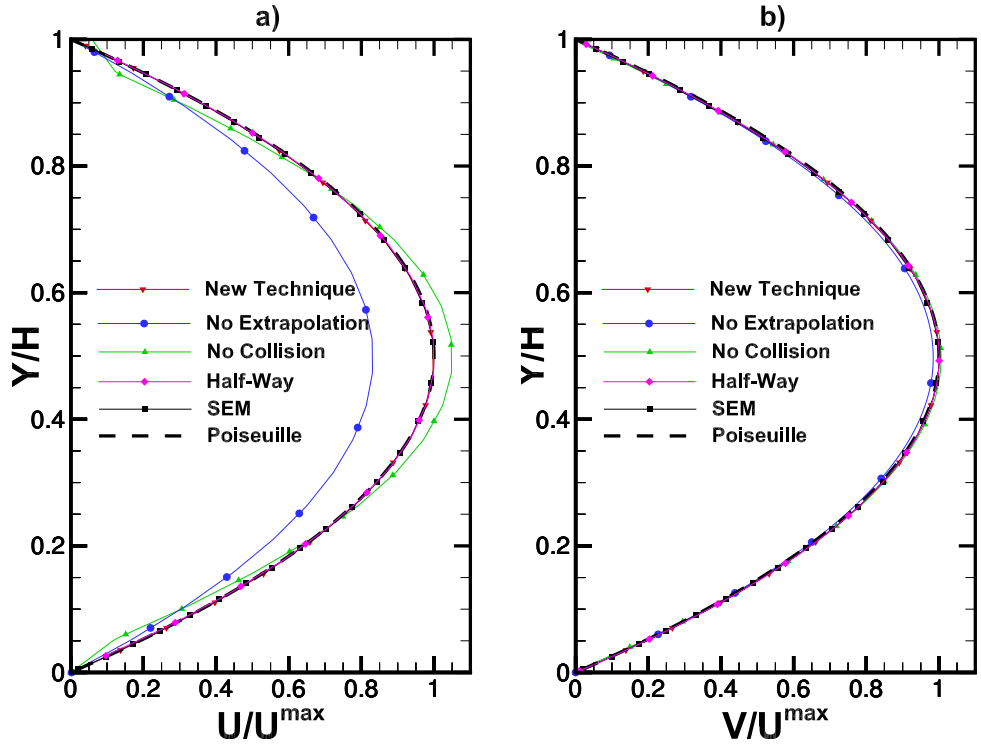

Figure 4.16: Velocity profiles at the outlet: a) low grid resolution and Re = 0.01 and b) high grid resolution and Re = 1.

The momentum is correctly conserved for the "New Technique", "No Collision", and "Half-Way" approaches. However, a loss of momentum conservation appears with the "No Extrapolation". Using the high grid resolution, the loss of momentum is relatively small as it can be seen in Figures 4.16b and 4.17. In case of low grid resolution, the serious loss of momentum conservation is observed with the "No Extrapolation" technique as seen in Figures 4.16a and 4.18. By a trapezoidal integration, the loss of momentum for the "No Extrapolation" is more than 10% but for the other techniques, it is less than 10^{-3}%. Therefore, the "New Technique" improves the velocity profile in case of low grid resolution. Moreover, the normalised velocity profile is not affected by the Reynolds number as expected for creeping flows.

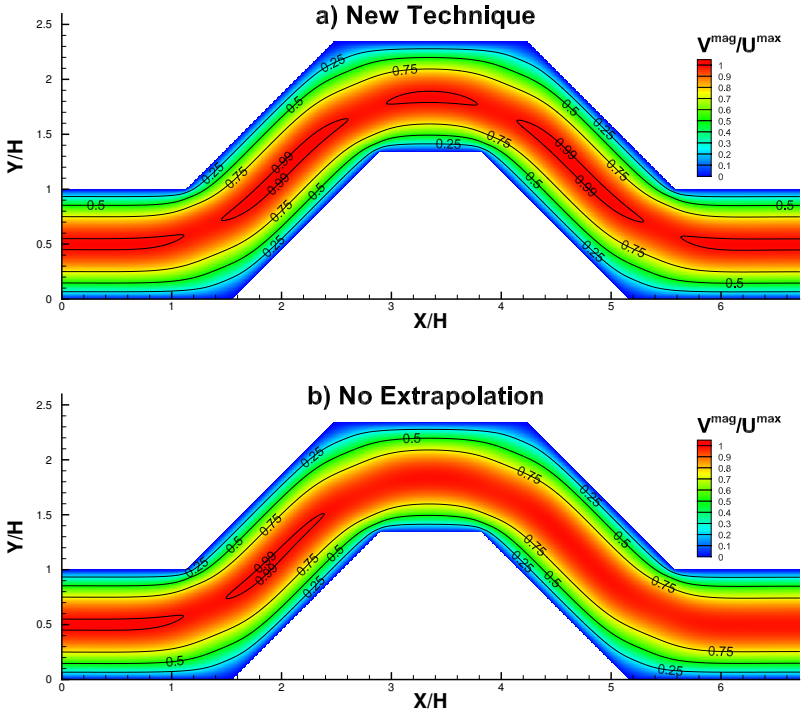

Figure 4.17: Velocity field for high grid resolution

Analysis in the interior of the inclined channel We have seen the "New Technique" conserves the momentum and the velocity profile is correctly captured at the outlet. However, we need an accurate velocity profile everywhere in the domain, thus, we have extracted the velocity profiles in 5 stations as shown in Figure 4.15 and have calculated $\|E\|_1$ i.e. the relative error norm as in Equation 4.3 where N is the number of extracted points and U_c and U_a are the magnitude velocity calculated from the LBM results and the analytical solution, respectively.

Velocity profiles In Figure 4.19a, the velocity profiles at the station 2 for low grid resolution show that the "Half-Way" agrees with both SEM and Poiseuille profiles, but, the "No Collision" does not agree and has an overshoot at the centre line and undershoot at the wall. The "No Extrapolation" exhibits a loss of momentum. The "New Technique" agrees quite accurately, however, the height of the channel at the station 2 is smaller than H owing to inclined nature of the channel. The reduced height is due to the stair-like pattern used to represent inclined walls in this method. The

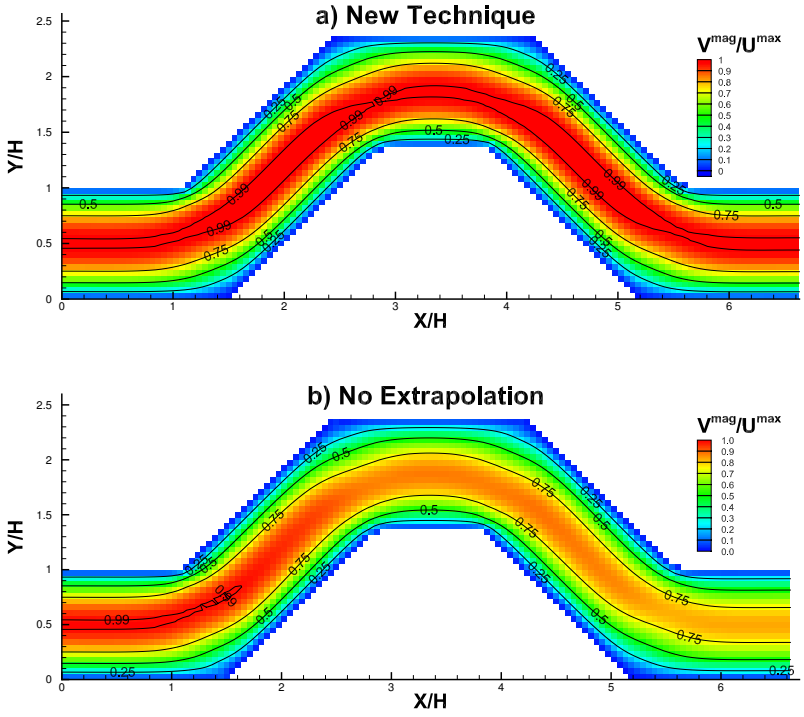

Figure 4.18: Velocity filed for low grid resolution

effect of the geometry-imposed constriction results in a slight overestimation of the velocity at the centre line in order to conserve momentum. Moreover, the deviation of the velocity at the wall comes from the no-slip condition imposed by the full-way bounce-back rule.

In Figure 4.20, the velocity profiles at station 3 is shown. This is the straight part at the middle of the geometry. The constriction effect due to the stair-like pattern does not influence this region i.e. the surface is aligned with the lattice. Thus, as seen in straight channel analysis, Figure 4.20 shows a very good agreement between the "New Technique", "SEM", "Half-Way" and the analytical result. For the "No Extrapolation" and the "No Collision" shows inaccuracy.

Similar results to station 2 are observed for station 4 with more loss of momentum for the "No Extrapolation" as shown in Figure 4.21.

Velocity profile errors Looking at the error norms based on the analytical solution i.e. a parabolic profile, the error is reduced by a factor 0.1 between the low resolution (Figure 4.22) and the high resolution (Figure 4.23) as expected i.e. linear

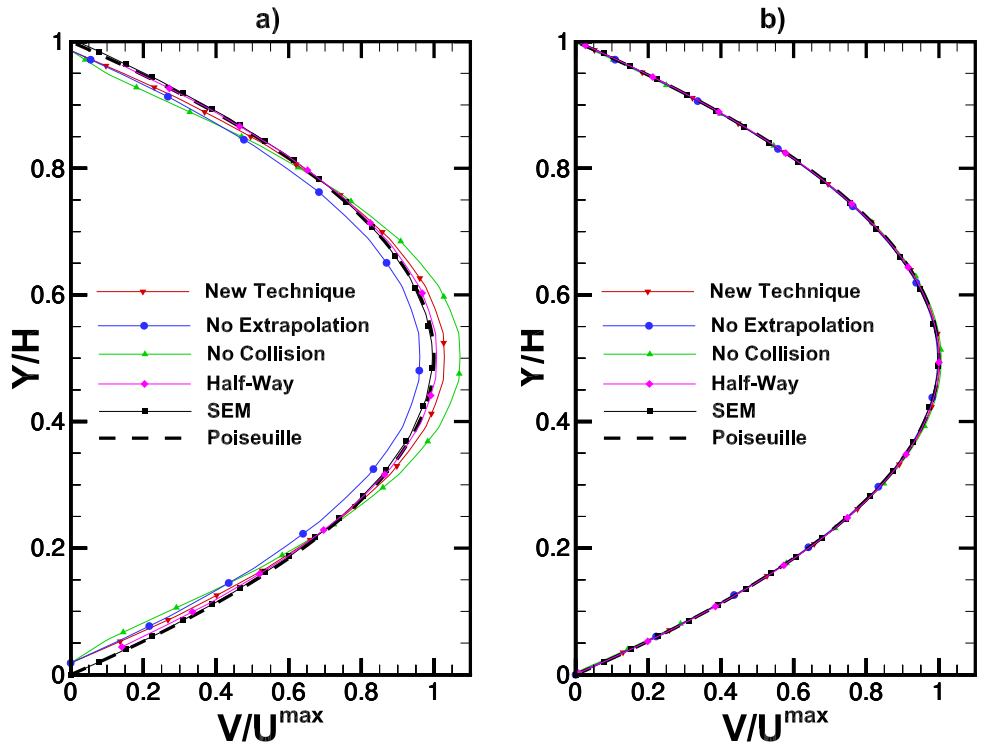

Figure 4.19: Velocity profiles at station 2: a) low grid resolution and Re = 0.01 and b) high grid resolution and Re = 1.

convergence.

The "Half-Way" and "SEM" results are essentially the same for Re= 0.01 or 1 and the low or high grid resolutions. The "New Technique" has some discrepancy for the inclined parts, however it is almost two times better than "No Collision" and four times better than "No Extrapolation".

At low grid resolution, the errors of each methods are similar for Re $\leqslant$ 1 (Figures 4.22 and 4.24). However, the inertia starts to affect the solution at Re = 1 for the high grid resolution (4.23, and4.25). Note that we have also extracted the errors for Re=0.1 and the low or high grid resolutions with the similar results to Re=0.01.

The errors are accumulated for the "No Extrapolation" case due to the loss of momentum. We can notice the parabolic profile becomes less valid for Re=1 as shown in Figure 4.25.

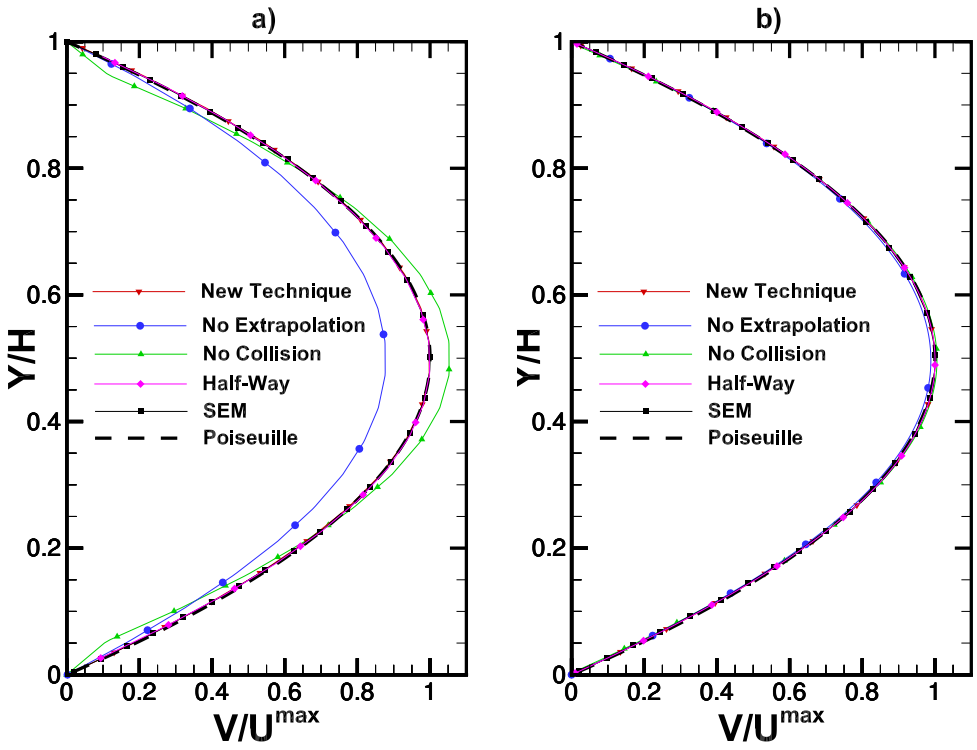

Figure 4.20: Velocity profiles at station 3: a) low grid resolution and Re = 0.01 and b) high grid resolution and Re = 1.

4.2.3.2 Effect on the pressure-drop

It is important to calculate the right pressure-drop, especially in low speed flows since at the incompressible limit, the velocity and density are directly coupled. Indeed, the Navier-Stokes equations become elliptical. However, in two phases flow, the local pressure gradient is also important because this could change the shape and the displacement of an interface between two immiscible fluids.

This "New Technique" improves the prediction of the pressure-drop in case of low resolution. In Figure 4.26, it can be clearly seen that the inaccurate value of density at the walls is predicted for the "No Collision" case. The "No Extrapolation" technique for the inclined parts yields very strange profiles (Figure 4.26).

In Table 4.5, the pressure-drop is compared to the results from SEM. It can be clearly seen that the pressure-drop is not correctly calculated in case of "No Collision" while the results of the "New Technique" and SEM are in good agreement. It can be no-

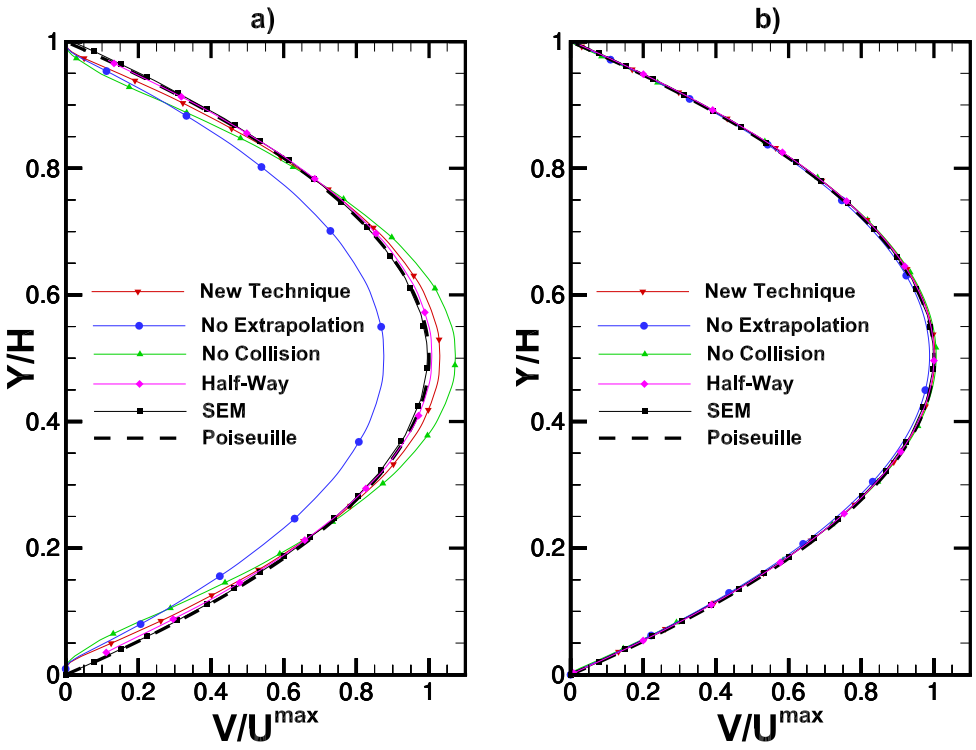

Figure 4.21: Velocity profiles at station 4: a) low grid resolution and Re = 0.01 and b) high grid resolution and Re = 1.

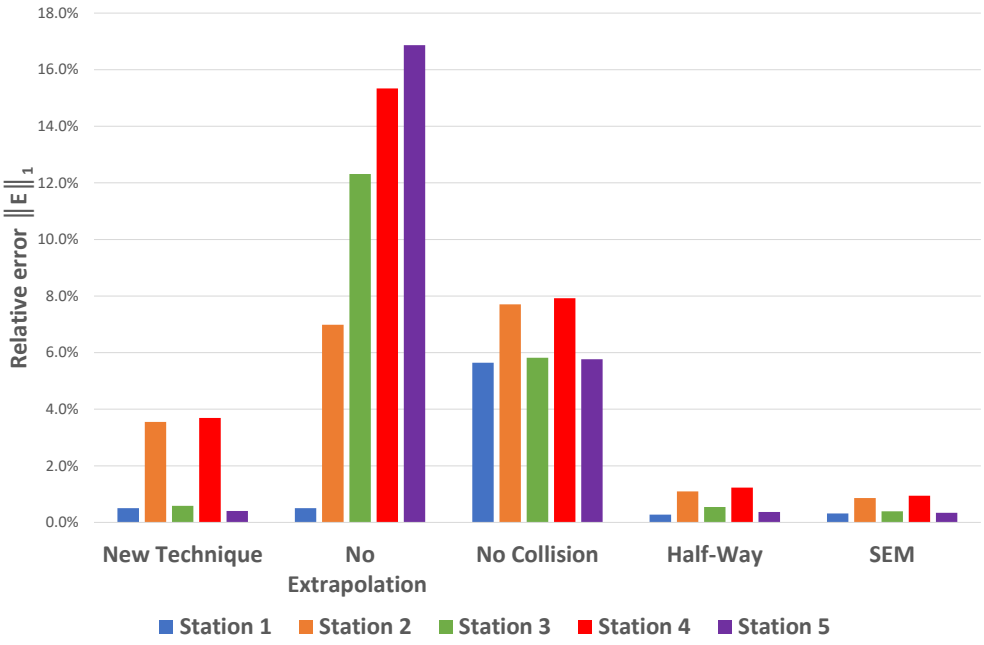

Figure 4.22: $\|E\|_1$ for low grid resolution and Re=0.01

ticed that the "Half-Way" technique cannot converge under 1% since the shear stress is taken in account at half lattice from the wall which leads to errors when the flow is

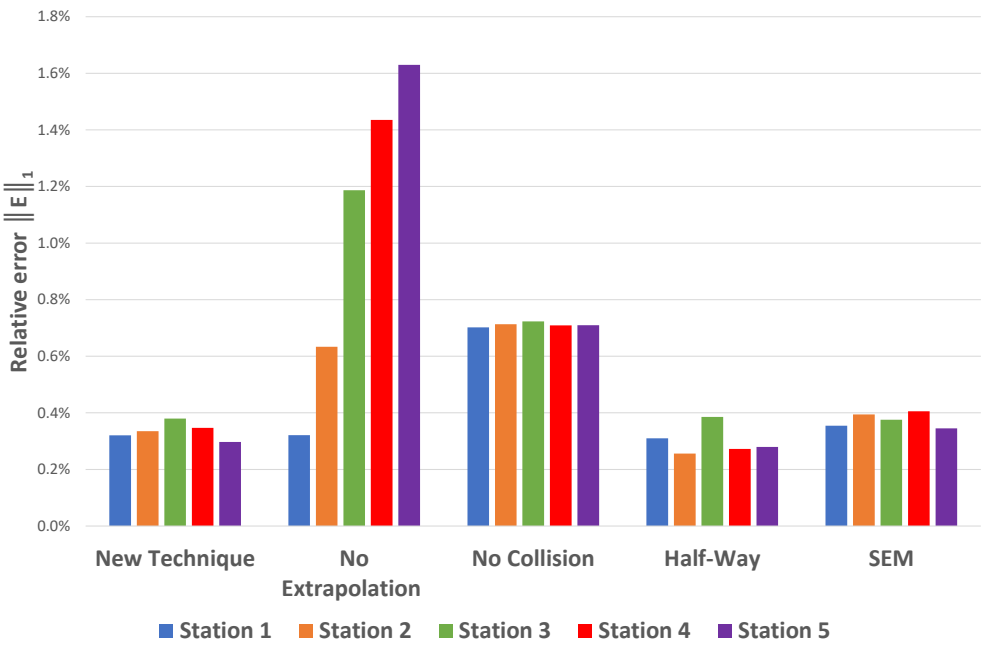

Figure 4.23: $\|E\|_1$ for high grid resolution and Re=0.01

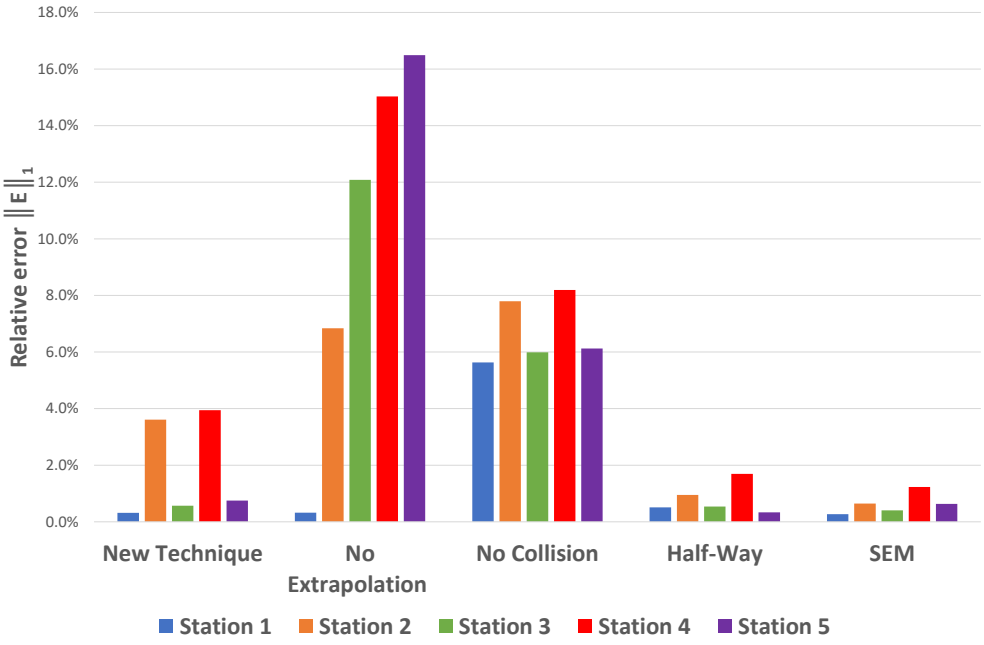

Figure 4.24: $\|E\|_1$ for low grid resolution and Re=1

not parallel to the lattices.

Moreover, we notice the error without collisions on walls increases compared to a straight channel. This suggests that for a single-phase flow with a very complex geometry such as porous media, the effect of the collision could be not negligible in a

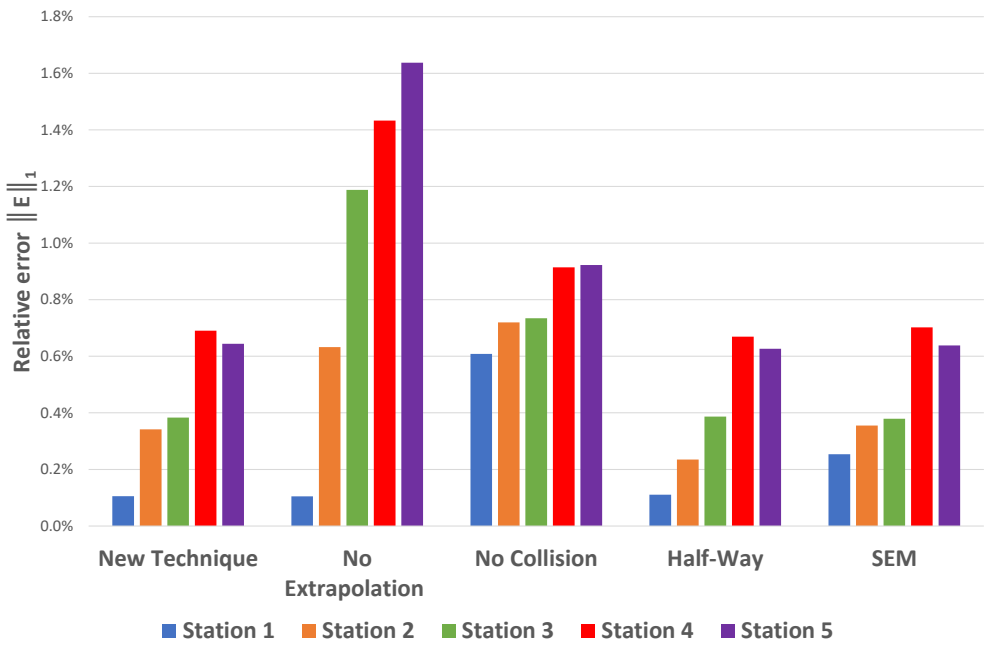

Figure 4.25: $\|E\|_1$ for high grid resolution and Re=1

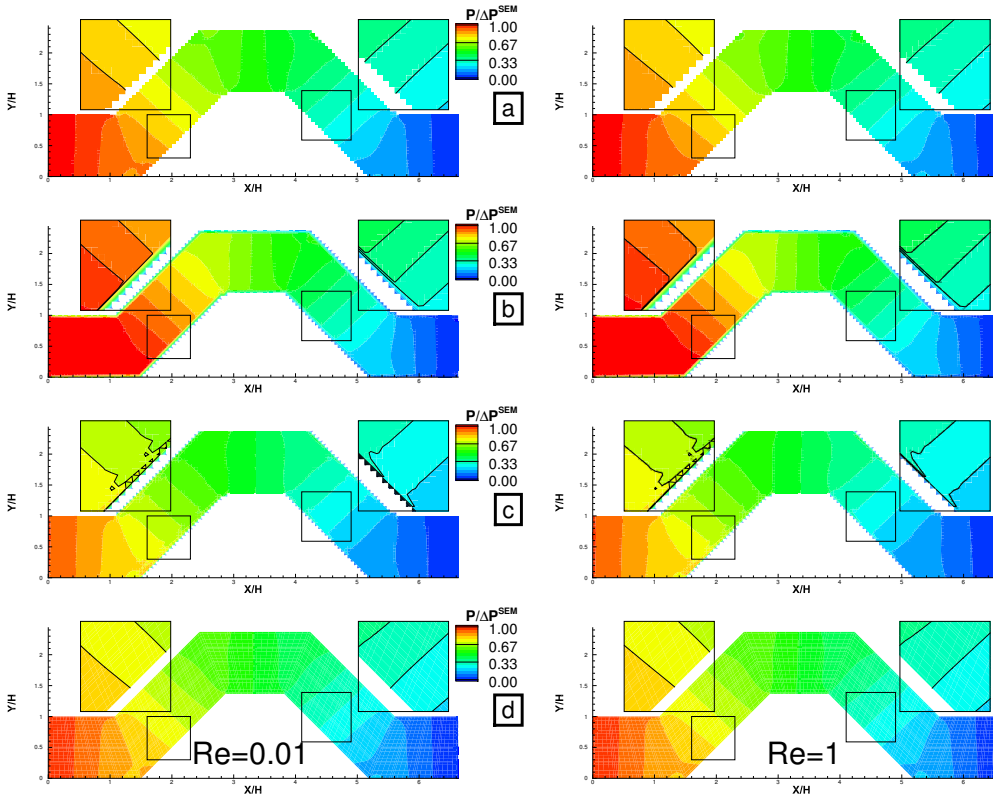

Figure 4.26: Comparison of pressure field to SEM results; a) New Technique, b) No Collision, c) No Extrapolation, and d) SEM.

Inclined channels					
	Re	**New Technique**	**No Extrapolation**	**No Collision**	**Half-Way**
Low Resolution	10	12.20%	2.74%	29.59%	3.45%
	1	6.17%	4.90%	21.04%	7.85%
	0.1	5.66%	5.08%	20.32%	8.22%
	0.01	5.61%	5.10%	20.25%	8.25%
High Resolution	10	0.36%	1.67%	0.91%	1.01%
	1	0.31%	1.57%	0.70%	1.01%
	0.1	0.30%	1.56%	0.68%	1.01%
	0.01	0.28%	1.53%	0.68%	1.18%

Table 4.5: Pressure-drop errors for a Poiseuille-like flow in the inclined channels.

single-phase flow.

4.3 The Laplace's law

The Laplace's law [132] is a well-known relation between the jump of pressure at the interface, surface tension and curvature for static droplets. In 2D, the Laplace's law is

$$\Delta P = \frac{\sigma}{R}, \tag{4.5}$$

and in 3D,

$$\Delta P = \frac{2\sigma}{R}, \tag{4.6}$$

where R is the radius of the droplet. This law is also known as Young-Laplace equation due to Laplace created this law based on the theoretical formalism of Young (no mathematics formalism) [133].

In order to keep $Kn \ll 1$, the radius of the droplet and the size of the domain are kept to $20[lu]$ and $100^2[lu]$, respectively and the dynamic viscosity of the droplet is kept to $1/36[lu]$. The coefficient β (recolouring operator) is set to be 0.99. The boundary conditions of the domain are set to wall boundary conditions. The surface tension varies from $10^{-6}[lu]$ to $10^{-2}[lu]$.

The Lishchuk approach (CSF) and the Reis approach (Reis) will be compared, which were described in subsubsection 3.3.4.1. The effect of the calculation of the gradient will be also compared with the 2^{nd}-order finite difference and the 4^{th}-order compact

scheme. The viscosity ratio is calculated as

$$\lambda = \frac{\nu^m}{\nu^d}, \tag{4.7}$$

where ν^m and ν^d are the dynamic viscosity of the matrix and the droplet, respectively. The calculation is stopped when the error of the density over the domain is less than 10^{-10}. Only the case of $\sigma = 0.01[lu]$ and $\lambda = 1$ with the Reis' model and 2^{nd} order colour gradient could not converge less than $2 \cdot 10^{-10}$. It is quite surprising to notice this discrepancy only for a unity viscosity ratio.

4.3.1 Effect of the viscosity ratio

The viscosity ratio is set to 0.5, 1, 2, and 10. Firstly, we analyse the error of the simulation for a viscosity ratio of unity. The error is defined as

$$Error = \frac{\left|\Delta P^{La} - \Delta P\right|}{\Delta P^{La}}, \tag{4.8}$$

where ΔP^{La} and ΔP are the difference of pressure of the Laplace's law and the simulation, respectively. The Figure 4.27 shows the very good agreement with the analytical solution. However, we can notice a discrepancy for the Reis' model with the 2^{nd}-order colour gradient due to the approach creates a lot of spurious currents and, thus, it could not converge further. When the surface tension reduces, the accuracy reduces for the 2^{nd}-order case. This can be caused by the isotropic or the spatial errors of the gradient. If we look more carefully at the results (Table 4.6), we can see the difference from the Reis and CSF models are negligible compared to the accuracy of the gradient.

In case the droplet is two times more viscous than the matrix, the Table 4.7 shows the errors is similar to the unit case (Table 4.6) or a little lower error. This arises from the reduced collision rate in the matrix, so the matrix plays less role in the solution.

In case the viscosity of the matrix is higher than the viscosity of the droplet (Tables 4.8 and 4.9), the errors are globally higher than the unity viscosity ratio case. Surprisingly for a surface tension of $10^{-3}[lu]$, the errors for 2^{nd} order colour gradient are lower

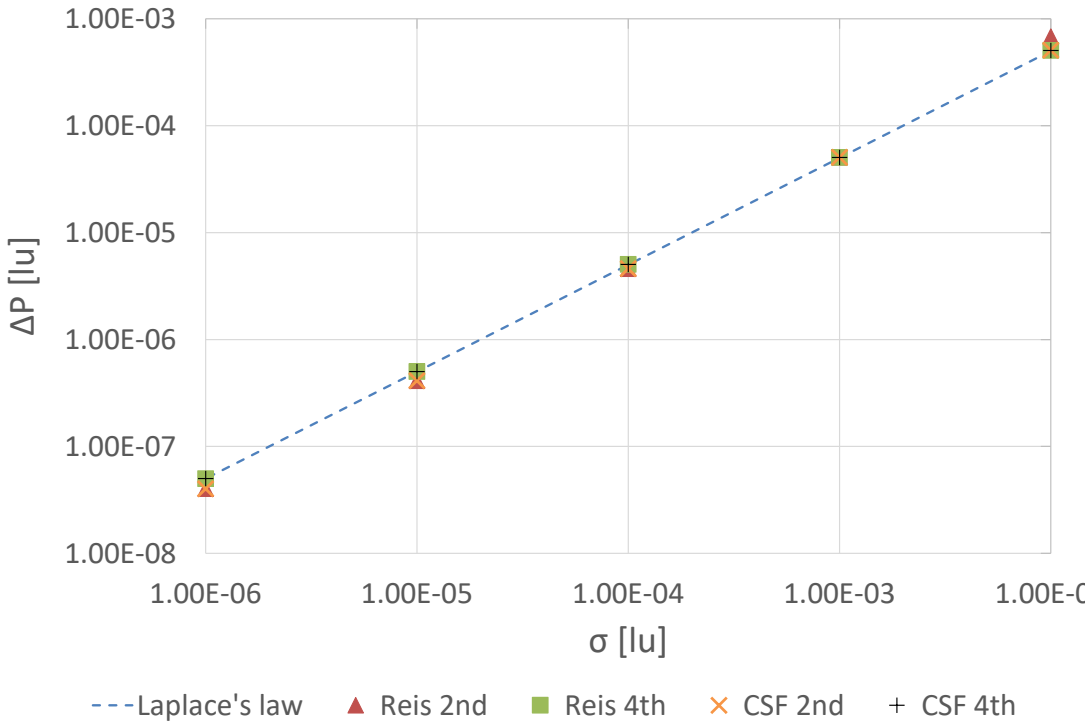

Figure 4.27: The Laplace's law with $\lambda = 1$.

	The Laplace's law	**Reis 2nd**	**Reis 4th**	**CSF 2nd**	**CSF 4th**
Surface tension [lu]	ΔP **[lu]**				
1.00E-02	5.00E-04	6.82E-04	5.06E-04	5.09E-04	5.06E-04
1.00E-03	5.00E-05	5.06E-05	5.05E-05	5.06E-05	5.06E-05
1.00E-04	5.00E-06	4.59E-06	5.03E-06	4.60E-06	5.03E-06
1.00E-05	5.00E-07	4.12E-07	5.01E-07	4.12E-07	5.01E-07
1.00E-06	5.00E-08	4.02E-08	5.00E-08	4.02E-08	5.00E-08
Surface tension [lu]		**Errors**			
1.00E-02		36.45%	1.14%	1.82%	1.16%
1.00E-03		1.15%	1.10%	1.15%	1.13%
1.00E-04		8.23%	0.62%	8.10%	0.65%
1.00E-05		17.67%	0.15%	17.62%	0.19%
1.00E-06		19.60%	0.07%	19.57%	0.02%

Table 4.6: Numerical errors and ΔPs for the Laplace's law with $\lambda = 1$.

	The Laplace's law	Reis 2nd	Reis 4th	CSF 2nd	CSF 4th
Surface tension [lu]	ΔP **[lu]**				
1.00E-02	5.00E-04	5.35E-04	5.06E-04	5.09E-04	5.06E-04
1.00E-03	5.00E-05	5.09E-05	5.06E-05	5.08E-05	5.06E-05
1.00E-04	5.00E-06	4.75E-06	5.04E-06	4.75E-06	5.04E-06
1.00E-05	5.00E-07	4.28E-07	5.02E-07	4.28E-07	5.02E-07
1.00E-06	5.00E-08	4.18E-08	5.01E-08	4.17E-08	5.01E-08
Surface tension [lu]		**Errors**			
1.00E-02		7.02%	1.15%	1.86%	1.16%
1.00E-03		1.73%	1.13%	1.65%	1.14%
1.00E-04		4.94%	0.78%	5.01%	0.80%
1.00E-05		14.33%	0.44%	14.46%	0.46%
1.00E-06		16.35%	0.22%	16.52%	0.25%

Table 4.7: Numerical errors and ΔPs for the Laplace's law with $\lambda = 0.5$

than 4^{th} order cases. No explanation has been found to explain it.

	The Laplace's law	Reis 2nd	Reis 4th	CSF 2nd	CSF 4th
Surface tension [lu]	ΔP **[lu]**				
1.00E-02	5.00E-04	5.12E-04	5.06E-04	5.09E-04	5.06E-04
1.00E-03	5.00E-05	5.02E-05	5.06E-05	5.04E-05	5.06E-05
1.00E-04	5.00E-06	4.34E-06	5.02E-06	4.36E-06	5.02E-06
1.00E-05	5.00E-07	3.99E-07	4.99E-07	4.00E-07	5.00E-07
1.00E-06	5.00E-08	3.91E-08	4.98E-08	3.93E-08	4.99E-08
Surface tension [lu]		**Errors**			
1.00E-02		2.32%	1.13%	1.81%	1.16%
1.00E-03		0.49%	1.14%	0.74%	1.15%
1.00E-04		13.29%	0.41%	12.90%	0.43%
1.00E-05		20.26%	0.14%	20.00%	0.09%
1.00E-06		21.72%	0.32%	21.46%	0.27%

Table 4.8: Numerical errors and ΔPs for the Laplace's law with $\lambda = 2$.

4.3.2 Spurious currents

In a static case, the velocity should vanish. However, spurious currents are seen due to models and numerical techniques. Several studies were published, and the origin of the spurious currents is still not clear. In the colour fluid model, the recolouring

	The Laplace's law	Reis 2nd	Reis 4th	CSF 2nd	CSF 4th
Surface tension [lu]	ΔP **[lu]**				
1.00E-02	5.00E-04	5.36E-04	5.10E-04	5.32E-04	5.06E-04
1.00E-03	5.00E-05	4.77E-05	5.10E-05	4.73E-05	5.06E-05
1.00E-04	5.00E-06	4.10E-06	5.03E-06	4.12E-06	5.00E-06
1.00E-05	5.00E-07	3.96E-07	5.01E-07	3.98E-07	4.98E-07
1.00E-06	5.00E-08	3.95E-08	5.01E-08	3.96E-08	4.97E-08
Surface tension [lu]		**Errors**			
1.00E-02		7.23%	1.94%	6.38%	1.13%
1.00E-03		4.64%	2.01%	5.31%	1.23%
1.00E-04		17.94%	0.68%	17.59%	0.08%
1.00E-05		20.73%	0.24%	20.47%	0.50%
1.00E-06		21.09%	0.18%	20.82%	0.56%

Table 4.9: Numerical errors and ΔPs for the Laplace's law with $\lambda = 10$.

step is greatly responsible for the parasitic current generation. Leclaire, by modifying the recolouring operator, has reduced the spurious current significantly for a static case [134]. Meanwhile, higher-order Lattice Boltzmann can also reduce the spurious current [135]. Lee also proposed to calculate the intermolecular force in the pressure form [136], however, the momentum is not conserved. Moreover, the discretisation of the colour gradient has an impact too through increased accuracy order of gradients in the spatial and isotropic, but the spurious currents are not completely removed [109]. Here, we try to highlight the effect of the model and the choice of gradients on the production of the parasitic current. We keep the same previous cases of the Laplace's law errors. All the next plots of this section have:

- The 2^{nd} and the 4^{th} order colour gradients are on the two top and bottom quarters, respectively.
- The CSF and the Reis' models are on the two left and right quarters, respectively.
- The scale of the velocity magnitude is based on the CSF model with the 4^{th} order colour gradient.
- The streamlines are represented in black and only on half of each quarter.
- The dashed line represents the interface between the two fluids.

As seen in Figure 4.28, the CSF and Reis' models behave similarly when the viscosity is unity and when the surface tension is quite low. When the surface tension increases, the behaviour of the two models differ (Figure 4.29). The interface has minor effects on the streamline for CSF. But for Reis' model, two vortices at each side of the interface can be seen which modify the droplet size due to the stress generated by the vortices. Clearly, the 2^{nd} order colour gradient generates more spurious current due to only 2^{nd} order accuracy in space and the interface is not circular due to the anisotropy of the gradient.

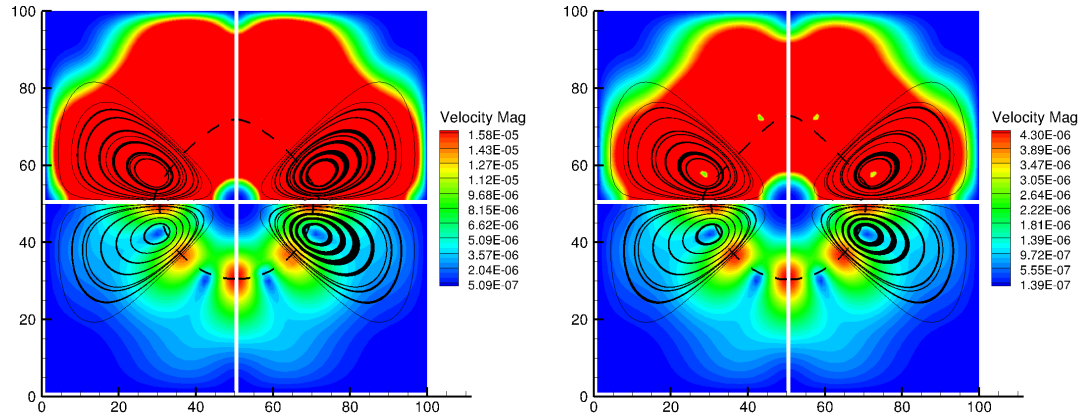

Figure 4.28: Spurious currents for $\lambda = 1$ and $\sigma = 10^{-4}[lu]$ and $10^{-5}[lu]$ on the left and right, respectively.

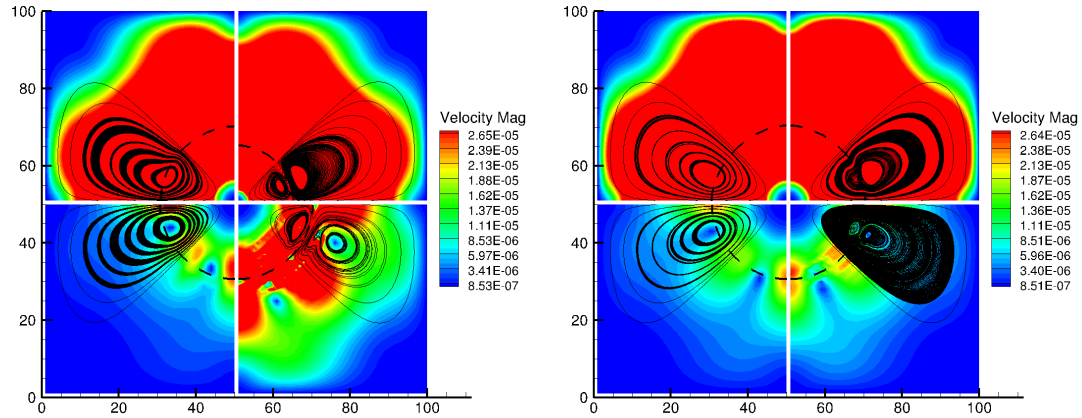

Figure 4.29: Spurious currents for $\lambda = 1$ and $\sigma = 10^{-2}[lu]$ and $10^{-3}[lu]$ on the left and right, respectively.

When the viscosity ratio decreases (matrix with a lower viscosity), as shown in the Figures 4.30 and 4.31, the CSF model produces less spurious current than Reis' model, but both produce more spurious current than the unity viscosity ratio case.

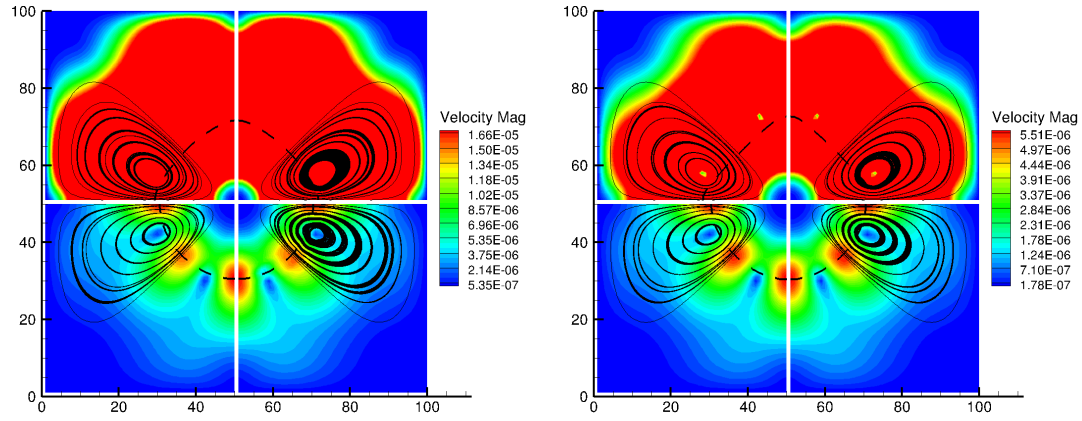

Figure 4.30: Spurious currents for $\lambda = 0.5$ and $\sigma = 10^{-4}[lu]$ and $10^{-5}[lu]$ on the left and right, respectively.

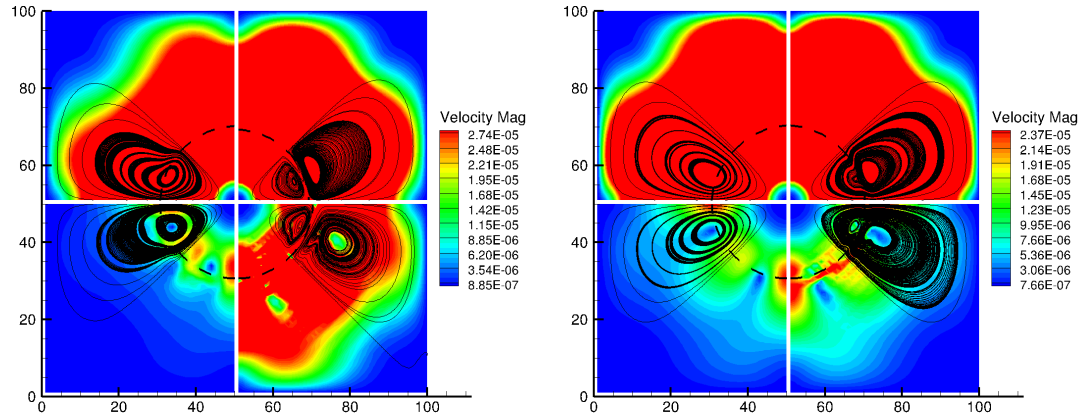

Figure 4.31: Spurious currents for $\lambda = 0.5$ and $\sigma = 10^{-2}[lu]$ and $10^{-3}[lu]$ on the left and right, respectively.

When the droplet has a lower viscosity (Figures 4.32, 4.33, 4.34, and 4.35), the spurious currents stay almost the same as the unity viscosity ratio case. It can be observed that the Reis' model generates a vortex in each part of the interface when the viscosity ratio increases. However, the spurious current magnitude is higher compared to the CSF model.

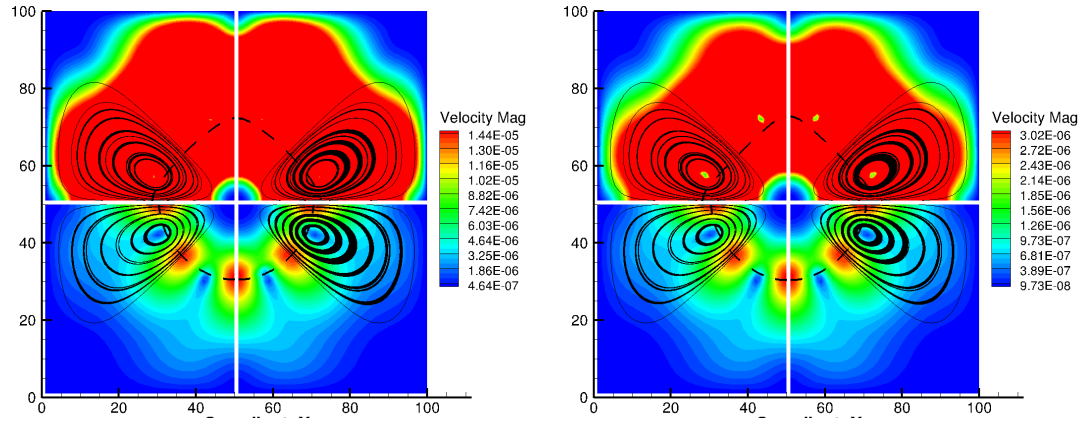

Figure 4.32: Spurious currents for $\lambda = 2$ and $\sigma = 10^{-4}[lu]$ and $10^{-5}[lu]$ on the left and right, respectively.

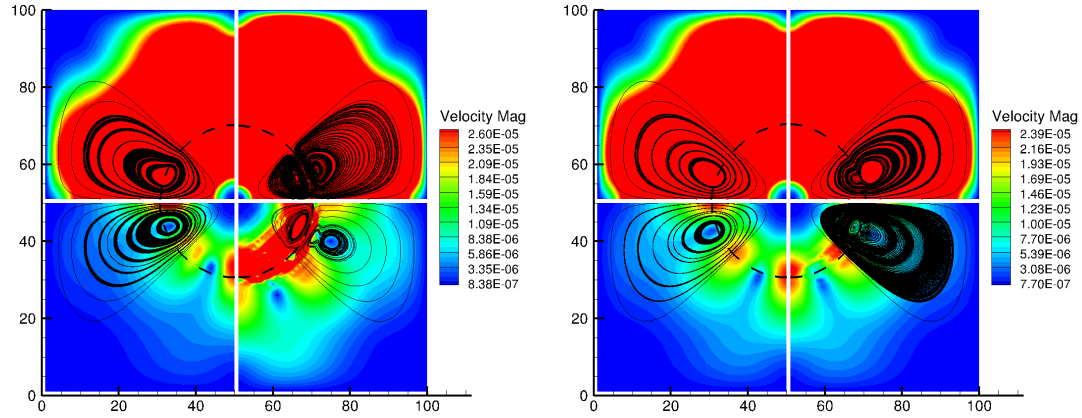

Figure 4.33: Spurious currents for $\lambda = 2$ and $\sigma = 10^{-2}[lu]$ and $10^{-3}[lu]$ on the left and right, respectively.

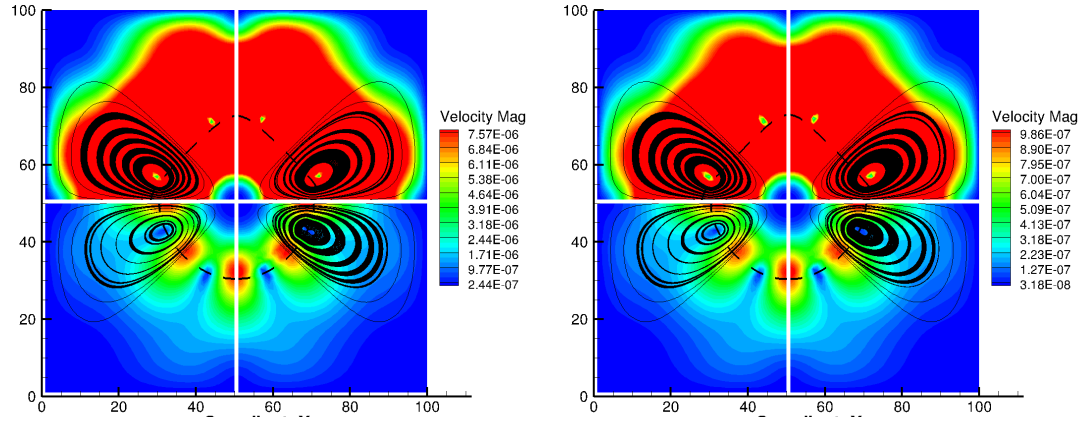

Figure 4.34: Spurious currents for $\lambda = 10$ and $\sigma = 10^{-4}[lu]$ and $10^{-5}[lu]$ on the left and right, respectively.

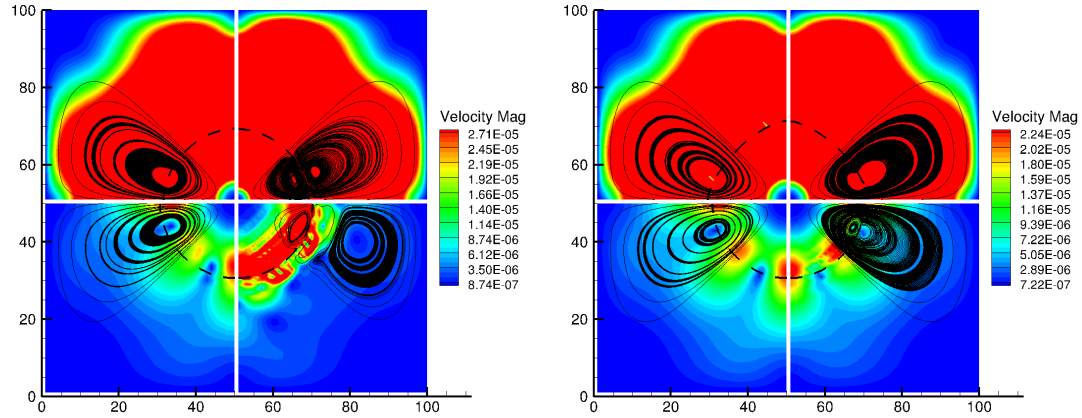

Figure 4.35: Spurious currents for $\lambda = 10$ and $\sigma = 10^{-2}[lu]$ and $10^{-3}[lu]$ on the left and right, respectively.

During this test, we did not notice a big difference on computational cost due to we used a limited number of processors (4 to 10). For more processors, CSF could perform slower due to the calculation of curvature needs to synchronise the colour gradient.

4.4 Chapter summary

On the 2D lid-driven cavity with single-phase flow, the new platform performs well for a relativity high number of cores and is accurate for a large range of Reynolds numbers from 100 to 3200. The implementation of the boundary conditions employed (bounce back, Zou and He and Ho) for the simulations have been considered as validating.

We successfully designed a new boundary condition to improve the velocity profile and the pressure drop in complex geometries. This is based on the bounce-back rules with the inverse distance weighting extrapolation of the density on concave corners and a collision rule. In single-phase flow, the new technique achieves excellent results for a low grid resolution and low Reynolds number.

The collision on surfaces was shown to play an important role in the redistribution of the mass and momentum. In the collision process, the density value has to be the most realistic to conserve the momentum which the “new technique” excels at low Reynolds.

We have studied the Laplace's law and compared the errors with the Reis and CSF models and the classical FD 2^{nd} and 4^{th} order gradients for the colour gradient. The 2^{nd} brings quite a lot of error in term of accuracy of the Laplace's law, generates much more spurious current and deform the interface. The two models give globally the same accuracy for the Laplace's law.

Chapter 5

Contact angle treatment

This chapter describes the contact angle treatments implemented in our LBM platform with the validations and an application on a sample of Berea sandstones [6]. We implemented a standard approach, commonly used in commercial software such as Fluent from ANSYS [137], and created a smooth contact angle approach. We validated for the static cases on flat and inclined walls and for the dynamic cases on serpentine and inclined channels. We have extracted the relative permeability, mobility ratio, capillary number and saturation from the Berea sandstone sample with viscosity ratio of 2 and 5, and contact angles of $10°, 45°, 90°, 170°$ and free (no constraint on it).

5.1 Introduction

The phenomena of the contact angle have been studied for centuries. For instance, the famous law of Jurin [138] was proposed in 1717, which describes the height of a fluid rising in a capillary due to the contact angle. Young [133] created the concept of equilibrium of forces acting on the triple line which generates the contact angle. Dupré [139] added the energy to the concept of Young and created the well-known Young-Dupré's law

$$\cos(\theta) = \frac{\gamma_{sl} - \gamma_{sv}}{\gamma_{lv}}, \tag{5.1}$$

where γ are the interfacial tensions between two components, the subscripts $_{s,l}$ and $_v$ are for solid, liquid and vapour, respectively. The vapour can be replaced by another liquid.

Laplace worked also on this subject and described the variation of pressure between the interface of two fluids. He created the Laplace's law [132]

$$\Delta P = \sigma \nabla \cdot n. \tag{5.2}$$

However, all this work was done for static contact angles, but the interface forces depend on the fluid motion as well. Indeed, the shear stress changes the interface forces, so the contact angle. The shear stress can be decomposed into two parts: the wall shear stress (the adherence force) and the normal shear stress. The adherence force is mainly due to the Van der Waals force. The normal shear stress is due to the fluid motion and the viscosity.

Taylor in 1962 [140] may have been the first to study the invalid non-slip condition at the triple line. He noticed the continuum hydrodynamic approach cannot deal with the velocity singularity for a Taylor scraping flow (two-dimensional corner flow). With the continuum fluid assumption, this "corner flow" generates an infinite shear and an infinite force. The typical image to represent this phenomenon is a painter using his spatula. Without a slip velocity, the painter would not be able to move the paint with the spatula.

Different contact angles can be defined i.e. microscopic, dynamic, or apparent, which need different models [141]. All has been wildly studied since decade in term of experimental, analytical, or numerical work [142–145]. With the new experimental techniques, the dynamic of the contact lines has been more precise as in the work of Katoh *et al* [146] where several dynamic experiments where performed (liquid-liquid contact line in a capillary tube, liquid-gas of a two-dimensional meniscus, and an axisymmetric droplet) and he highlighted the effect of roughness or impurities on the solid surface to influence the dynamics of the triple line. Pore-scale experiments were performed by Andrew *et al* [147] and they were able to measure the contact line inside an hetero-

geneous structure (rock). Afkhami *et al* [141] proposed a new boundary condition for Volume Of Fluid methods to improve the stress singularity at the contact line created by the traditional slip condition. Later on, molecular dynamics has been used and compared to VOF with quite good agreement [148].

Using Lattice Boltzmann Method (LBM) which is a mesoscopic particle-based method derived from Boltzmann equation and Lattice Gas Automata (LGA) [56] and the colour fluid model introduced by Rothman and Keller [1], different models can be found in the literature to define the contact angle e.g. Guntensun [4] chose to use the Young-Dupré's law, Leclaire [149] used the secant method to redistribute the density between the two fluids. The hysteresis approach has been also successfully used by Liu [114]. The method can also be extended to more than two fluids [91] but we will limit here to two immiscible liquids. We also restrict our discussion to two fluids with the same density although it can be used for fluids with different densities [92].

Choosing LBM to treat porous media can cause a misalignment between the geometry (walls) and the Cartesian grid (lattice) [90]. Enforcing the alignment leads to the generation of "stairs" which introduces concave and convex corners. Using a classical scheme for the Lattice Boltzmann Method, the normal of the interface is not correctly evaluated. We proposed to estimate it by using the mesh and a linear least-square method.

5.2 Contact angle treatment

The key idea of all contact angle treatment is to define the normal of the interface according to the contact angle. In the standard approach, the theoretical value is directly used to define the normal of the interface. In the smooth treatment, an estimation of the contact angle is used to define the normal of the interface.

5.2.1 Standard treatment of contact angle

This treatment is very simple and used in most CFD software such as Fluent from ANSYS [137]. The contact angle is fixed between two fluids and set up at the beginning

of the simulation. It can be extended to models for dynamic and/or hysteresis contact angles where the contact angle can be defined by several approaches. A good review of models was done by Eral *et al* [150].

In this chapter, we consider this as the standard approach, commonly used in VOF models such as in Fluent [137], the modification of the normal direction of the interface in the CSF and the recolouring step by the theoretical contact angle which can be the equilibrium contact angle, the advancing or receding contact angle in case of hysteresis, or the dynamic contact angle in case of dynamic models. Only the equilibrium contact angle is used in this work due to other type of contact angles are not known.

5.2.2 Smooth treatment for complex geometries

In complex geometries, it is often difficult to have an accurate representation of the walls. Indeed, the mesh needs to represent curves. Rarely, curved cells are used in CFD (computationally very expensive). Therefore, the curves are represented with a linear approach in the best cases for the NS solvers and "stairs" for LBM. Those approaches can generate wrong contact angle behaviour when it used with the standard treatment. In order to improve it, an estimator has to be defined and it can be done by several ways. The first way is to refine the mesh, for the NS solvers, in order to reduce the variation of the contact angle. However, it is not always possible to refine. In case of low resolution of the geometry as in porous media, the refinement can change the geometry. By refining, the contact angle type (microscopic, dynamic, or apparent) can change which needs different models [141]. The refinement can break the continuum fluid assumption too. Refinement also increases the computational cost and it can become unaffordable. Moreover, in case of the Cartesian grid, as used in LBM, the "stairs" will stay with the refinement.

Smooth approach

To treat walls misaligned with the lattice, a new approach needs to be used. Leclaire [151] firstly proposed this approach by using a mathematical approach (circles, flat plates, etc.) to define the real surface. For a complex geometry, this definition of the surface can be complex for instance you could need to reconstruct the surface and use

a large number of nodes to represent it. The idea of this improvement is to directly use the mesh to define the real surface. This is made by the assumption the real surface is somewhere below the wall. In this first approach, we define this real surface at the first layer of nodes below the wall in the solid phase with the LBM Cartesian mesh. This means the real surface is considered at most 1 lattice from the wall for full-way bounce-back and 0.5 lattice for half-way bounce-back.

To smooth the orientation of the interface at the wall surface and take into account the flow conditions, we need to interpolate between the real surface and the closest nodes in the domain to define the approximate normal of the interface at the wall nodes. At this interpolation step, different choices can be done. We implemented a linear interpolation and a linear least-square interpolation. The linear least-square can recover the linear interpolation in case of using only two nodes (one for the real surface and one for the fluid nodes) for the interpolation. Therefore, only the linear least-square method will be used.

As a quick reminder of the linear least-square method described in 3.3.5.3, we base the least-square method on the signed distance (positive for the fluid nodes and negative for the solid nodes). Therefore, the method is restricted to seek the normal when the distance is null at the boundary i.e. the y-intercept of a linear regression. All the loops are vectorised, and the nodes are marked in the pre-processing part. Thus, the calculation time is similar to the linear interpolation.

Node selection

The drawback of this method is the selection of nodes for interpolation. Let us define a case as in Figure 5.1.

The smooth approach is applied to the wall nodes (red). For each wall node, we associate N_f number of fluid nodes (blue) and N_s number of first solid layer nodes (cyan). To select the fluid nodes, we first take the closest fluid node by using the normal of the wall then we travel around this node. Finally, we sort the nodes found by the distance from the wall node and we conserve only the N_f number of the closest nodes. For the first layer nodes, we travel on the wall and select the node at the

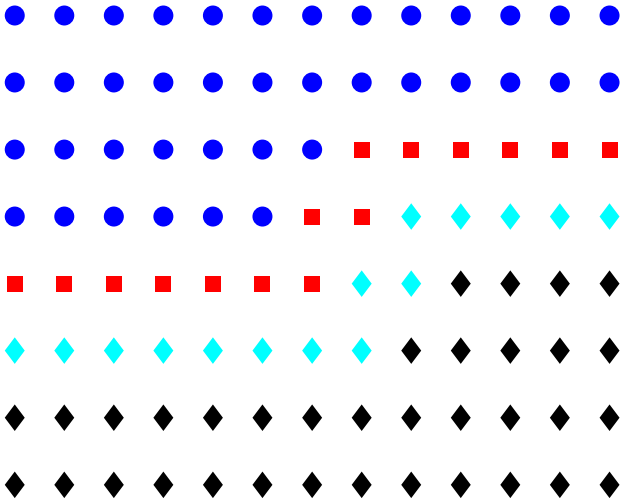

Figure 5.1: Node representation for the smooth approach. The blue, red, cyan and black points are the fluid, wall, first layer in solid and solid nodes, respectively.

opposite direction of the normal then we sort the nodes by distance and we conserve only the N_s number of the closest nodes.

This step is done in the pre-treatment. Therefore, this method has a comparable CPU cost with the standard approach.

5.2.3 Incorporated in Colour Fluid model

These two approaches (the standard or smooth treatment) can be used for different multiphase simulation methods including VOF and Level-Set. In this chapter, only the colour-fluid LBM model will be used.

The colour-fluid model can be used with different perturbation operators as seen in subsubsection 3.3.4.1. The contact angle modifies the normal of the interface, in the CSF model, the normal is directly used. So, no special treatment is needed. For the other model, the colour gradient is directly used. Therefore, the contact angle treatment modifies the components of the colour gradient but keeps the colour gradient norm. Thus, the colour gradient is aligned with the normal.

The contact angle also modifies the recolouring step but without any special treatment due to the recolouring from Latva-Kokko *et al* [5].

Other techniques exist such as the modification of the density on the wall [4] but this

model considers the slip condition of the interface and models the balance of force between shear force, interface force and fluid-structure interaction on the surface by the Young-Dupré's law (Equation 5.1).

5.3 Validation cases

Dealing with contact angle causes numerical problems. Therefore, the method needs to be validated and analysed. Three cases are used: the standard validation on static droplets, inclined channels and serpentine.

5.3.1 Static droplets

Two main kinds of static droplets are tested: a droplet on a wall which can be aligned or not aligned with the lattice and a droplet on a circle. For those cases, a mesh size of $400^2[lu]$, a coefficient β (recolouring operator) of 0.99 and a droplet radius of 50 lattices are used. The fluids are considered to have the same kinematic viscosity of $1/36[lu]$ and a surface tension of $0.001[lu]$ to keep a low mean free path and a low disturbance from the source term. For instance, those parameters correspond to a droplet formation in ink-jet printing [152] where the Ohnesorge number varies from 0.02 to 1.5 in this article (equivalent to a Laplace number of 129).

Flat and inclined walls

The first validation of this new approach is carried out with the flat and inclined walls. We expect to get the same result with these walls. An example of a droplet on a wall is shown in Figure 5.2 where the red fluid is the droplet and the blue fluid is the surrounding fluid. The improvement of the method can be clearly seen compared with the standard approach. The contact angle does not affect in the same manner the results. In Figure 5.3, the smooth treatment removes the spreading on the surface as commonly seen in LBM when the surface is not aligned with the lattice [151] and keeps wetting the wall for a quite large contact angle.

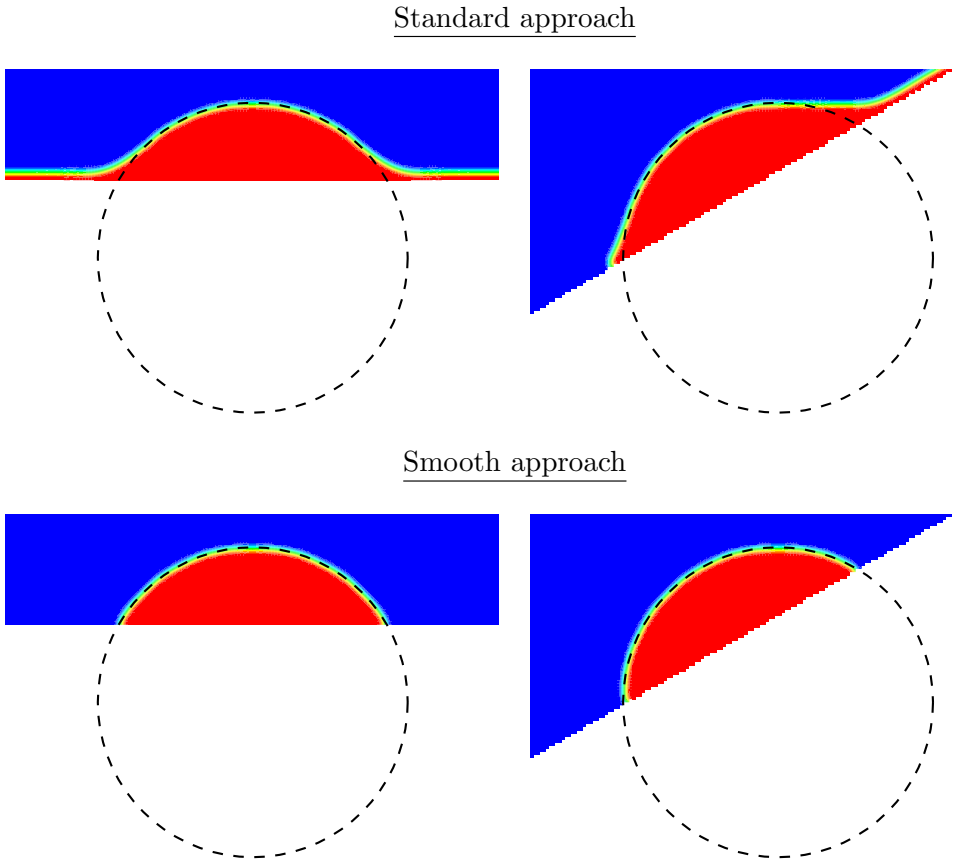

Figure 5.2: Static droplet on flat and inclined walls. the circle represents the theoretical interface and the white part under the droplet is solid.

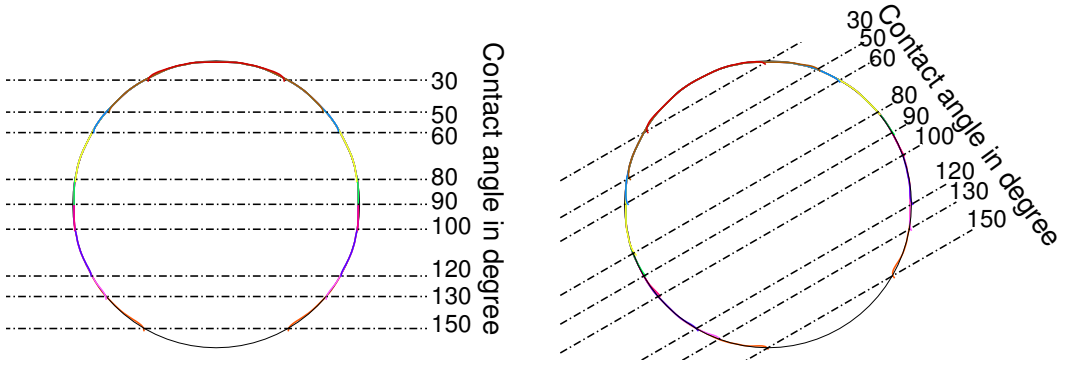

Figure 5.3: Profiles of the static droplets on a surface with the smooth approach. Each colour represents a contact angle, i.e. blue, yellow, green for $60°, 80°$,and$90°$, respectively.

Moreover, non-symmetrical droplet was not observed in the static case, which can be seen with the standard approach in Figure 5.4. In the dynamic case, the droplet can be non-symmetrical due to the balance of force among the interface forces and the shear stress, roughness, chemical reactions, etc.

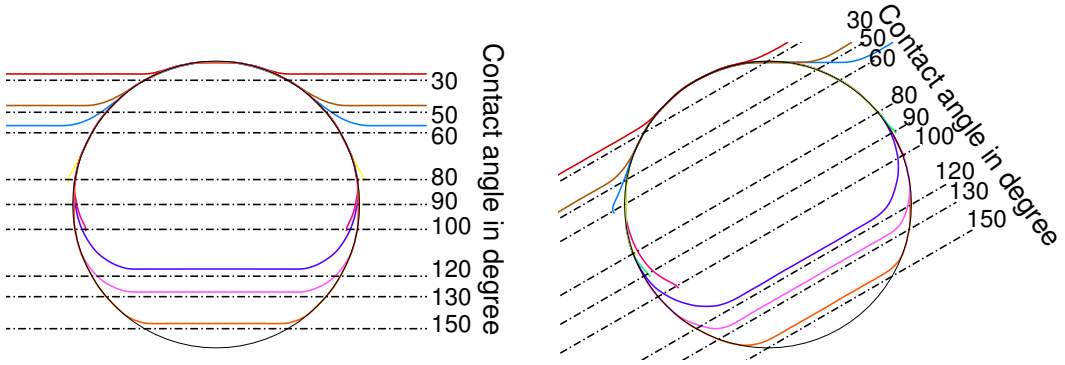

Figure 5.4: Profiles of the static droplets on a surface with the standard approach. Each colour represents a contact angle, i.e. blue, yellow, green for $60°, 80°$,and$90°$, respectively.

With this approach, the droplet does not spread on the surface as commonly seen in LBM when the surface is not aligned with the lattice [151]. It is similar results obtained by a similar method used by Leclaire in [151]. However, he defined his real surface by nodes regularly placed on an equation line i.e. the ideal scenario for the interpolation.

Curved boundaries

The flat and inclined walls are quite simple even if is still challenging to obtain accurate results. The curved boundary is more difficult, and the test case is defined as a circle with the same diameter than the droplet. In Figure 5.5, it can be clearly seen the improvement of the method. However, this new approach is not perfect for 80° because that interpolation technique has difficulties to give a null value. For a contact angle close to 90° one of the two components of the normal vector of the interface is close to 0.

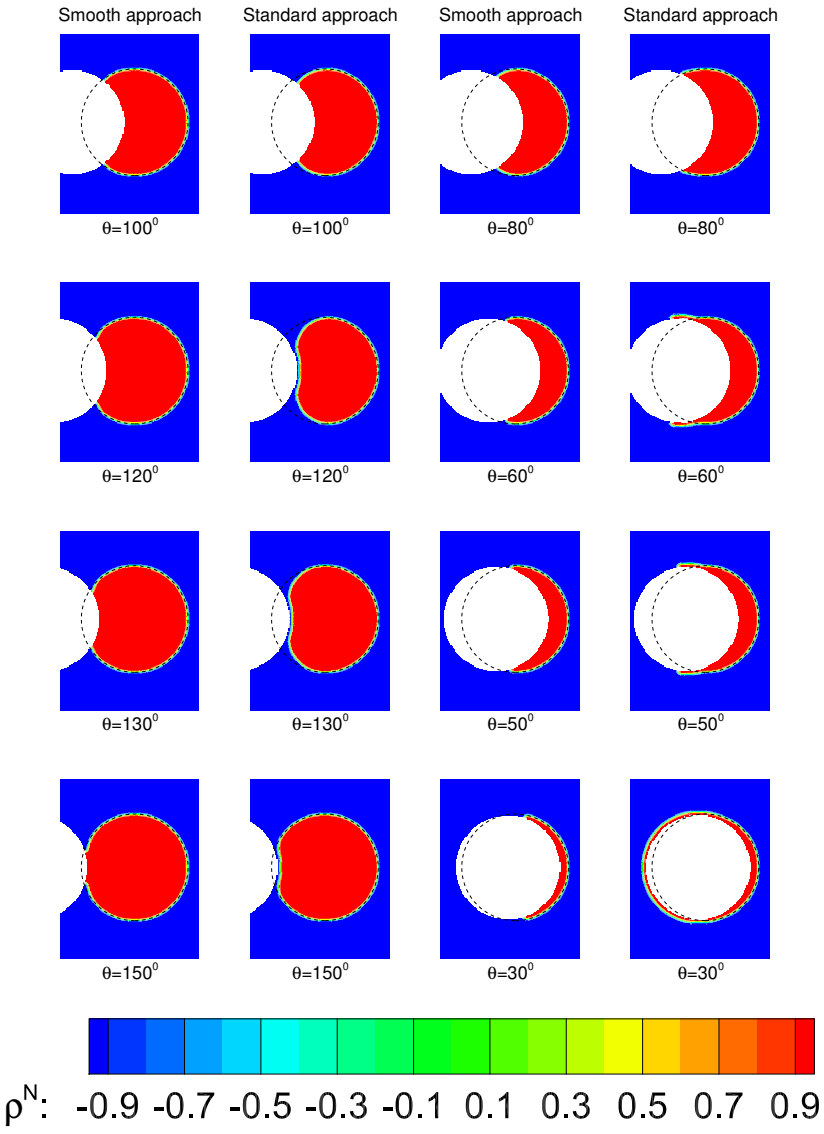

Figure 5.5: Comparison of static droplets on a curved boundary

5.3.2 Inclined channels

This simple geometry, seen in Figure 4.15, is created to analyse how an interface moving inside a channel with flat and inclined walls behaves with this new approach. The mesh size of 19 lattices for the channel height, and it was validated for a single-phase flow with SEM results as it can be seen in subsection 4.2.3. The same boundary conditions are used i.e. a parabolic velocity profile is imposed at the inlet and a constant pressure (density set to 1) at the outlet with the classical Zou and He boundary condition [83] and the wall treatment proposed in section 4.2 (full-way bounce-back with BGK collision and density extrapolation). Thus, the contact line can be control on the walls without the issue of the half-way bounce-back i.e. estimation of the position of the contact line.

We based the dimensionless number, described in chapter 2, on the height of the channel, the maximum velocity at the inlet, the kinematic viscosity of the red fluid, and a density of 1 [lu].

The smooth approach is compared to the standard approach in Figure 5.6 for a viscosity ratio of 6 (the blue fluid is the highest viscous fluid). The method handles correctly

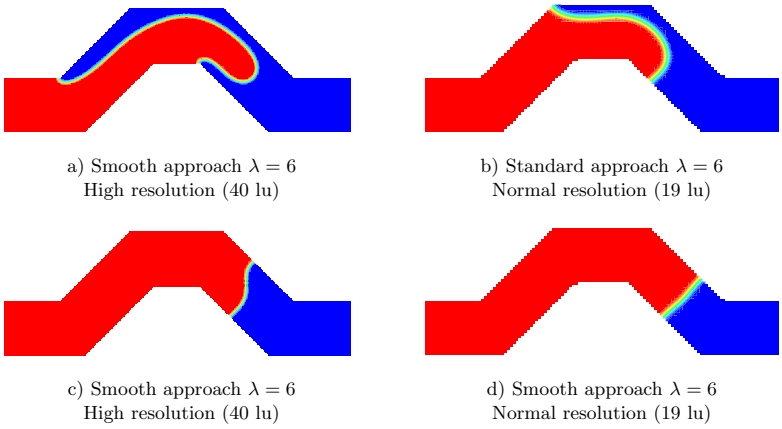

a) Smooth approach $\lambda = 6$
High resolution (40 lu)

b) Standard approach $\lambda = 6$
Normal resolution (19 lu)

c) Smooth approach $\lambda = 6$
High resolution (40 lu)

d) Smooth approach $\lambda = 6$
Normal resolution (19 lu)

Figure 5.6: Validation of the approach in a channel for Re=1, Ca=0.04, and $\theta = 90°$

this kind of complex geometry for this specific flow. However, a deeper investigation has to be done on the effect of the viscosity ratio, capillary number, contact angle and choice of nodes.

Effect of the viscosity ratio

The viscosity of the red fluid is kept constant with a value of $1/36[lu]$. The Reynolds number is kept to 1 to ensure the inertia forces are not prominent compared to the viscous forces. For the first case, the capillary number is quite small ($Ca = 0.04$) thus the interfacial forces are prominent in the domain and the interface stays almost flat with a contact angle of 90°. Due to the low capillary number, the interface is almost not affected by the viscosity ratio as seen in Figure 5.7.

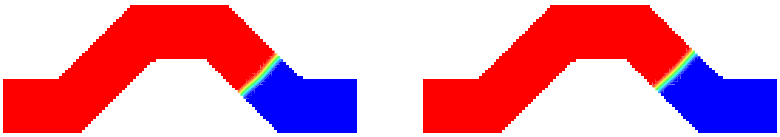

a) Smooth approach $\lambda = 6$ c) Smooth approach $\lambda = 1$

Figure 5.7: Effect of the viscosity ratio in a channel for H=19, Re=1, Ca=0.04, and $\theta = 90°$.

When the inertia forces are less negligible, the non-uniform flow field can change the interface position with the viscosity as represented in Figure 5.8.

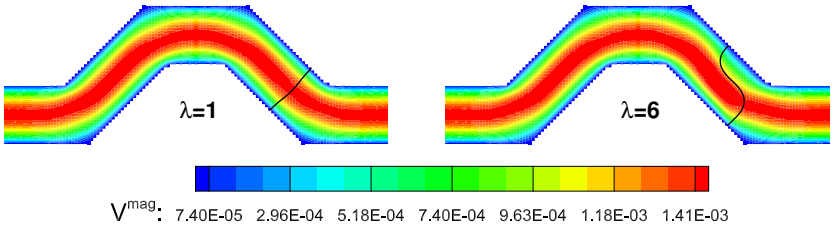

Figure 5.8: Effect of the viscosity ratio in a channel with inertia effect (Re=1, Ca=0.4, and $\theta = 90°$). The black line represents the interface.

Effect of the capillary number

The capillary number affects the displacement of the interface in term of velocity and deformation. It is difficult to predict the behaviour due to the effect is local along the interface. However, it can be seen, in Figure 5.9, the inertial forces become stronger with the increase of the capillary number in the inclined part. Therefore, the correct behaviour of the interface is captured with the smooth approach.

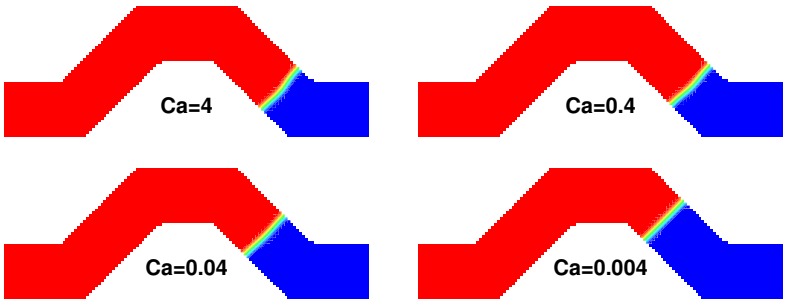

Figure 5.9: Effect of the capillary number in a channel for $\lambda = 1$, Re=1, and $\theta = 90°$.

Effect of the contact angle

The inclined channel creates problems to get the correct contact angle as it can be seen in Figures 5.4 and 5.6. The smooth approach works well on the static droplets (Figure 5.3) but in dynamic cases, the contact angle changes due to the shear forces. As it can be seen in Figure 5.10, the smooth approach handles the flow well on inclined walls. The low grid resolution, needed to be able to simulate large simulation domains for reservoir applications, creates some pinches of the interface but without altering the physical behaviour. It can be noticed the capillary number needs to be higher for the contact angle 150° due to the capillary pressure.

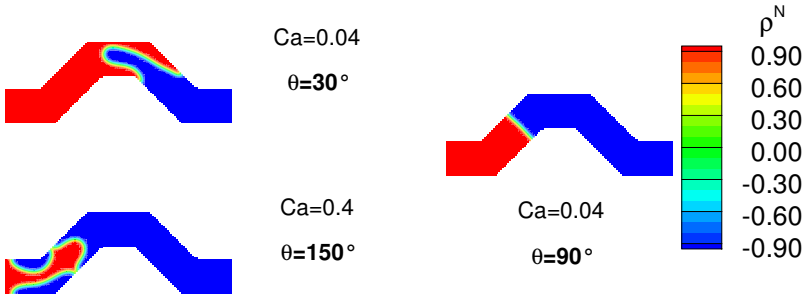

Figure 5.10: Effect of the contact angle in a channel for $\lambda = 1$ and Re=1.

Node selection

The main issue of the smooth approach comes from the node selection (Figure 5.1) which can affect the results. The selection is explained in subsection 5.2.2. For a contact angle of 90°, the solid node selection does not affect greatly the results as it can see in

Figure 5.11. The fluid nodes can have a modest influence with a large number of fluid nodes. From this first test, it can be sufficient to limit the number of fluid nodes to a maximum of the 3 closest nodes.

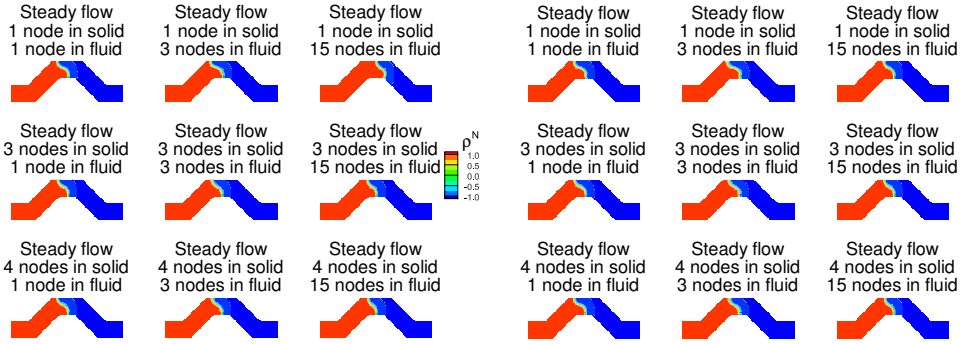

Figure 5.11: Node Selection for 90° contact angle, viscosity ratio 1 and $Ca = 0.4$ and 4 on the left and right, respectively.

When the wetting fluid is the incoming (red fluid), the choice of node affects more the results as in Figure 5.12. Using 4 solid nodes is not a good idea due to the non-symmetrical selection and using more is not a solution due to the theoretical contact angle will be far from the contact angle set-up. Indeed, on a flat surface, using an even number brings a non-symmetrical selection, thus, the contact angle will be anisotropy i.e. an interface moving on a flat wall will be differently influenced if the interface is before or after a node. This will change the contact angle even for a constant flow condition and a perfect flat surface. Moreover, using a lot of node could give wrong results due to the colour gradient is close to 0, so, the estimate contact angle would be far from reality. A second interface can also influence it. Thus, the theoretical contact angle would not be correctly estimated.

When the wetting fluid is the outgoing (blue fluid), unsteady phenomena of the contact line can appear. In Figure 5.13 on the left, the unsteady behaviour was not expecting for this case due to the Reynolds number is 1, the capillary number is not so low or high, and the viscosity ratio is 1. Therefore, the selection of nodes can generate spurious unsteady phenomena.

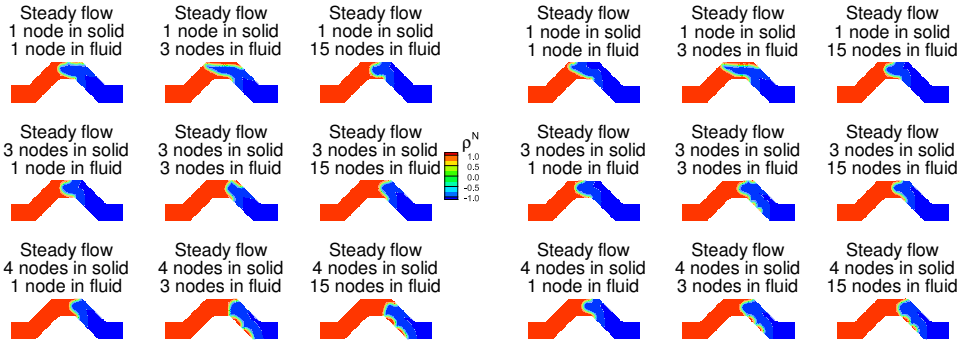

Figure 5.12: Node Selection for 30° contact angle, $Ca = 0.4$ on the left and $Ca = 4$ on the right and viscosity ratio 1

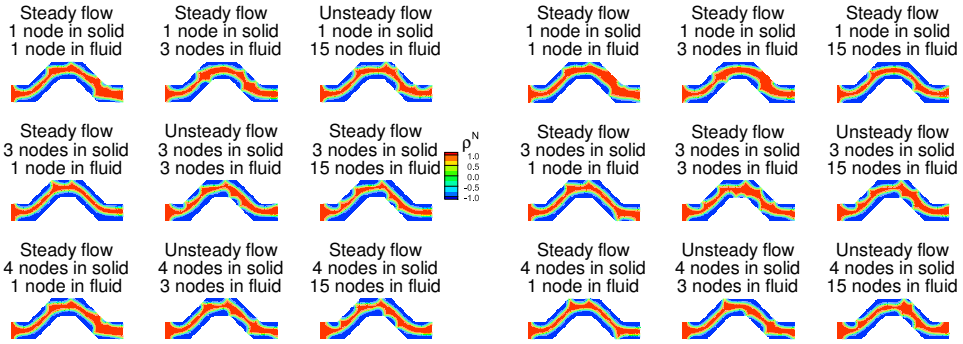

Figure 5.13: Node Selection for 150° contact angle, $Ca = 0.4$ on the left and $Ca = 4$ on the right and viscosity ratio 1

5.3.3 Serpentine

The serpentine represents a non-straight channel with a constant height (H). The radius (R) of curvatures at the central line is 1.25 H and the length is 10 R. Without external forces such as gravity, magnetic field, etc. and with a Reynold number less or equal to 1, the velocity profile is parabolic due to the well-known Poiseuille flow. Therefore, an interface moving inside should be affected by the parabolic velocity profile and the capillary number at the interface as for a straight channel and locally, the curvature of the wall will also modify the interface shape.

The Reynolds, the capillary number, and the viscosity ratio are defined by the same way than before for the straight channels.

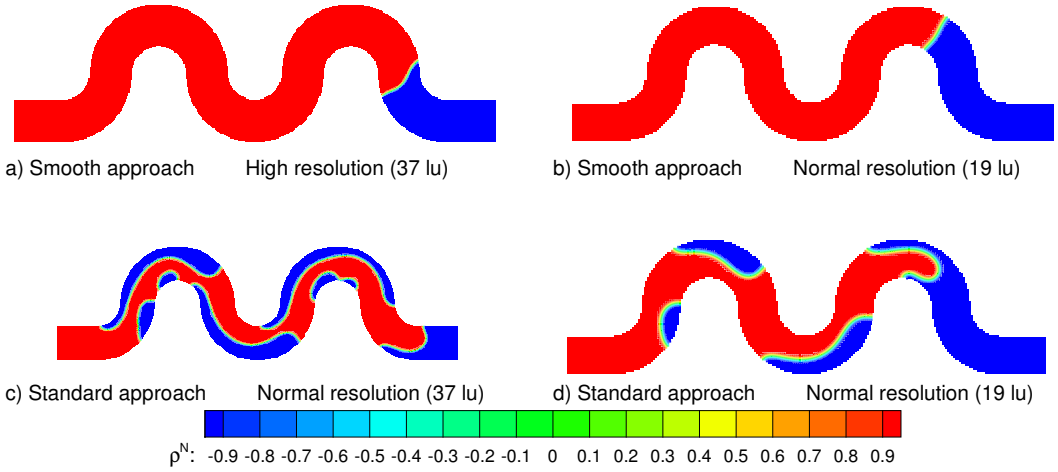

Figure 5.14: Validation of the approach for Re=1, Ca=0.04 and λ=6.

Clearly, as shown in Figure 5.14, the standard approach does not represent correctly the physics due to the low Reynolds and capillary numbers, the interface should not break and stay almost straight with a contact angle of 90°.

Effect of the viscosity ratio

The viscous forces affect the displacement of interfaces by conserving the momentum. As the momentum has to be conserved everywhere, the viscous forces affect the displacement of the interface at any location of the flow field including the triple line which is rarely taken into account. With this smooth contact angle approach, we can simulate

interface displacement on the triple line with the viscous forces and the surface tension force. The viscosity of the red fluid is kept constant.

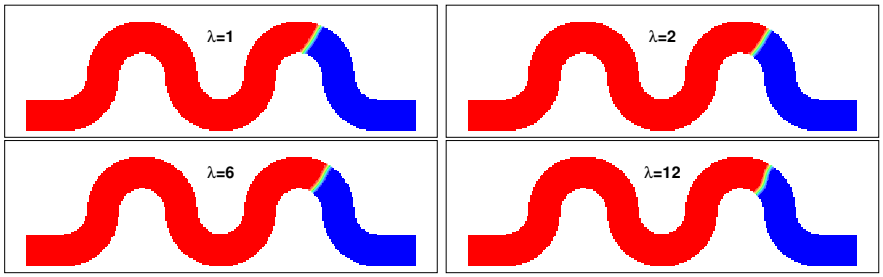

Figure 5.15: Effect of the viscosity ratio on the interface displacement in a serpentine for Re=1, Ca=0.04, and $\theta = 90°$.

As expected, the displacement interface moves almost at the same speed due to the mass flow of the red fluid is the same between the simulations. With the increase of the viscosity of the blue fluid, the interface deforms more due to the curvature of the serpentine as shown in Figure 5.15. Moreover, the pressure gradient is corrected affecting through the interface including the triple line as represented in Figure 5.16.

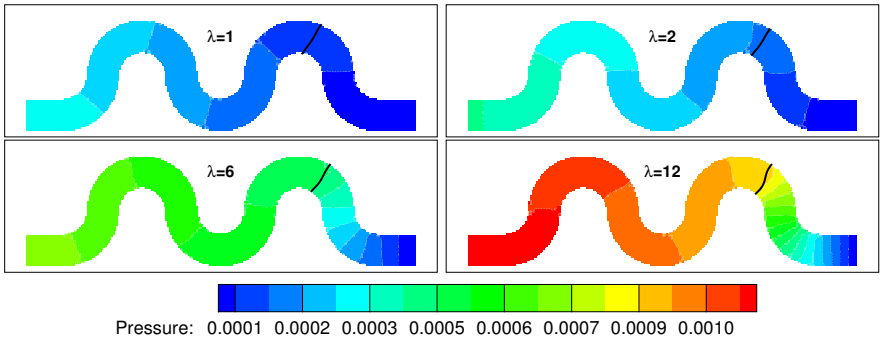

Figure 5.16: Effect of the viscosity ratio on the pressure field in a serpentine for Re=1, Ca=0.04, and $\theta = 90°$.

It can be noticed at this channel size ($19[lu]$), viscous and capillary fingerings do not exist and should not exist. Moreover, the capillary fingerings cannot happen due to the viscosity ratio more than 1. The viscosity ratio is relatively low, then the viscous fingerings for a bigger height are unlucky to happen too [153, 154].

Effect of the capillary number

The capillary number is inversely proportional to the surface tension. When the capillary number is less than 1, the interface forces are stronger than the viscous forces. In other words, the interface does not deform due to the viscous force. For a contact angle of 90°, the interface has to be flat for a capillary number tends to 0. Figure 5.17 shows the expected results.

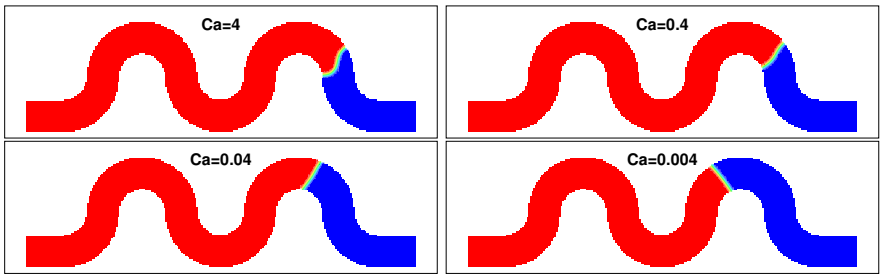

Figure 5.17: Effect of the capillary number in a serpentine for Re=1, $\lambda = 1$, and $\theta = 90°$.

Effect of the contact angle

In case of a curved boundary, it is difficult to define the normal of the surface so the contact angle and also the analysis of the accuracy. However, the serpentine is very close to a straight channel thus, we expect to get similar results than a straight channel with negligible inertia.

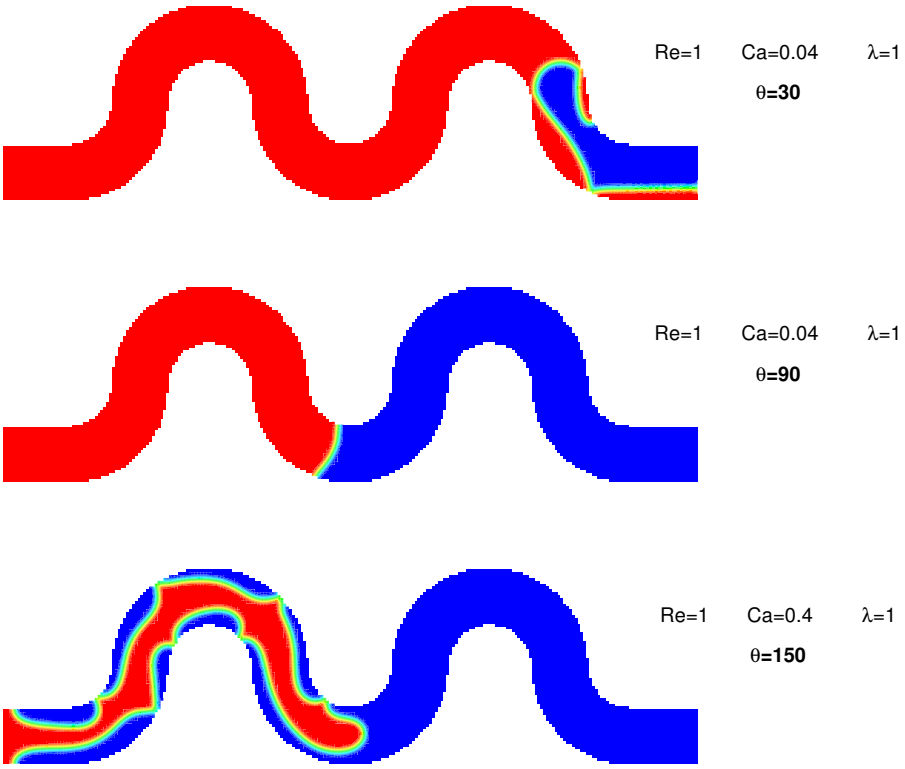

Figure 5.18: Effect of the contact angle in a serpentine.

The results should not be exactly the same as a straight channel because the wall shear stress will be different, and the curvature of the wall will affect the velocity of the contact line. However, the interface position at the centre of the channel should be very similar to a straight channel. We get a very good match (Figure 5.19) and we consider the displacement of the interface as correct even for a low grid resolution.

At a low or large contact angle, the approach does not perform perfectly for a channel height of only 19 lattices as seen in Figure 5.18. The interface is pinched with the wall, but the results become better if we increase the resolution (Figure 5.20).

5.3.4 Discussion

The smooth method shows a strong improvement of the results compared to the standard approach for static droplets and dynamic interface without introducing a sliding wall boundary condition [4]. The acceleration and deceleration of the velocity

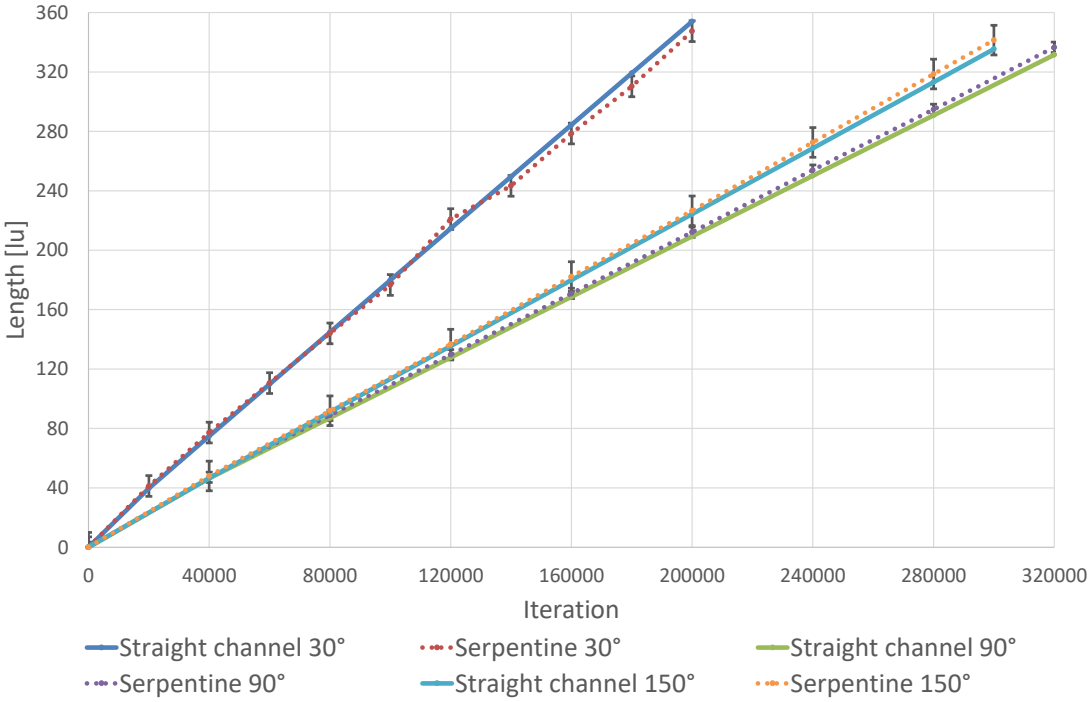

Figure 5.19: Comparison between the serpentine and straight channel. $Re = 1$ for the contact angles of 90° and 30° and $Re = 10$ for the contact angle of 150°.

of the contact line are captured with this new approach, however further validation is needed to confirm the results quantitatively. As the serpentine is a channel with a constant height, we have compared the results between the serpentine and the straight channel. To reduce the effect of the curvature of the channel on the flow field, the Reynolds number is fixed at 1. The inertia affects also the capillary number, so the capillary number is kept less than 1 but more than 10^{-3} to avoid a capillary fingering. A good agreement was found and represented in Figure 5.19. The most useful part of this method is to be able to handle complex geometry with poor resolution but keeps the essence of the physics which is important to enable pore-scale simulations for REV samples.

5.4 Berea sandstones

This Figure 5.22 represents a sample of Berea sandstones [6] and is read directly by the code and an evaluation for each node is done to determine the solid or fluid nodes. After this step, several methods add the walls and corners to the domain and remove

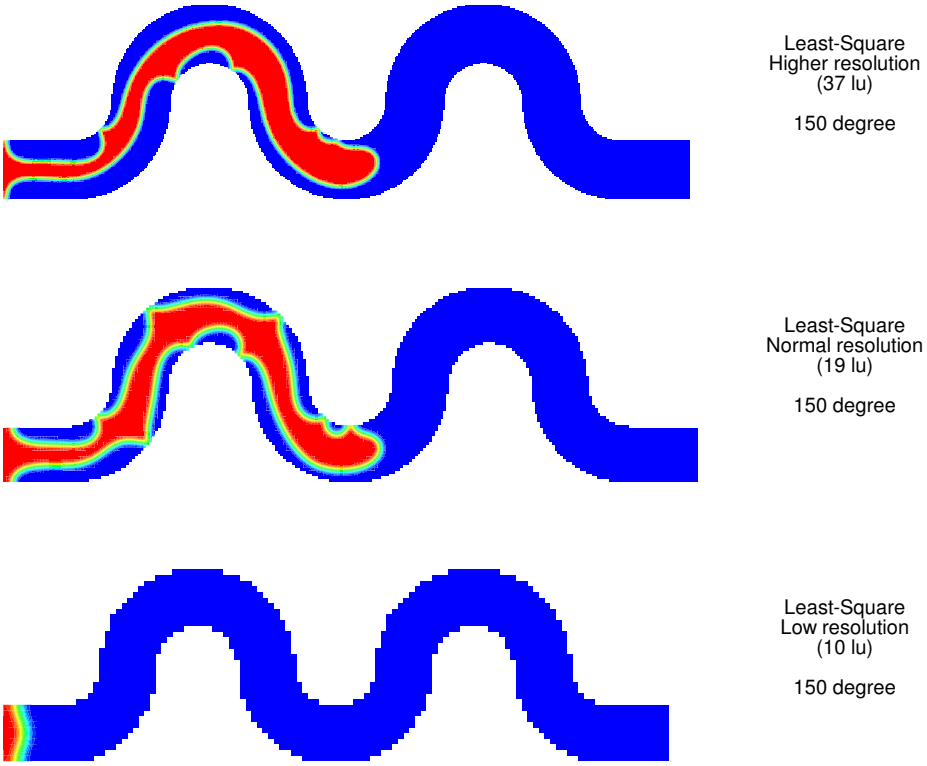

Figure 5.20: Effect of the grid resolution in a serpentine for $Re = 1$, $Ca = 0.4$ and $\lambda = 6$.

the incorrect solid nodes. To detect the walls and the concave and convex corners, we detect the kind of node (fluid or solid) connected to all solid nodes and we define the direct and diagonal connections to a solid node. A direct connection is the first node in ± x or ± y direction. A diagonal connection is the first node in ± x and ± y directions. The wall boundary conditions are detected as 3 solid direct connections, the concave corners as 4 solid direct connections, and the convex corners as 2 solid direct connections and 1 solid diagonal connection. A sketch is shown in Figure 5.21. The code automatically removes the solid nodes (not physical and also cannot be computed) connected to: no other solid node, the walls without thickness (one layer of solid nodes), two concave corners at the same node, and the solid nodes connected to only one solid node. In addition, the code is parallel through an MPI approach and including I/O and pre-treatment. Another example of simulation is given in Appendix B.

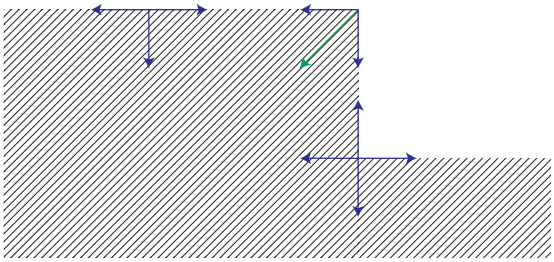

Figure 5.21: Detection of walls and corners; The solid direct connections in black blue arrows and the solid diagonal connection in green arrow.

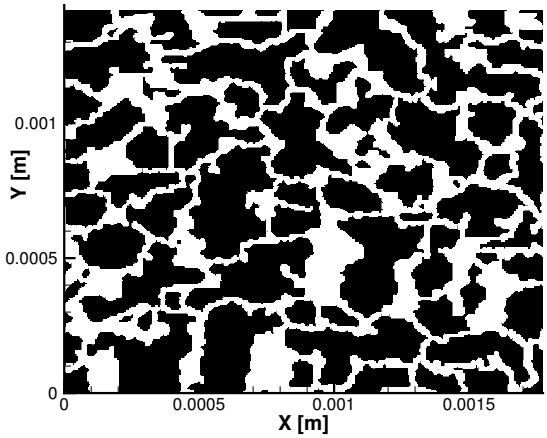

Figure 5.22: Berea sandstones representation after imaging treatments.

The sample has a porosity of 0.333634, a length of 1774$[\mu m]$, a height of 1418$[\mu m]$ and a depth of 24.54$[\mu m]$. The size of the 2D simulation is 1323$[lu]$ by 1059$[lu]$. A pressure difference of 0.2/3$[lu]$ is imposed using Zou and He boundary condition [83]. The wall is treated with the "New Technique" described in section 4.2 (full-way bounce-back) and the contact angle with the smooth approach. The intrinsic permeability is 4.875$[lu]$ so 8881mD. The 2D approach cannot be compared with the experimental results [6] due to the depth is not taken into account.

The viscosity ratio is defined in subsection 2.1.2 and the dynamic viscosity of the displaced fluid is kept constant at 0.125$[lu]$. For all simulations, the domain is initialised with a linear pressure drop, a density at the outlet set to 1, and the velocity equals to 0. In two-phase flow simulations, the porous media is saturated by the invading fluid for the 20 first lattices in the x-direction and the rest of the media is saturated with the displaced fluid. This initialisation is used to avoid non-physical phenomena due to the boundary conditions. Indeed, the normal of interface can be wrongly calculated at the boundary condition.

A representation of the two-phase flow in the Berea sandstones is shown in Figure 5.23 where the blue fluid is the invading fluid and the red fluid is the displaced fluid. In case of imbibition, the contact angle is less than 90°, so the blue fluid is defined as the wetting fluid. For drainage, the contact angle is more than 90°. In Figure 5.23, it can be noticed a lot of capillary trapping for a low contact angle.

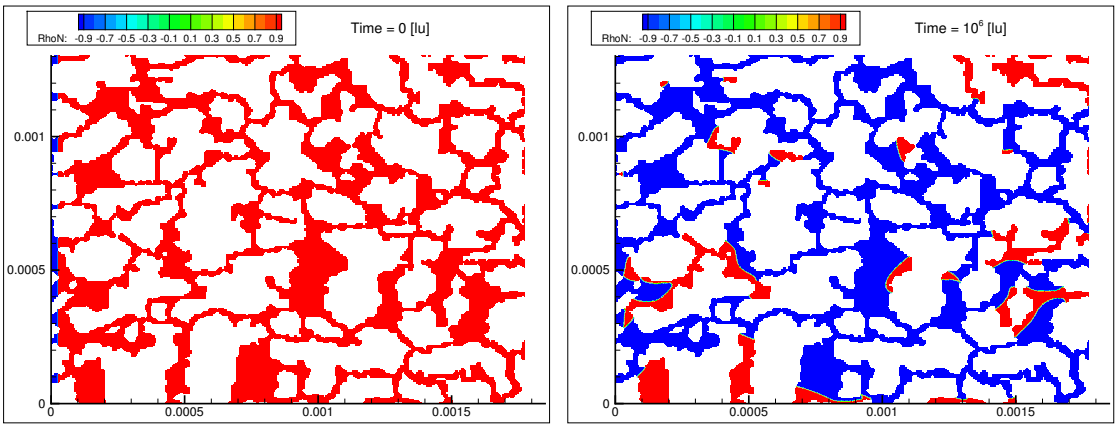

Figure 5.23: Two-phases flow in Berea sandstones with $\lambda = 2$, $\theta = 45°$, $\sigma = 0.001[lu]$ and $\Delta p = 0.2/3[lu]$.

In the next two sections, the surface tension is set to $0.001[lu]$ to keep the magnitude of spurious current negligible in comparison with the flow field. To investigate the effect of the smooth approach on the Berea sandstones, the mobility, mobility ratio and capillary number are based on the integration of velocity magnitude, and magnitude of pressure drop over the domain and described in section 2.2. The average velocity magnitude is scaled to the volume of the sample with the porosity. This means the results are the maximum we could get, and they are not directional. Therefore, those values can be difficult to compare to experimental data, but they are closer to the values that are used in up-scaling methods for reservoir simulations [18, 155]. Indeed, up-scaling methods replace each REV by a volume, thus, the volume averaging is more suitable.

5.4.1 Effect of the viscosity ratio

The viscosity ratio affects the permeability at the steady state but also the flow fluctuation, unsteady behaviour due to the evolution of the gradient of pressure and/or mass flow for a reservoir, or the evolution to towards the steady state which is mostly neglected in single-phase flow through a porous media. Indeed, the inertia effect cannot be negligible due to the Forchheimer effect [156] when the mass flow rate starts to be important or when the flow is developing inside the porous media.

Firstly, the impact of the viscosity ratio is seen in Figure 5.24 by removing the contact angle. This is done by using the same approach than inside the domain on the walls and corners. Thus, the normal of the interface at the walls or corners is approximated by the colour gradient. Physically, this represents an interface sliding on a wall with an equilibrium of forces between Solid-Invading and Solid-Displaced. We call this contact angle as "free". As expected the mobility ratio increases with the viscosity ratio. As it can be seen in Figure 5.24, the mobility ratio is 15% higher than the viscosity ratio of 2 at the steady state which means the relative permeability of the invading fluid is 15% greater than the displaced fluid.

By increasing the viscosity ratio to 5, the displaced fluid has its mobility reduced to the same as injecting water in a media filled with silicon oil or honey. The mobility ratio is 20% less than the viscosity ratio. Thus, the invading fluid needs to sneak.

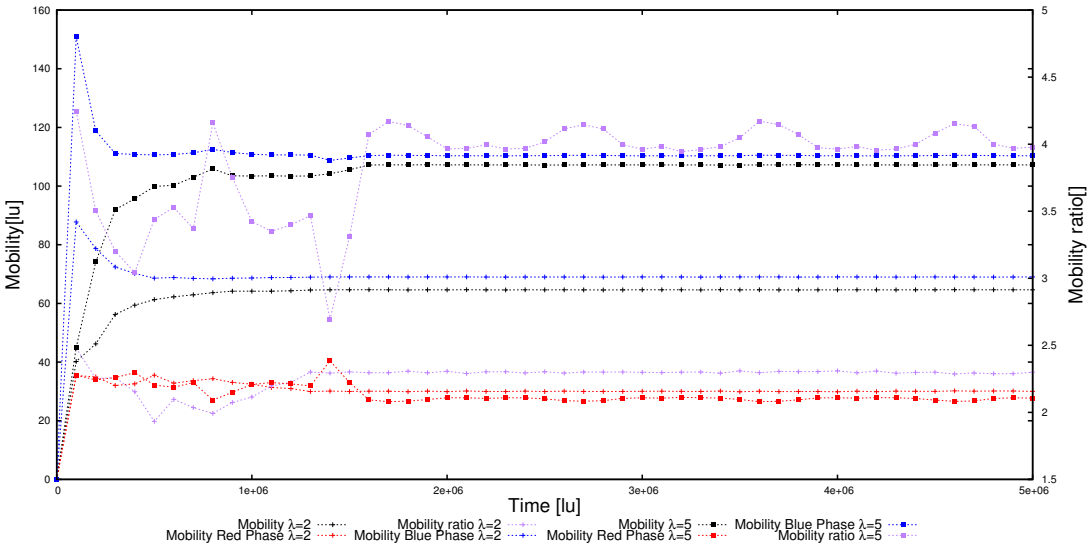

Figure 5.24: Time evolution of the mobility ratio and the capillary number with free contact angle for Berea sandstones.

When the Reynold number and the capillary number are low enough, the interface moved at $\theta = 90°$ in a channel with a free contact angle approach as explained above. Figure 5.25 represents the same case as Figure 5.24 but with a defined contact angle of 90°. There is no major difference between the two cases. The viscosity ratio has a slightly more effect for $\lambda = 5$, i.e. the mobility ratio is $\approx 28\%$ less than the viscosity ratio.

If the displaced fluid is assigned as the wetting fluid, i.e. the drainage case seen in Figure 5.26, the viscosity ratio plays an important role compared to the $\theta = 90°$ case. The mobility of the displaced fluid is a little less affected by the mobility ratio. However, the invading fluid shows a strong influence. In oil recovery, the production of oil will be lower.

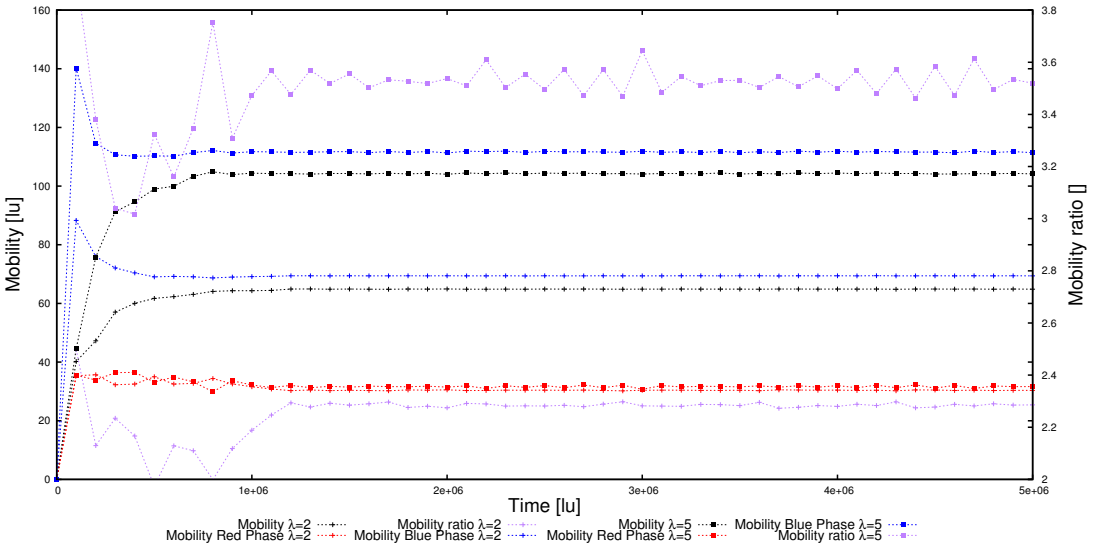

Figure 5.25: Time evolution of the mobility ratio and the capillary number with $\theta = 90°$ for Berea sandstones.

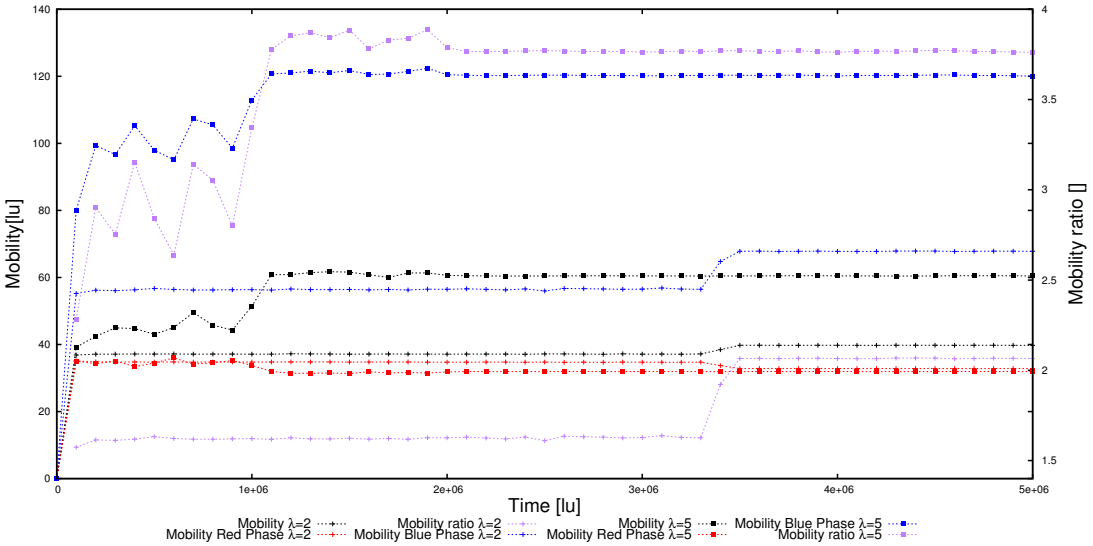

Figure 5.26: Time evolution of the mobility ratio and the capillary number with $\theta = 170°$ for Berea sandstones.

In Figure 5.27, the displaced fluid is drained outside. The mobility ratio is greatly increased compared with the previous cases, so the viscosity ratio has an important impact on the mobility of the displaced fluid.

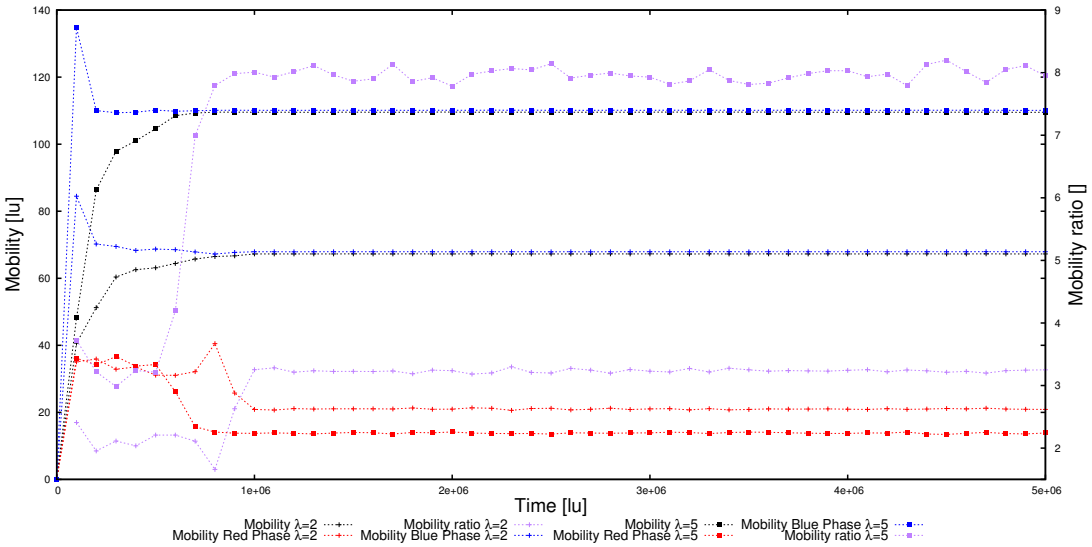

Figure 5.27: Time evolution of the mobility ratio and the capillary number with $\theta = 10°$ for Berea sandstones

5.4.2 Effect of the contact angle

Previously, we have seen the viscosity ratio plays a significant role and we have noticed that the contact angle modified greatly the flow inside the Berea sandstones. However, the viscosity ratio is fixed at each simulation, but the apparent contact angle changes with the capillary number.

When the viscosity ratio is 2, the mobility ratio is similar for a contact angle of 45°, 90° or "free". For a contact angle of 10° or 170°, a significant effect is noticed and represented in Figure 5.28.

It can be deduced that the wall shear forces affect more than the interfacial forces. In other words, the contact angle is closer to the orientation of the interface rather the equilibrium contact angle. However, the capillary number is always affected by the contact angle. Thus, the similar results for the mobility ratio come from the curvature of the interface is around 0 for the contact angles: "free", 90° and 45°.

When the viscosity ratio increases to 5 and shown in Figure 5.29, significant effects are observed. First, the smooth approach does not perform well for a contact angle of 170°. The mesh needs to be increased to represent correctly the fingers inside the sample as it was shown in the serpentine case.

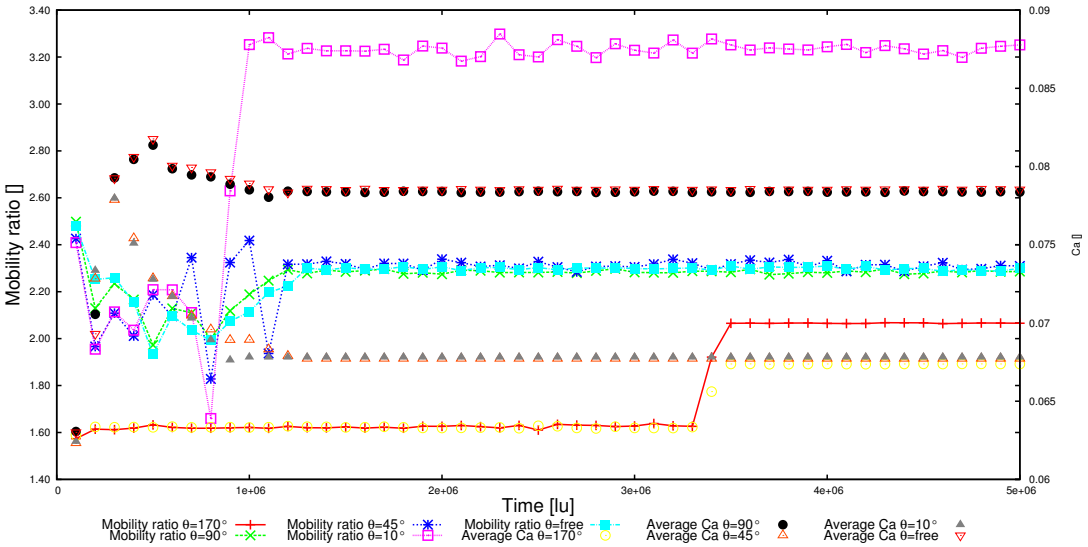

Figure 5.28: Time evolution of the mobility ratio and the capillary number with $\lambda = 2$ for Berea sandstones.

Second, for a contact angle of 90°, the mobility ratio is lower than a "free" contact angle due to the wall shear forces. By decreasing the contact angle, the mobility ratio is clearly increasing. Using Figures 5.27 and 5.25, it can be deduced this comes from the relative permeability of the displaced fluid is decreasing. It can be noticed for a contact angle of 45°, the mobility ratio is less than the viscosity ratio. Therefore, the displaced fluid has the highest relative permeability.

The capillary number is also clearly affected by the contact angles. For a 90° contact angle, the capillary number is the highest which means the shear forces contribute to the capillary number. This is confirmed by the capillary number at the contact angle of 170°.

5.4.3 Effect of the surface tension

The surface tension affects directly the capillary number and as we have seen it plays a significant role in the Berea sandstones. To complete this study, we compared 3 different surface tensions at a relatively low viscosity ratio, 2, and a contact angle of 90°.

We can see in Figure 5.30, the capillary number increases by one order with a decrease

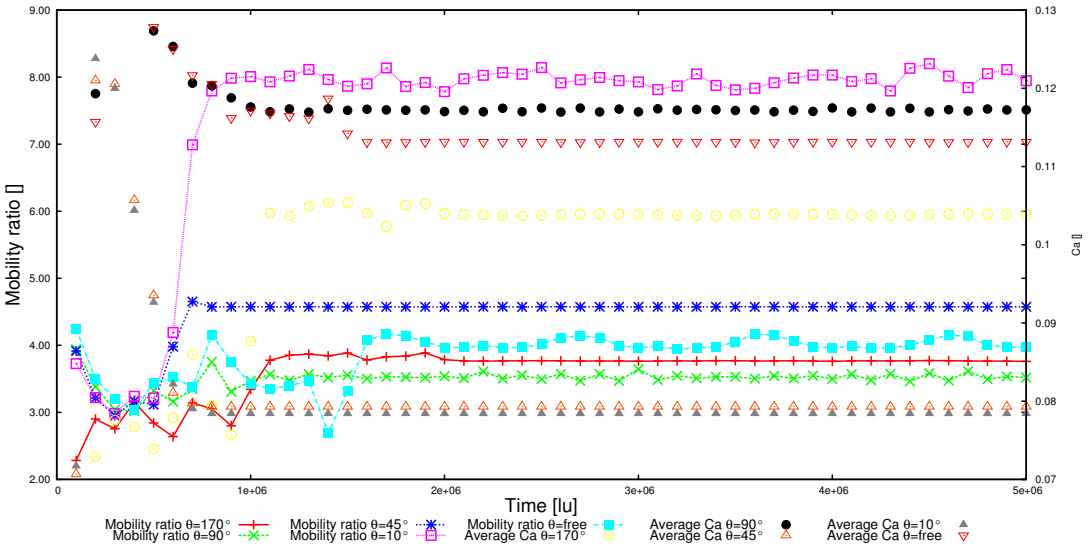

Figure 5.29: Time evolution of the mobility ratio and the capillary number with $\lambda = 5$ for Berea sandstones.

of one order of the surface tension. Therefore, the inertia forces stay constant and the changes of the mobility ratio are directly linked with the interfacial forces. Imposing a surface tension of $0.01[lu]$ creates too high spurious current and gives noisy results.

5.4.4 Discussion

We have seen the smooth approach can be used to analyse the flow inside a Berea sandstone sample. We have shown the capillary number can be used to characterise the two-phase flows, but it is affected by the contact angle and the viscosity ratio.

For a low viscosity ratio of 2, the mobility ratio is similar for a contact angle of 45°, 90° and with a "free" approach. When the viscosity ratio increases to 5, the mobility ratio becomes more dependent on the contact angle and also on the mesh size for the high drainage case that was shown for a contact angle of 170°.

The capillary number obtained from the simulations for a range of 0.003 to 1. In reservoir simulations, the capillary number usually varies from 10^{-11} to 10^{-5} [155]. Therefore, our simulations need a smaller capillary to be more realistic for reservoirs simulations.

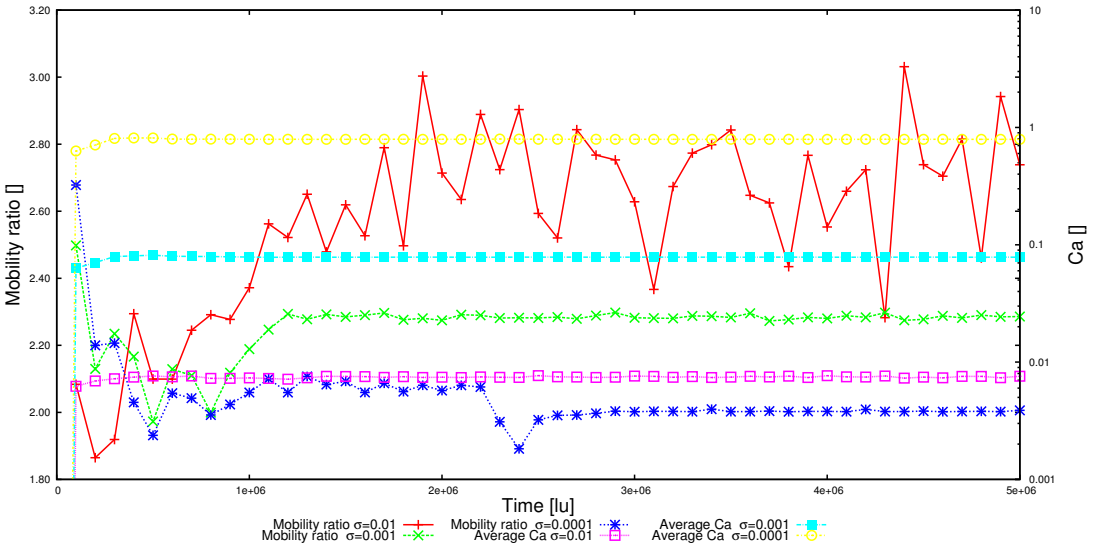

Figure 5.30: Time evolution of the mobility ratio and the capillary number with $\lambda = 2$ and $\theta = 90°$ for Berea sandstones.

Table 5.1 summarizes the results obtained for steady states from our simulations. The intrinsic permeability, used to calculate the relative permeability, is calculated with a single-phase flow with the same pressure drop than the two-phase flow and the viscosity of the displaced fluid is kept constant for all simulations. This assumption is done to keep a reference permeability constant. Indeed, the viscosity is linked with the Knudsen number from the kinetic theory. Therefore, the permeability changes with the viscosity. The variable S represents the saturation and described in subsection 2.2.6.

Table 5.1 shows the viscosity ratio reduces the relative permeability of the invading fluid which represents a reduction of the production rate of the displaced fluid. The relative permeability of the displaced fluid drops with decreasing the contact angle due to the saturation of the displaced fluid drops. However, it stays almost constant for contact angle more than 90°. The mobility is also affected as the viscosity of the fluids is constant in the domain.

The saturation of the invading fluid and the mobility ratio increase when the contact angle decreases. Therefore, the oil recovery will become more difficult when the saturation of the oil becomes low. We observed when the viscosity ratio increases, the capillary decreases. For high viscosity ratio, the interfacial forces will only play a role

λ	2				
Contact angle in degree	free	90	45	10	170
$K_{r,displaced}$	0.80	0.81	0.79	0.56	0.88
$K_{r,invading}$	0.92	0.93	0.91	0.91	0.91
$M_{displaced}$	30.05	38.38	29.48	21.00	32.83
$M_{invading}$	69.01	69.41	68.02	67.92	67.82
M_{ratio}	2.30	2.28	2.31	3.23	2.07
Ca	0.079	0.078	0.068	0.068	0.067
$S_{invading}$	0.575	0.577	0.810	0.812	0.093

λ	5				
Contact angle in degree	free	90	45	10	170
$K_{r,displaced}$	0.73	0.85	0.64	0.37	0.85
$K_{r,invading}$	0.59	0.60	0.59	0.59	0.64
$M_{displaced}$	27.49	31.65	24.07	13.76	31.93
$M_{invading}$	110.37	111.64	110.10	110.12	120.25
M_{ratio}	4.02	3.53	4.57	8.00	3.77
Ca	0.113	0.117	0.079	0.078	0.104
$S_{invading}$	0.666	0.622	0.851	0.856	0.137

Table 5.1: The Berea sandstone sample: the steady state results for $\sigma = 0.001$ and the intrinsic permeability of $4.875[lu]$.

in the transition when the flow starts to develop.

5.5 Chapter summary

The smooth treatment has improved the representation of the interface on complex geometries compared to a standard approach. The non-physical behaviours, commonly seen in literature, were almost completely removed. The contact line behaviour was correctly captured on inclined channels and a serpentine. A good agreement was found between the serpentine and a straight channel for a Reynold number of 1 and a capillary number between 1 to 10^{-3}.

The smooth treatment is applied to a Berea sandstone sample. The capillary number can characterise the two-phase flows. However, it is affected by the viscosity ratio and the contact angle. For a low viscosity ratio ($\lambda = 2$), the mobility ratio is relatively not affected by the contact angle of 45° or 90°. For a higher viscosity ratio ($\lambda = 5$), the mobility ratio becomes more dependant of the contact angle but also of the grid resolution. Our results have a capillary number between 0.003 to 1 and in reservoir simulations, the capillary number varies from 10^{-11} to 10^{-5}. Therefore, our simulations need a smaller capillary to be more realistic for reservoirs simulations which is difficult to obtain (spurious current, high capillary pressure, and extreme slow flow).
The relative permeability of the displaced fluid drops with decreasing contact angle due to the saturation of the displaced fluid drops. However, it stays almost constant for contact angle more than 90°. The saturation of the invading fluid and the mobility ratio increase when the contact angle decreases. Therefore, the oil recovery will become more difficult when the saturation of the oil becomes low. We observed when the viscosity ratio increases, the capillary decreases. For high viscosity ratio, the interfacial forces will only play a role in the transition when the flow starts to develop.

Chapter 6

Conclusion

A review of the most used methods to simulate multiphase flows was presented. LBM used in this thesis was described in more details, especially the colour fluid model. LBGK limits the minimum relaxation time for numerical stability and the maximum is limited by the Knudsen number (rarefaction). The classical scheme used for LBGK employed here is an explicit march in time. Therefore, the time step is limited, and the calculation can be very costly. The colour-fluid model used in this thesis have mainly limitation due to the recolouring operator and the anisotropic properties of the colour gradient.
A validation case is shown on the droplet deformation. We consider we got a good agreement with the analytical. This case has been chosen for his complicated physics due to the deformation comes from the shear stress.

We have validated the single-phase solver on a 2D Driven cavity, the new platform performs well for a relativity high number of cores and is accurate for a large range of Reynolds numbers from 100 to 3200. The implementation of the boundary conditions employed (bounce back, Zou and He and Ho) for the simulations have been considered as validating.
We successfully designed a new boundary condition to improve the velocity profile and the pressure drop in complex geometries. This is based on the bounce-back rules with a weight-distance extrapolation of the density on concave corners and the collision operator. In single-phase flows, the new technique achieves excellent results for a low

grid resolution and low Reynolds number. The collision on a surface was shown to play an important role in the redistribution of the mass and momentum. In the collision process, the density value has to be the most realistic to conserve the momentum which the "new technique" excels at low Reynolds.
We have studied the Laplace's law with the Reis and CSF models and the classical FD 2^{nd} and 4^{th} order gradients for the colour gradient. The 2^{nd} brings quite a lot of error in term of accuracy of the Laplace's law, generates much more spurious current and deform the interface. The two models give globally the same accuracy for the Laplace's law.

We have applied our new boundary condition for two-phase flows and we have added a smooth treatment of the contact angle to improve the representation of the interface on complex geometries compared to a standard approach. The non-physical behaviours, commonly seen in literature, were almost completely removed. The contact line behaviour was correctly captured on inclined channels and a serpentine. A good agreement was found between the serpentine and a straight channel for a Reynold number of 1 and a capillary number between 1 to 10^{-3}.
The smooth treatment is applied to a Berea sandstone sample. The capillary number can characterise the two-phase flows. However, it is affected by the viscosity ratio and the contact angle. For a low viscosity ratio ($\lambda = 2$), the mobility ratio is relatively not affected by the contact angle of 45° or 90°. For a higher viscosity ratio ($\lambda = 5$), the mobility ratio becomes more dependant of the contact angle but also of the grid resolution. Our results have a capillary number between 0.003 to 1 and in reservoir simulations, the capillary number varies from 10^{-6} to 10. Therefore, our simulations are realistic and can be used to improve the simulations at reservoir scale.
The relative permeability of the displaced fluid drops with decreasing contact angle due to the saturation of the displaced fluid drops. However, it stays almost constant for contact angle more than 90°. The saturation of the invading fluid and the mobility ratio increase when the contact angle decreases. Therefore, the oil recovery will become more difficult when the saturation of the oil becomes low. We observed when the viscosity ratio increases, the capillary decreases. For high viscosity ratio, the interfacial

forces will only play a role in the transition when the flow starts to develop.

Perspective

The calculation required a lot of CPU time. The 3D calculation would be too expensive. However, using a Hele-Shaw approximation could tackle this problem. In single-phase with a force driven flow has shown very good results [157] for LBM and a two-phase flow approach was developed [13] for VOF. This needs to be extended and validated to pressure driven flows.

In porous media for oil & gas extraction, the viscosity of the oil can be very high. Thus, hot water or steam is used to reduce the viscosity of the oil. An extension of this work for non-isothermal and 3D should be highly beneficial for oil & gas companies.

In order to improve the accuracy, grid resolution and stability of the simulations, it will be interesting in the evaluation of the CM operator effect.

Another approach to reduce the computational cost would be to replace the FD scheme (Cartesian grid) by a FVM or a SEM/SEDG scheme (Deformed mesh) [158] but the parallel efficiency of the method would be drastically reduced.

Appendix A

Mesoscopic Methods

Several methods have been developed to simulate the flow from the free molecular to the continuum regimes. The most used is based on the Boltzmann equation.

Direct Simulation Monte-Carlo method

The method (particle-based) derives from the stochastic techniques used in the kinetic theory and is originate from Bird [22]. The domain is randomly filled with particles and each particle represents a huge number of molecules of gas.

The most important steps, at each time step, are streaming, colliding and sampling. During the streaming process, each particle is moved to the new position according to their initial position, velocity and boundary conditions. The collision step uses binary collisions. With the Monte-Carlo method, several collisions can be done at each time step between two particles. The selection of the two particles is done by a random draw from all particles in the simulation. The collision step is done when the criterion of the number of collisions is satisfied. The sampling is used to get the macroscopic properties.

However, the random selection process destroys the covariance in case of no correlation between the macroscopic velocity seen by the two particles. A correction was proposed by Fede [159].
In case of low covariance flow, a new technique was proposed by Baker [160]. The idea

is to represent only the deviation to the equilibrium and so not all the distribution. In order to conserve the mass, the particles have a signed. The method was extended to multi-scale to be applied to high-aspect-ratio geometries [161] to take into account different Knudsen number involving in the flow as in porous media.

LBM / DVM

LBM or Discrete Velocity Method (DVM) are deterministic methods and derived from the Boltzmann equation. To be deterministic, those methods need a lattice and a pre-deterministic velocity distribution (scheme). In LBM, the particles hop from node to node, called in-lattice and so it is possible to integrate in time analytically using the propriety of the hyperbolic equations. DVM needs to integrate in time the collision term due to the particles are streamed by a transport equation and could not fully arrive at another node, called off-lattice. Commonly, DVM is used from moderate to highly rarefied conditions rather than LBM is used from continuum regime to moderate rarefied conditions. A hybrid method exists to couple DSMC with LBM to take the advantage of DSMC in rarefy condition and LBM in continuum regime [162].

Appendix B

An example of simulations around a complex geometry

During this study, I used my code to simulate flows in other cases. Indeed, my laboratory colleagues found very useful the importation of images to simulate flows for complex geometries in a relatively short time.

For instance, the 29th Scottish Fluid Dynamics meeting was organised by my laboratory (JWFL) at the University of Strathclyde. We wanted nice images for the background of the computers used for the presentation. I realised a simulation of the flow around a famous monument of Glasgow: The Duke of Wellington and shown in Figure B.1.

Figure B.1: Duke of Wellington.

In order to simulate this kind of flow, several steps need to be done. In this thesis, Matlab was used to be easier to check the treatment from raw image to treated image. First, the raw image (Figure B.2) needs to be cleaned with an image processing software to have high contrast between the fluid part and the solid part. At this stage, the image is read then the picture is scaled to change the grid resolution. To avoid to get sharp and not physical edge, it is preferable to smooth the edges then transform to a binary image. Finally, the image is cropped to keep the domain needed then write to a file (Figure B.3). The small code is given bellow (Listing B.1). To import to LBM, each pixel corresponds to a fluid or solid node (binary file), so it is straightforward.

Figure B.2: Raw image of the duke of Wellington.

Figure B.3: Treated image of the duke of Wellington.

Listing B.1: Matlab image treatment code

```
%%Read image
OIm = imread('input_image.jpg');
%%resize
RIm=imresize(OIm, scale);
%%smooth edges
h = fspecial('disk',1);
GRIm=imfilter(RIm,h,'same');
%%Convert to binary image
BGRIm = im2bw(GRIm, level);
%%Crop Image
if x1 > size(BGRIm,2)
    x1=size(BGRIm,2);
end
if y1> size(BGRIm,1)
    y1=size(BGRIm,1);
end
```

```
L=x1-x0;
H=y1-y0;
CIm=imcrop(BGRIm,[x0 y0 L H]);
%%Write Crop image
imwrite(CIm,'output_image.jpg');
```

Bibliography

[1] Daniel H. Rothman and Jeffrey M. Keller. Immiscible cellular-automaton fluids. *Journal of Statistical Physics*, 52(3-4):1119–1127, 1988.

[2] S V Lishchuk, C M Care, and I Halliday. Lattice Boltzmann algorithm for surface tension with greatly reduced microcurrents. *Phys. Rev. E*, 67(3):36701, mar 2003.

[3] J U Brackbill, D B Kothe, and C Zemach. A continuum method for modeling surface tension* 1. *Journal of computational physics*, 100(2):335–354, 1992.

[4] Andrew K. Gunstensen, Daniel H. Rothman, Stéphane St??phane Zaleski, and Gianluigi Zanetti. Lattice Boltzmann model of immiscible fluids. *Physical Review A*, 43(8):4320–4327, 1991.

[5] M. Latva-Kokko and Daniel H. Rothman. Diffusion properties of gradient-based lattice Boltzmann models of immiscible fluids. *Physical Review E - Statistical, Nonlinear, and Soft Matter Physics*, 71(5):1–8, 2005.

[6] Edo S. Boek and Maddalena Venturoli. Lattice-Boltzmann studies of fluid flow in porous media with realistic rock geometries. *Computers and Mathematics with Applications*, 59(7):2305–2314, 2010.

[7] International - U.S. Energy Information Administration (EIA).

[8] Pierre Wuithier and Andreé Giraud. *Le Peétrole : raffinage et génie chimique. tome 1.* Editions Technip, 2nd comple edition, 1972. ISBN 271080199X.

[9] Charles-Michel Marle. *Cours de production: Les écoulements polyphasiques en milieu poreux. Tome IV*, volume 4. Editions TECHNIP, 1984.

[10] J.M. Mandhane, G.A. Gregory, and K. Aziz. A flow pattern map for gas—liquid flow in horizontal pipes, 1974. ISSN 03019322.

[11] Siti Aminah Setu, Ioannis Zacharoudiou, Gareth J. Davies, Denis Bartolo, Sébastien Moulinet, Ard a. Louis, Julia M. Yeomans, and Dirk G. a. L. Aarts. Viscous fingering at ultralow interfacial tension. *Soft Matter*, 9(44):10599, 2013.

[12] Ruben Scardovelli and Stéphane Zaleski. Direct Numerical Simulation of Free-Surface and Interfacial Flow. *Annual Review of Fluid Mechanics*, 31(1):567–603, 1999.

[13] B. Lagrée. *Modelling of two-phase flow in porous media with volume-of-fluid method.* PhD thesis, Universite Pierre et Marie Curie, 2015.

[14] Sara Thomas. Enhanced Oil Recovery – An Overview. *Oil & Gas Science and Technology – Rev. IFP*, 63(1):9–19, 2008.

[15] Laura N R Roberts, Michael D Lewan, and Thomas M Finn. Burial History, Thermal Maturity, and Oil and Gas Generation History of Petroleum Systems and Geologic Assessment of Oil and Gas in the Southwestern Wyoming Province, Wyoming, Colorado, and Utah. *U.S. Geological Survey Digital Data Series*, 3, 2005.

[16] E. Warren and B. A. Bekins. Elevated Ground Temperatures at Crude Oil Spill Sites due to Microbial Activity. *AGU Fall Meeting Abstracts*, December 2009.

[17] Quintard M. and Whitaker S. Ecoulement monophasique en milieu poreux: effet des hétérogénéités locales. *Journal de mécanique théorique et appliquée*, 6(5): 691–726, 1987.

[18] François McKee. *Etude et mise à l'échelle des écoulements diphasiques en milieux poreux hétérogènes par une approche d'optimisation.* PhD thesis, Université de Nantes, 2013.

[19] Amir Fayazi, Hadi Bagherzadeh, and Abbas Shahrabadi. Estimation of pseudo relative permeability curves for a heterogeneous reservoir with a new automatic

history matching algorithm. *Journal of Petroleum Science and Engineering*, 140: 154–163, apr 2016.

[20] Open Porous Media.

[21] Zhao Yu, Orin Hemminger, and Liang Shih Fan. Experiment and lattice Boltzmann simulation of two-phase gas-liquid flows in microchannels. *Chemical Engineering Science*, 62(24):7172–7183, 2007.

[22] G. A. Bird. *Molecular gas dynamics and the direct simulation of gas flows*. Clarendon Press, Oxford, 1994. ISBN 0198561954. 458 pp.

[23] Ting Horng Chung, Lloyd L. Lee, and Kenneth E. Starting. Applications of Kinetic Gas Theories and Multiparameter Correlation for Prediction of Dilute Gas Viscosity and Thermal Conductivity. *Industrial and Engineering Chemistry Fundamentals*, 23(1):8–13, 1984.

[24] W D Kingery and M Humenik. Surface Tension at Elevated Temperatures. I. Furnace and Method for Use of the Sessile Drop Method; Surface Tension of Silicon, Iron and Nickel. *The Journal of Physical Chemistry*, 57(3):359–363, mar 1953.

[25] S. W. Mayer. Dependence of Surface Tension on Temperature. *The Journal of Chemical Physics*, 38(8):1803–1808, apr 1963.

[26] PHYWE. Surface tension with the ring method (Du Nouy method). Technical report, PHYWE series of publications, 2017.

[27] Bruno Ferréol and Daniel H. Rothman. Lattice-Boltzmann simulations of flow through Fontainebleau sandstone. *Transport in Porous Media*, 20(1-2):3–20, 1995.

[28] Alphonsus Fagan. Porous and Permeable Rocks. In *An introduction to the petroleum industry*. Government of Newfoundland and Labrador, 1991.

[29] S. F. Benjamin and C. A. Roberts. Three-dimensional modelling of NOx and particulate traps using CFD: A porous medium approach. *Applied Mathematical Modelling*, 31(11):2446–2460, 2007.

[30] L. Chmielarz, P. Kuśtrowski, R. Dziembaj, P. Cool, and E. F. Vansant. Selective catalytic reduction of NO with ammonia over porous clay heterostructures modified with copper and iron species. *Catalysis Today*, 119(1-4):181–186, 2007.

[31] Jian Min, Joshua B. Drake, Theodore J. Heindel, and Rodney O. Fox. Experimental validation of CFD simulations of a lab-scale fluidized-bed reactor with and without side-gas injection. *AIChE Journal*, 56(6):1434–1446, 2010.

[32] Christian David. Geometry of flow paths for fluid transport in rocks. *Journal of Geophysical Research: Solid Earth*, 98(B7):12267–12278, jul 1993.

[33] Yehuda Bachmat and Jacob Bear. Macroscopic modelling of transport phenomena in porous media. 1: The continuum approach. *Transport in Porous Media*, 1(3): 213–240, sep 1986.

[34] J. B. Walsh and W. F. Brace. The effect of pressure on porosity and the transport properties of rock. *Journal of Geophysical Research*, 89(B11):9425, oct 1984.

[35] C. David, M. Darot, and D. Jeannette. Pore structures and transport properties of sandstone. *Transport in Porous Media*, 11(2):161–177, may 1993.

[36] Henry Darcy. *Les fontaines publiques de la ville de Dijon.* Libraire des Corps imperiaux des ponts et chaussées et des mines, Dijon, darmont edition, 1856. 647 pp.

[37] E Fermi, J Pasta, and S Ulam. Studies of nonlinear problems, 1955.

[38] Owen J. H. Williams, Tue Nguyen, Anne-Marie Schreyer, and Alexander J. Smits. Particle response analysis for particle image velocimetry in supersonic flows. *Physics of Fluids*, 27(7):076101, 2015.

[39] E. Cunningham. On the Velocity of Steady Fall of Spherical Particles through Fluid Medium. *Proceedings of the Royal Society A: Mathematical, Physical and Engineering Sciences*, 83(563):357–365, mar 1910.

[40] Leonhard Euler. Principes generaux du mouvement des fluides. *Histoire de l'Académie Royale des Sciences et des Belles-Lettres de Berlin*, pages pp. 274–315, 1755.

[41] Claude Louis Marie Henri Navier. Mémoire sur les Lois du Mouvement des Fluides. *Mem.acad.r.sci*, 6:389–416, 1823.

[42] George Gabriel Stokes. *On the theories of the internal friction of fluids in motion and of the equilibrium and motion of elastic solids.* PhD thesis, Cambridge University, 1845.

[43] L. B. Lucy and L. B. A numerical approach to the testing of the fission hypothesis. *The Astronomical Journal*, 82:1013, dec 1977.

[44] R. A. Gingold and J. J. Monaghan. Smoothed particle hydrodynamics-theory and application to non-spherical stars. *Monthly Notices of the Royal Astronomical Society*, 181:375–389, 1977.

[45] M. B. Liu and G. R. Liu. Smoothed Particle Hydrodynamics (SPH): an Overview and Recent Developments. *Archives of Computational Methods in Engineering*, 17(1):25–76, mar 2010.

[46] Jean-Marc Cherfils. *Développements et applications de la méthode SPH aux écoulements visqueux à surface libre.* PhD thesis, Université du Havre, 2011.

[47] Xuezhou Lu. *Simulations numériques de l'action de la houle sur des ouvrages marins dans des conditions hydrodynamiques sévères.* PhD thesis, Université du Havre, 2016.

[48] G E Karniadakis, M Israeli, and S a Orszag. High-order splitting methods for the incompressible Navier-Stokes equations. *Journal of Computational Physics*, 97(2):414–443, 1991.

[49] P F Fischer. An overlapping Schwarz method for spectral element solution of the incompressible Navier-Stokes equations. *Journal of Computational Physics*, 133 (1):84–101, 1997.

[50] Y. Maday and A. T. Patera. Spectral element methods for the incompressible Navier-Stokes equations. In *State-of-the-art surveys on computational mechanics (A90-47176 21-64). New York, American Society of Mechanical Engineers, 1989, p. 71-143. Research supported by DARPA.*, pages 71–143, 1989.

[51] M. Chrust, A. Fabregat, and C. Mavriplis. An adaptive Discontinuous Galerkin solver for the incompressible Navier-Stokes equations. In *the 21st Annual Conference of the CFD Society of Canada*, Sherbrooke, 2013. CFD Society of Canada.

[52] Adlène Benkenida and Jacques Magnaudet. Une méthode de simulation d'écoulements diphasiques sans reconstruction d'interfaces. *Comptes Rendus de l'Académie des Sciences - Series IIB - Mechanics-Physics-Astronomy*, 328(1): 25–32, jan 2000.

[53] Stanley Osher and James A Sethian. Fronts propagating with curvature-dependent speed: Algorithms based on Hamilton-Jacobi formulations. *Journal of Computational Physics*, 79(1):12–49, nov 1988.

[54] Francis H Harlow and J Eddie Welch. Numerical Calculation of Time-Dependent Viscous Incompressible Flow of Fluid with Free Surface. *Physics*, 8(12):2182–2189, 1965.

[55] Salih Ozen Unverdi and Grétar Tryggvason. A front-tracking method for viscous, incompressible, multi-fluid flows. *Journal of Computational Physics*, 100(1):25–37, 1992.

[56] J. Hardy, Yves Pomeau, and O. de Pazzis. Time evolution of a twodimensional model system. I. Invariant states and time correlation functions. *Journal of Mathematical Physics*, 14(12):1746–1759, 1973.

[57] U. Frisch, B. Hasslacher, and Y. Pomeau. Lattice-gas automata for the Navier-Stokes equation. *Physical Review Letters*, 56(14):1505–1508, 1986.

[58] D D'Humières, P Lallemand, and U Frisch. Lattice Gas Models for 3D Hydrodynamics. *Europhysics Letters (EPL)*, 2(4):291–297, 1986.

[59] Stephen Wolfram. Cellular automaton fluids 1: Basic theory. *Journal of Statistical Physics*, 45(3-4):471–526, 1986.

[60] Uriel Frisch, Dominique D'Humières, Brosl Hasslacher, Pierre Lallemand, Yves Pomeau, and Jean-Pierre Rivet. Lattice Gas Hydrodynamics in Two and Three Dimensions. *Complex Systems*, 1(4):649–707, 1987.

[61] Yue Hong Qian. *Gaz sur reseaux et theorie cinetique sur reseaux appliquee a l'equation de navier-stokes*. PhD thesis, Université Pierre et Marie Curie, 1990.

[62] Shiyi Chen, Hudong Chen, Daniel Martinez, and William Matthaeus. Lattice Boltzmann Model for Simulation of Magnetohydrodynamics. *Physical Review Letters*, 67(27):5, 1991.

[63] Yue Hong Qian, D. D'Humières, and P. Lallemand. Lattice BGK Models for Navier-Stokes Equation. *Europhysics Letters (EPL)*, 17(6):479–484, 1992.

[64] Hudong Chen, Shiyi Chen, and William H. Matthaeus. Recovery of the Navier-Stokes equations using a lattice-gas Boltzmann method. *Physical Review A*, 45 (8):5339–5342, 1992.

[65] J. M. V. A Koelman. A Simple Lattice Boltzmann Scheme for Navier-Stokes Fluid Flow. *Europhysics Letters (EPL)*, 15(6):603–607, 1991.

[66] P. L. Bhatnagar, E. P. Gross, and M. Krook. A model for collision processes in gases. I. Small amplitude processes in charged and neutral one-component systems. *Physical Review*, 94(3):511–525, 1954.

[67] D. D'Humieres, I. Ginzburg, M. Krafczyk, P. Lallemand, and L.-S. Luo. Multiple-relaxation-time lattice Boltzmann models in three dimensions. *Philosophical Transactions of the Royal Society A: Mathematical, Physical and Engineering Sciences*, 360(1792):437–451, 2002.

[68] Pierre Lallemand and Li-Shi Luo. Theory of the lattice Boltzmann method: Dispersion, dissipation, isotropy, Galilean invariance, and stability. *Physical Review E*, 61(6):6546–6562, jun 2000.

[69] Simon Marié. Etude de la méthode Boltzmann sur Réseau pour les simulations en aéroacoustique. *Thèse UPMC*, page 170, 2008.

[70] B. Dorschner, F. Bösch, S. S. Chikatamarla, K. Boulouchos, and I. V. Karlin. Entropic multi-relaxation time lattice Boltzmann model for complex flows. *Journal of Fluid Mechanics*, 801:623–651, 2016.

[71] Fabian Bosch, Shyam S. Chikatamarla, and Ilya V. Karlin. Entropic multirelaxation lattice Boltzmann models for turbulent flows. *Physical Review E - Statistical, Nonlinear, and Soft Matter Physics*, 92(4), 2015.

[72] M. Geier, A. Greiner, and J. G. Korvink. A factorized central moment lattice Boltzmann method. *European Physical Journal: Special Topics*, 171(1):55–61, 2009.

[73] Martin Geier, Andreas Greiner, and Jan G. Korvink. Properties of the Cascaded Lattice Boltzmann automaton. *International Journal of Modern Physics C*, 18 (04):455–462, 2007.

[74] Kannan N. Premnath and Sanjoy Banerjee. Incorporating forcing terms in cascaded lattice Boltzmann approach by method of central moments. *Physical Review E - Statistical, Nonlinear, and Soft Matter Physics*, 80(3), 2009.

[75] Xiaoyi He and Li-Shi Luo. Lattice Boltzmann Model for the Incompressible Navier–Stokes Equation. *Journal of Statistical Physics*, 88(3/4):927–944, aug 1997.

[76] Claude Bardos and Seiji Ukai. The classical incompressible Navier-Stokes limit of the Boltzmann equation. *Mathematical Models and Methods in Applied Sciences*, 01(02):235–257, jun 1991.

[77] D Hilbert. Begründung der kinetischen Gastheorie. *Mathematische Annalen*, 72: 562–577, 1912.

[78] D Enskog. Kinetische Theorie der Vorg{ä}nge in m{ä}ssig verd{ü}nnten Gasen. *Archiv fur Mathematik, Astronomie und Physik*, 16:655–700, 1922.

[79] C. Truesdell and R. G. Muncaster. Fundamentals of Maxwell ' s Kinetic Theory of a Simple Monatomic Gas . *Journal of Fluid Mechanics*, 104(-1):527–533, mar 1981.

[80] Harold Grad. Principles of the Kinetic Theory of Gases. In *Thermodynamik der Gase / Thermodynamics of Gases*, pages 205–294. Springer Berlin Heidelberg, 1958. ISBN 978-3-642-45892-7.

[81] Carlo Cercignani. *The Boltzmann Equation and Its Applications*, volume 67 of *Applied Mathematical Sciences*. Springer New York, New York, NY, 1988. ISBN 978-1-4612-6995-3.

[82] Cédric Villani. Limites hydrodynamiques de l'équation de Boltzmann. *Séminaire Bourbaki*, 43:365–405, 2001.

[83] Qisu Zou and Xiaoyi He. On pressure and velocity boundary conditions for the lattice Boltzmann BGK model. *Physics of Fluids*, 9(6):1591, 1997.

[84] Chih-Fung Ho, Cheng Chang, Kuen-Hau Lin, and Chao-An Lin. Consistent Boundary Conditions for 2D and 3D Lattice Boltzmann Simulations. *Cmes-Computer Modeling In Engineering & Sciences*, 44(2):137–155, 2009.

[85] Anthony J.C. A.J.C. Ladd. Numerical simulations of particulate suspensions via a discretized Boltzmann equation. Part 1. Theoretical foundation. *Journal of Fluid Mechanics*, 271(1):285–309, 1994.

[86] Jonas Latt, Bastien Chopard, Orestis Malaspinas, Michel Deville, and Andreas Michler. Velocity boundaries in the lattice Boltzmann method. *Physical review. E, Statistical, nonlinear, and soft matter physics*, 77(5 Pt 2):056703, 2008.

[87] P. Lavallée, J.P. Boon, and a. Noullez. Boundaries in lattice gas flows. *Physica D: Nonlinear Phenomena*, 47(1-2):233–240, 1991.

[88] Santosh Ansumali and Iliya V. Karlin. Kinetic boundary conditions in the lattice Boltzmann method. *Physical Review E - Statistical, Nonlinear, and Soft Matter Physics*, 66(2):1–6, 2002.

[89] Jianping Meng and Yonghao Zhang. Accuracy analysis of high-order lattice Boltzmann models for rarefied gas flows. *Journal of Computational Physics*, 230(3): 835–849, 2011.

[90] Timm Krüger, Halim Kusumaatmaja, Alexandr Kuzmin, Orest Shardt, Goncalo Silva, and Erlend Magnus Viggen. *The lattice boltzmann method Principles and Practice*. Graduate Texts in Physics. Springer International Publishing, 2017. ISBN 978-3-319-44647-9.

[91] T. J. Spencer, I. Halliday, and C. M. Care. Lattice Boltzmann equation method for multiple immiscible continuum fluids. *Physical Review E*, 82(6):066701, dec 2010.

[92] T Reis and T N Phillips. Lattice Boltzmann model for simulating immiscible two-phase flows. *Journal of Physics A: Mathematical and Theoretical*, 40(14): 4033–4053, 2007.

[93] Daryl Grunau, Shiyi Chen, and Kenneth Egger. A Lattice Boltzmann Model for Multi-phase Fluid Flows. *Physics of Fluids A*, 2557(1993):15, 1993.

[94] U. D'Ortona, D. Salin, Marek Cieplak, Renata B. Rybka, and Jayanth R. Banavar. Two-color nonlinear Boltzmann cellular automata: Surface tension and wetting. *Physical Review E*, 51(4):3718–3728, 1995.

[95] Jonas Tölke, Manfred Krafczyk, Manuel Schulz, and Ernst Rank. Lattice Boltzmann simulations of binary fluid flow through porous media. *Philosophical transactions. Series A, Mathematical, physical, and engineering sciences*, 360(1792): 535–545, 2002.

[96] Zhaoli Guo, Chuguang Zheng, and Baochang Shi. Discrete lattice effects on the forcing term in the lattice Boltzmann method. *Physical Review E - Statistical, Nonlinear, and Soft Matter Physics*, 65(4):1–6, 2002.

[97] Xiaowen Shan and Hudong Chen. Lattice Boltzmann model for simulating flows with multiple phases and components. *PHYSICAL REVIEW E*, 47(3), 1993.

[98] Haihu Liu, Qinjun Kang, Christopher R. Leonardi, Sebastian Schmieschek, Ariel Narváez, Bruce D. Jones, John R. Williams, Albert J. Valocchi, and Jens Harting. Multiphase lattice Boltzmann simulations for porous media applications. *Computational Geosciences*, 20(4):777–805, aug 2016.

[99] Chuandong Lin, Kai Hong Luo, Linlin Fei, and Sauro Succi. A multi-component discrete Boltzmann model for nonequilibrium reactive flows. *Scientific Reports*, 7(1):14580, dec 2017.

[100] Li Chen, Qinjun Kang, Bruce A. Robinson, Ya-Ling He, and Wen-Quan Tao. Pore-scale modeling of multiphase reactive transport with phase transitions and dissolution-precipitation processes in closed systems. *Physical Review E*, 87(4): 043306, apr 2013.

[101] Q. Li, Q.J. Kang, M.M. Francois, Y.L. He, and K.H. Luo. Lattice Boltzmann modeling of boiling heat transfer: The boiling curve and the effects of wettability. *International Journal of Heat and Mass Transfer*, 85:787–796, jun 2015.

[102] D. M. Anderson, G. B. McFadden, and A. A. Wheeler. Diffuse-Interface Methods in Fluid Mechanics. *Annual Review of Fluid Mechanics*, 30(1):139–165, 1998.

[103] V.L. Ginzburg;L.D. Landau. On the theory of superconductivity (in Russian). *Zh. Eksp. Teor. Fiz. (Soviet Physics JETP)*, 20:1064, 1950;English translation in: L. D. Landau, Collected papers (Oxford: Pergamon Press, 1965) p. 546.

[104] A. J. Briant, A. J. Wagner, and J. M. Yeomans. Lattice Boltzmann simulations of contact line motion. I. Liquid-gas systems. *Physical Review E - Statistical, Nonlinear, and Soft Matter Physics*, 69(3 1), 2004.

[105] Michael R. Swift, W. R. Osborn, and J. M. Yeomans. Lattice Boltzmann simulation of nonideal fluids. *Physical Review Letters*, 75(5):830–833, 1995.

[106] Michael Swift, E. Orlandini, W. Osborn, and J. Yeomans. Lattice Boltzmann simulations of liquid-gas and binary fluid systems, 1996. ISSN 1063-651X.

[107] A. J. Wagner and Q. Li. Investigation of Galilean invariance of multi-phase lattice Boltzmann methods. *Physica A: Statistical Mechanics and its Applications*, 362 (1):105–110, 2006.

[108] Qun Li. *Theory of the Lattice Boltzmann Method for Multi-Phase and Multicomponent Fluids*. PhD thesis, North Dakota State University of Agriculture and Applied Science, 2006.

[109] Sébastien Leclaire, Marcelo Reggio, and Jean-Yves Trépanier. Isotropic color gradient for simulating very high-density ratios with a two-phase flow lattice Boltzmann model. *Computers & Fluids*, 48(1):98–112, 2011.

[110] Rj LeVeque. Finite difference methods for differential equations. *Draft version for use in AMath*, pages 1998–2005, 1998.

[111] Lothar Collatz. *The Numerical Treatment of Differential Equations*. Springer Berlin Heidelberg, Berlin, Heidelberg, 1960. ISBN 978-3-642-88436-8.

[112] Sébastien Leclaire. Forward and backward finite differences for isotropic gradients on a square lattice derived from a rectangular lattice formulation. *International Journal of Computer Mathematics*, 92(5):1078–1085, may 2015.

[113] Keijo Kalervo Mattila, Luiz Adolfo Hegele J??nior, and Paulo Cesar Philippi. High-accuracy approximation of high-rank derivatives: Isotropic finite differences based on lattice-Boltzmann stencils. *The Scientific World Journal*, 2014:142907, 2014.

[114] Haihu Liu, Yonghao Zhang, and Albert J. Valocchi. Lattice Boltzmann simulation of immiscible fluid displacement in porous media: Homogeneous versus heterogeneous pore network. *Physics of Fluids*, 27(5):052103, may 2015.

[115] M Shapira and S Haber. Low Reynolds number motion of a droplet in shear flow including wall effects. *Int. J. Multiphase Flow*, 16(2):305–321, 1990.

[116] Haihu Liu. *Modelling and simulation of droplet dynamics in microfluidic devices*. PhD thesis, University of Strathclyde, 2010.

[117] Nikolaos Ioannou. *Lattice Boltzmann modelling of droplet dynamics in confinement*. PhD thesis, University of Strathclyde Department, 2016.

[118] Kameswararao Anupindi, Weichen Lai, and Steven Frankel. Characterization of oscillatory instability in lid driven cavity flows using lattice Boltzmann method. *Computers & fluids*, 92:7–21, 2014.

[119] U Ghia, K.N Ghia, and C.T Shin. High-Re solutions for incompressible flow using the Navier-Stokes equations and a multigrid method. *Journal of Computational Physics*, 48:387–411, 1982.

[120] F Archambeau, N Mechitoua, and M Sakiz. A finite volume method for the computation of turbulent incompressible flows - industrial applications. *Int. J. Finite Volumes*, 1:1–62, 2004.

[121] PaulF. Fischer and JamesW. Lottes. Hybrid schwarz-multigrid methods for the spectral element method: Extensions to navier-stokes. In TimothyJ. Barth, Michael Griebel, DavidE. Keyes, RistoM. Nieminen, Dirk Roose, Tamar Schlick, Ralf Kornhuber, Ronald Hoppe, Jacques Périaux, Olivier Pironneau, Olof Widlund, and Jinchao Xu, editors, *Domain Decomposition Methods in Science and Engineering*, volume 40 of *Lecture Notes in Computational Science and Engineering*, pages 35–49. Springer Berlin Heidelberg, 2005. ISBN 978-3-540-22523-2.

[122] NTNU. Performance and Scalability test of Code Saturne, 2018.

[123] Massimiliano Culpo. Current Bottlenecks in the Scalability of OpenFOAM on Massively Parallel Clusters. Technical report, PRACE.

[124] I. Ginzbourg and D. D'Humières. Local second-order boundary methods for lattice Boltzmann models. *Journal of Statistical Physics*, 84(5-6):927–971, 1996.

[125] Takaji Inamuro, Masato Yoshino, and Fumimaru Ogino. A non-slip boundary condition for lattice Boltzmann simulations. *Physics of Fluids*, 7(12):2928–2930, dec 1995.

[126] B. Chun and A. J.C. Ladd. Interpolated boundary condition for lattice Boltzmann simulations of flows in narrow gaps. *Physical Review E - Statistical, Nonlinear, and Soft Matter Physics*, 75(6), 2007.

[127] Jonas Latt. *Hydrodynamic limit of lattice Boltzmann equations*. PhD thesis, Université de Genève, 2007.

[128] M'hamed Bouzidi, Mouaouia Firdaouss, and Pierre Lallemand. Momentum transfer of a Boltzmann-lattice fluid with boundaries. *Physics of Fluids*, 13(11):3452–3459, 2001.

[129] Ansys Inc. ANSYS® Student, Release 17.1, 2016.

[130] MathWorks. MATLAB and Statistics Toolbox Release 2014b, 2014.

[131] Sauro Succi. *The Lattice Boltzmann Equation For Fluid Dynamics and Beyond*. Clarendon Press, 2001. ISBN 978-0-19-850398-9. 308 pp.

[132] Pierre Simon marquis de Laplace. *Traité de Mécanique Céleste*, volume 4. Courcier, Paris, 1805. 1–79 pp.

[133] Thomas Young. An Essay on the Cohesion of Fluids. *Philosophical Transactions of the Royal Society of London*, 95(0):65–87, 1805.

[134] Sébastien Leclaire, Nicolas Pellerin, Marcelo Reggio, and Jean-Yves Trépanier. An approach to control the spurious currents in a multiphase lattice Boltzmann method and to improve the implementation of initial condition. *International Journal for Numerical Methods in Fluids*, 77(12):732–746, apr 2015.

[135] P. C. Philippi, D. N. Siebert, L. A. Hegele, and K. K. Mattila. High-order lattice-Boltzmann. *Journal of the Brazilian Society of Mechanical Sciences and Engineering*, 38(5):1401–1419, 2016.

[136] Taehun Lee and Paul F. Fischer. Eliminating parasitic currents in the lattice Boltzmann equation method for nonideal gases. *Physical Review E - Statistical, Nonlinear, and Soft Matter Physics*, 2006.

[137] I Ansys. ANSYS FLUENT theory guide. *Knowledge Creation Diffusion Utilization*, 15317(November):724–746, 2009.

[138] James Jurin. An account of some experiments shown before the Royal Society; with an enquiry into the cause of the ascent and suspension of water in capillary tubes. *Philosophical Transactions of the Royal Society of London*, 30:739–747, 1717.

[139] Athanase Dupré and Paul Dupré. *Théorie mecanique de la Chaleur*. Gauthier-Villars, Paris, 1869.

[140] G. I. Taylor. The scientific papers of Sir Geoffrey Ingram Taylor. Volume 4. Mechanics of fluids: Miscellaneous papers, 1971.

[141] S. Afkhami, S. Zaleski, and M. Bussmann. A mesh-dependent model for applying dynamic contact angles to VOF simulations. *Journal of Computational Physics*, 228(15):5370–5389, aug 2009.

[142] Ahmed Taher, Benjamin Jones, Paolo Fiorini, and Liesbet Lagae. Analytical, numerical and experimental study on capillary flow in a microchannel traversing a backward facing step. *International Journal of Multiphase Flow*, 2018.

[143] A. J J Van der Zanden and A. K. Chesters. An approximate solution of the hydrodynamic problem associated with moving liquid-liquid contact lines. *International Journal of Multiphase Flow*, 20(4):789–798, sep 1994.

[144] A. M. Barajas and R. L. Panton. The effects of contact angle on two-phase flow in capillary tubes. *International Journal of Multiphase Flow*, 19(2):337–346, 1993.

[145] Markus Hilpert and Avishai Ben-David. Infiltration of liquid droplets into porous media: Effects of dynamic contact angle and contact angle hysteresis. *International Journal of Multiphase Flow*, 35(3):205–218, mar 2009.

[146] Kenji Katoh, Tatsuro Wakimoto, Yasufumi Yamamoto, and Takahiro Ito. Dynamic wetting behavior of a triple-phase contact line in several experimental systems. *Experimental Thermal and Fluid Science*, 60:354–360, jan 2015.

[147] Matthew Andrew, Branko Bijeljic, and Martin J. Blunt. Pore-scale contact angle measurements at reservoir conditions using X-ray microtomography. *Advances in Water Resources*, 68:24–31, 2014.

[148] Jun Zhang, Matthew K. Borg, and Jason M. Reese. Multiscale simulation of dynamic wetting. *International Journal of Heat and Mass Transfer*, 115:886–896, 2017.

[149] Sébastien Leclaire, Andrea Parmigiani, Orestis Malaspinas, Bastien Chopard, and Jonas Latt. Generalized three-dimensional lattice Boltzmann color-gradient method for immiscible two-phase pore-scale imbibition and drainage in porous media. *Physical Review E*, 95(3), 2017.

[150] H. B. Eral, D. J C M 'T Mannetje, and J. M. Oh. Contact angle hysteresis: A review of fundamentals and applications. *Colloid and Polymer Science*, 291(2): 247–260, 2013.

[151] Sébastien Leclaire, Kamilia Abahri, Rafik Belarbi, and Rachid Bennacer. Modeling of static contact angles with curved boundaries using a multiphase lattice Boltzmann method with variable density and viscosity ratios. *International Journal for Numerical Methods in Fluids*, 82:451–470, 2016.

[152] Jiayan Tai, Hiong Yap Gan, Yen Nan Liang, and Boon Keng Lok. Control of Droplet Formation in Inkjet Printing Using Ohnesorge Number Category: Materials and Processes. In *2008 10th Electronics Packaging Technology Conference*, pages 761–766. IEEE, dec 2008. ISBN 978-1-4244-2117-6.

[153] Roland Lenormand, Eric Touboul, and Cesar Zarcone. Numerical models and experiments on immiscible displacements in porous media. *Journal of Fluid Mechanics*, 189(-1):165–187, 1988.

[154] Harris Sajjad Rabbani, Dani Or, Ying Liu, Ching-Yao Lai, Nancy B. Lu, Sujit S. Datta, Howard A. Stone, and Nima Shokri. Suppressing viscous fingering in structured porous media. *Proceedings of the National Academy of Sciences*, 115 (19):4833–4838, 2018.

[155] Lars Hov Odsæter, Carl Fredrik Berg, and Alf Birger Rustad. Rate Dependency in Steady-State Upscaling. *Transport in Porous Media*, 110(3):565–589, dec 2015.

[156] Douglas Ruth and Huiping Ma. On the Derivation of the Forchheimer Equation by Means of the Averaging Theorem. *Transport in Porous Media*, 7:255–264, 1992.

[157] Artin Laleian, Albert J Valocchi, and Charles J Werth. An Incompressible, Depth-Averaged Lattice Boltzmann Method for Liquid Flow in Microfluidic Devices with Variable Aperture. *Computation*, 3:600–615, 2015.

[158] Misun Min and Taehun Lee. A spectral-element discontinuous Galerkin lattice Boltzmann method for nearly incompressible flows. *Journal of Computational Physics*, 230:245–259, 2011.

[159] Pascal Fede, Olivier Simonin, and Philippe Villedieu. Monte Carlo Simulation of Colliding Particles in Gas-Solid Turbulent Flows From a Joint Fluid-Particle PDF Equation. In *Volume 2: Symposia and General Papers, Parts A and B*, pages 431–438. ASME, 2002. ISBN 0-7918-3616-9.

[160] Lowell L. Baker and Nicolas G. Hadjiconstantinou. Variance reduction for Monte Carlo solutions of the Boltzmann equation. *Physics of Fluids*, 17(5):051703, may 2005.

[161] Alexander Patronis and Duncan A. Lockerby. Multiscale simulation of non-isothermal microchannel gas flows. *Journal of Computational Physics*, 270:532–543, 2014.

[162] G. Di Staso, H.J.H. Clercx, S. Succi, and F. Toschi. DSMC–LBM mapping scheme for rarefied and non-rarefied gas flows. *Journal of Computational Science*, 17:357–369, 2016.